Synchronization and Stochastic Behavior of Electrons in a Penning Trap

A thesis presented

by

Lisa Jill Lapidus

to

The Department of Physics
in partial fulfillment of the requirements
for the degree of
Doctor of Philosophy
in the subject of
Physics

Harvard University
Cambridge, Massachusetts

January 1998

©1998 by Lisa Jill Lapidus

All rights reserved

Abstract

Recent work has described the collective behavior of a large number of parametrically pumped electron oscillators as well as the behavior of a single electron in a Penning trap. The excitation of a single particle oscillator is well described by the classical Mathieu equation with interesting nonlinear dynamics appearing with increasing numbers of electrons. The plasma is extremely sensitive to the net heat in the system, particularly cooling from transverse electromagnetic modes of the cylindrical Penning trap cavity. Under certain conditions the plasma can be sufficiently cooled so that it acts like a rigid ball of charge. The goal of the current work is to bridge the single particle and many particle regimes by studying the collective behavior of "countable" numbers of electrons (i.e. 2,3,4), thereby building a plasma one electron at a time.

To Bert and Ernie

Larry, Moe and Curly,

John, Paul, George and Ringo.

And most of all,

to Fred,

without whom this work would not have been possible.

Contents

Acknowledgment **vii**

List of Figures **viii**

1 Nonneutral Plasmas Confined in a Penning Trap **1**

1.1 Overview 1

1.2 Electron Motions 3

1.3 Electromagnetic Cavity Modes 7

1.4 Full Equations of Motion 11

1.5 Plasma Behavior 13

1.6 Electrostatic Fluid Modes 15

2 Experimental Apparatus **32**

2.1 Cylindrical Trap 32

2.2 Cryostat 33

2.3 Superconducting Magnet 35

2.4 Detection 38

3 Parametric Excitation of One Electron **49**

3.1 Single Electron as a Parametric Oscillator 50

3.2 Measurement of the Axial Excursion of One Electron 55

4 Observations of Large Clouds of Electrons 60

4.1 Measurement of the Axial Excursion of Many Electrons 60

4.2 Axial Amplitude and Cyclotron Cavity Modes 63

5 Stochastic Behavior of One Electron 71

5.1 Phase Bistability of the Parametric Excitation 71

5.2 A Model of Phase Flip Transition Rates 72

5.3 Data Acquisition 75

5.3.1 Statistical Errors 75

5.3.2 Systematic Errors 76

5.4 Measured Flip Rates 77

5.4.1 Detuning and drive strength 77

5.4.2 Externally Applied Noise 79

5.4.3 Anharmonicity 82

5.4.4 Distribution of Phase Residence Times 82

5.4.5 Correlation of Phase Flips and Amplitude Collapse 82

5.5 Sources of Noise 85

5.5.1 Noise from the Inductive Amplifier 86

5.5.2 Noise from the Power Supply 86

5.6 Measurement of Flip Rates from Sources of Noise 87

5.7 Measurement of the Strength of the Noise Sources 88

6 Stochastic Behavior of Many Electrons 90

6.1 Measured Flip Rates for 2, 3 and 4 Electrons 90

6.2 Differences between 1, 2, and 3 electrons 94

6.2.1 Axial Damping and Flip Rates 94

6.2.2 Effective Temperature and Flip Rates 95

6.3 Distribution of Phase Residence Times 98

6.4 Cyclotron Damping and Flip Rates 99

7 Conclusion 101

A Derivation of Phase Flip Rates of a Parametric Oscillator 103

A.1 Fluctuational Phase Flip Transition Rates 103

A.2 Conditions of Validity of Phase Flip Rates 106

B Dynamics of 2 and 3 Electrons 109

B.1 Equilibrium Positions of 2 Electrons 109

B.2 Transfer of Energy between Axial and Cyclotron Motions 111

Acknowledgment

Thanks to my advisor, Gerald Gabrielse, for the guidance and helpful insight he provided in my graduate study. Thanks also to Daphna Enzer for theoretical support in the latter stages of this work. Theoretical work on stochastic phase flip rates was provided by Mark Dykman and Vadim Smelyanskiy of Michigan State University. Thanks to Ralph Conti at the University of Michigan for introducing us. Thanks also to Joseph Tan and Tom O'Neil for useful conversations that motivated this work and Ching-Hua Tseng for passing on all the practical experimental knowledge that never gets written down.

During my time at Harvard, I have had the pleasure of interacting with many other members of the research group: postdoctoral fellows Kamal Abdullah and Timothy Roach; students Loren Haarsma, Anton Khabbaz, David Phillips, David Hall, Steven Peil, Carla Levy, Peter Yesley, John Estrada and Paul Oxley.

Finally I would like to thank my parents, Gerald and Rachelle Lapidus for encouraging me all my life and for teaching me I could do anything I put my mind to, and my husband, Shawn Winnie, for putting up with me through the roughest periods of this work. Shawn cheerfully helped with innumerable helium fills and he was always willing to listen and provide a thoughtful opinion and a humorous comment when no one else was able to. His efforts improved this work immeasurably.

This work supported by the Office of Naval Research and the National Science Foundation.

List of Figures

1.1 The three fundamental motions of an electron in a Penning Trap 4
1.2 Setting of the compensation voltage, V_c, to make $C_4 = 0$ determined from fits of parametric lineshapes. See Chapter 3 for details. The tune point is consistent for 1 to 1000 electrons. 6
1.3 Comparison of measured and calculated frequencies for TE modes where m=0. 9
1.4 Observed cavity modes of the cylindrical Penning trap. 17

2.1 Cross section of cylindrical Penning trap 33
2.2 Cold finger dewar system 34
2.3 Bucket dewar system 36
2.4 Calibration of effective time constant of magnet shunt resistor 38
2.5 (a)The trap and inductive amplifier. (b)The equivalent LCR circuit which is resonant at $\omega_0^2 = 1/LC$. (c)The equivalent LCR circuit with the addition of electrons which short out the noise at $\omega_z^2 = 1/lc$. 39
2.6 (a) Johnson noise induced in a tuned circuit. (b) Johnson noise shorted by approximately 1000 resonantly tuned electrons. 40
2.7 Detection scheme for electrons in a Penning trap 41
2.8 Filters applied to trap for noise suppression 42
2.9 Coherent detection of one electron 43

2.10 FWHM of coherently detected Lorentzian lineshapes for small numbers of electrons. The widths are clearly discrete multiples of the width for one electron. 45

2.11 Amplitude of noise resonance relative to peak amplitude versus measured FWHM of a cloud of electrons 46

2.12 Successive loading of 3 electrons 47

2.13 Linearity of complete detection circuit and a typical measured cavity mode 48

3.1 Dynamic regions of the parametric oscillator without anharmonicity ($\lambda_4, \lambda_6 = 0$) 51

3.2 Parametric lineshapes (a) and amplitude at $\epsilon = 0$ (b) of one electron for various drive strengths 53

3.3 Parametric width versus drive strength for one electron 54

3.4 Parametric resonance with predicted parabolic lineshape 55

3.5 Parametric lineshapes for various C_4: (a) $C_4 = -3.86 \times 10^{-3}$; (b) $C_4 = 2.18 \times 10^{-4}$; (c) $C_4 = 2.81 \times 10^{-3}$ 56

3.6 The linear coefficient (b) from the parabolic fits for various compensation voltage settings. The circles and squares represent two different drive strengths. 58

4.1 (a) Measured signal dependence on compensation voltage versus number of electrons. The line is the scaled calibration for 1 electron. (b)The ratio, A/A_{rigid} extracted from (a) versus number of electrons. $A/A_{rigid} \approx 1$, showing that with strong cavity cooling, the center-of-mass of each of these clouds oscillates with the same amplitude as a rigid ball of charge. 62

4.2 Axial signal versus cyclotron frequency. The amplitude increases as the cyclotron frequency comes into resonance with a cavity mode. 64

4.3 TE_{115} cavity mode when the electron cloud is (a) not fully synchronized and (b) fully synchronized near resonance. (a) and (b) were made with different size electron clouds so the signal size was also different. 65

4.4 Mode maps at various FET drain currents when the FET is not submerged in liquid helium. As the heat dissipated in the FET increases, the noise environment of the electrons increases, and the level of synchronization decreases. 66

4.5 Parametric axial lineshapes for various detunings from the cyclotron cavity mode. The circles are the amplitudes that would be measured in a "mode map". 67

4.6 The shape of the TE_{115} becomes highly asymmetric for large N and depends on the direction the field is swept. (a) The field is swept down. (b) The field is swept up. 68

4.7 Flatness factor (flat top width/FWHM) versus (a) C_4, (b) number of electrons, (c) drive strength, and (d) axial damping. 69

4.8 Flatness factors for various drive strength and number of electrons (figures 4.7b and 4.7c) plotted against axial excursion, $z \propto A_{rigid}$, near a cavity mode. 70

5.1 Phase space of parametrically excited oscillator. The dots (A) mark the stable points and the cross (B) marks the unstable point at the origin. The lines trace the separatrix of the two basin's of attraction. 72

5.2 Parametric resonance of a single electron with the edges, $\epsilon_\pm$, marked. 74

5.3 Flip rate versus detuning of drive frequency from upper edge of parametric resonance for various drive strengths. (a)$\epsilon_+/2\pi = 31$ Hz (b)$\epsilon_+/2\pi = 60$ Hz (c)$\epsilon_+/2\pi = 100$ Hz. The lines are fits to $lnW = a + b(\epsilon_+ - \epsilon)^c$ where c=1 (solid), c=1/2 (dotted) and c=3/2 (dashed). The data clearly is insensitive to the power of the fit. 78

5.4 Linear coefficient of fit of $y = a\,exp(-b(\epsilon_+ - \epsilon))$ versus $1/\epsilon_+ \approx 4/h\omega_z$. A fit of $y = a\,exp(-b(\epsilon_+ - \epsilon)^{3/2})$ produces a similar line. 79

5.5 (a) Flip rates versus detuning from edge of parametric resonance for a single drive strength ($\epsilon_+/2\pi = 100$ Hz) and various noise power attenuations: -18 dB, circles; -21 dB, triangles; -30 dB, squares. The -30 dB line is not significantly different from data that had no noise present. (b) Flip rates versus the inverse noise relative to -30 dB for a detuning of 50 Hz. The horizontal line is the flip rate with no applied noise. 80

5.6 Flip rates of various detunings, drives and anharmonicities, shown together on the combined curve given by 5.3. The independent variable $kTS_{1,2}/D \propto \ln W$ is defined in Appendix A. The plotting symbols designate different detunings: 20Hz, circles; 50 Hz, triangles; 90 Hz, squares. 81

5.7 Histograms of time between flips for various parameter settings: (a) $\epsilon_+/2\pi =$ 100 Hz, $(\epsilon_+ - \epsilon)/2\pi = 20$ Hz; (b) $\epsilon_+/2\pi = 100$ Hz, $(\epsilon_+ - \epsilon)/2\pi = 50$ Hz; (c) $\epsilon_+/2\pi = 100$ Hz, $(\epsilon_+ - \epsilon)/2\pi = 90$ Hz; (d) $\epsilon_+/2\pi = 179$ Hz, $(\epsilon_+ - \epsilon)/2\pi = 20$ Hz;(e) $\epsilon_+/2\pi = 100$ Hz, $(\epsilon_+ - \epsilon)/2\pi = 100$ Hz with added noise; (f) $\epsilon_+/2\pi = 100$ Hz, $(\epsilon_+ - \epsilon)/2\pi = 50$ Hz, $C_4 = -1.72 \times 10^{-3}$ These plots show that an exponential distribution of time between flips is measured for a wide variety of parameters. 83

5.8 Sample of typical raw data of phase and amplitude over time. For every amplitude collapse, there is a corresponding phase flip except in three cases marked by grey circles. 84

5.9 Flip rate versus noise power for externally applied white noise near ω_z (black) and $2\omega_z$ (white). The line is a fit for the black points only. The x axis was determined for each plot from independent calibrations of the drive strength. 85

5.10 Inverse flip rate versus temperature of externally applied noise. The constant, lnC_1, is determined from fits in Fig. 5.3. The parameters, $\epsilon_+/2\pi =$ 300 Hz and $(\epsilon_+ - \epsilon)/2\pi = 450$ Hz, are outside the region where $lnW \propto (\epsilon_+ - \epsilon)^{3/2}/\epsilon_+$ so a numerical value of the exponential argument is used. . . 89

6.1 Flip rates versus number of electrons for $\epsilon_+/2\pi \approx 100$Hz and $(\epsilon_+ - \epsilon)/2\pi \approx$ 40 Hz (circles), $\epsilon_+/2\pi \approx 60$Hz and $(\epsilon_+ - \epsilon)/2\pi \approx 20$ Hz (triangles), $\epsilon_+/2\pi \approx$ 300 Hz and $(\epsilon_+ - \epsilon)/2\pi \approx 50$ Hz (squares) 91

6.2 Flip rates of 2 electrons versus detuning $(\epsilon_+ - \epsilon)/2\pi$ for (a) $\epsilon_+/2\pi = 29.11$ Hz, (b) $\epsilon_+/2\pi = 91.78$ Hz and (c) $\epsilon_+/2\pi = 297.35$ Hz 92

6.3 Flip rates of 3 electrons versus detuning $(\epsilon_+ - \epsilon)/2\pi$ for (a) $\epsilon_+/2\pi = 94.20$ Hz, (b) $\epsilon_+/2\pi = 304.39$ Hz and (c) $\epsilon_+/2\pi = 534.54$ Hz. These ϵ_+ represent the measurable range and should not be compared to the range in Fig. 6.2 93

6.4 Coefficients from the fit of $lnW = a + b(\epsilon_+ - \epsilon)$ for 1 (circles), 2 (triangles) and 3 (squares) electrons versus $1/\epsilon_+$ 94

6.5 Flip rates adjusted by $(1/f) = 8.05(\epsilon_+ - \epsilon)^{0.89}/\epsilon_+^{0.39}$ versus temperature of externally added white noise for 1 (circles), 2 (triangles) and 3 (squares) electrons. For 1 electron, $\epsilon_+/2\pi = 300$ Hz and $(\epsilon_+ - \epsilon)/2\pi = 450$ Hz. For 2 electrons $\epsilon_+/2\pi = 88$ Hz and $(\epsilon_+ - \epsilon)/2\pi = 100$ Hz. For 3 electrons $\epsilon_+/2\pi = 110$ Hz and $(\epsilon_+ - \epsilon)/2\pi = 50$ Hz. The fact that the slopes of these plots are not all 1 indicates that either the theory is not completely correct or the calibration of the external noise power changed between measurements. 95

6.6 (a) Linear coefficients from the fit of $lnW = a + b(\epsilon_+ - \epsilon)$ versus $1/\epsilon_+$ for 2 electrons with full axial damping (black) and half axial damping(grey). (b) same as (a) for 3 electrons with full axial damping (black) and one third axial damping (grey). 96

6.7 Linear coefficient of fit of $\ln W = a + b(\epsilon_+ - \epsilon)^{0.89}$ plotted versus $1/\epsilon_+$. The solid line is the fit of $b = c/\epsilon_+^{0.39}$, giving a $T + \bar{X} = 12.9 \pm 6.4$ K 97

6.8 Histogram of phase residence times of 2 electrons for (a) $\epsilon_+/2\pi = 92$ Hz, $(\epsilon_+ - \epsilon)/2\pi = 30$ Hz and (b) $\epsilon_+/2\pi = 56$ Hz, $(\epsilon_+ - \epsilon)/2\pi = 20$ Hz. 98

6.9 Histogram of phase residence times of 3 electrons for (a) $\epsilon_+/2\pi = 304$ Hz, $(\epsilon_+ - \epsilon)/2\pi = 20$ Hz and (b) $\epsilon_+/2\pi = 533$ Hz, $(\epsilon_+ - \epsilon)/2\pi = 50$ Hz. 99

6.10 Parametric amplitudes and flip rates across a cavity mode. As the mode detuning increases, the center of the lineshape collapses so that the measured amplitude (a) decreases to zero far from the mode. (b) The mean phase residence time ($\tau = 1/W$) also decreases with mode detuning so that either the amplitude or the $\log \tau$ are good measures of the mode cooling power. 100

A.1 Activation energy verses relative detuning. The solid line is numerical form from which Eq. A.14 is derived. The dotted line is the approximation from which Eq. A.9 is derived. It is clear the approximation is only valid for $(\epsilon_+ - \epsilon)/\epsilon_+$ near zero. 106

Chapter 1

Nonneutral Plasmas Confined in a Penning Trap

1.1 Overview

The vast majority of physical systems are characterized by complex behavior due to nonlinear interactions between various components. The synchronization of various motions is the hallmark of many such complex systems. Examples of self-synchronization of nonlinear oscillators abound in biology, chemistry and physics. More than 300 years ago, Huygens noted that clocks hanging on the same wall over time tended to synchronize the phases of their swinging pendula [1]. More recently, self-organized behavior has been observed in the beating of heart cells and arrays of Josephson junctions [2,3]. Nonlinear systems have often been neglected as subjects of scientific research because they are difficult to characterize and were assumed to lack any universality in their complex behavior. However, there have been some recent advances in understanding of complex systems. For example, in 1978 Feigenbaum showed there is a universality in chaos [4] and several researchers over the past decade have described stochastic resonance of bistable systems in the presence of noise [5, 6]. The work of this thesis takes the approach of starting with the well understood system of a single electron in a Penning trap. The complexity is increased by adding individual electrons to the trap.

The experiments performed for this thesis use electrons in a Penning trap with a very good vacuum. The electrons are cooled by coupling them to electromagnetic modes of a high quality cylindrical microwave cavity formed by the trap electrodes. A simple cylindrical geometry allows easy identification of individual standing wave modes of the cavity, which are well separated in frequency. Such cooling was first observed and used by Tan and Gabrielse to synchronize the axial motion of between 10 and 10000 electrons [7]. Without cavity cooling, the parametrically driven oscillatory axial motion produces no observed excitation of the axial center of mass because anharmonic internal motions dominate the motion of the center of mass. With strong cavity cooling, however, electron synchronization causes a very large and clearly observable excitation of the center of mass. One of two major advances reported in this thesis is the demonstration that with strong cavity cooling the electrons synchronize so completely that the oscillation amplitude of the center of mass is the same size as would be expected for a rigid ball of charge. This dramatic synchronization of trapped electrons is achieved when the Coulomb interactions shunting energy from the internal motions to the cyclotron motion which then damps to the cavity. Such synchronization is presented for collections of electrons ranging from 2 to 1000.

Order has been previously observed in collections of trapped charged particles. In 1959, Wuerker, Shelton and Langmuir observed that aluminum particles in a Paul trap formed an ordered array when cooled by gas collisions [8]. More recently similar ordered systems have been observed with small numbers of laser cooled ions in Penning and Paul traps [9–11]. Each of these systems required a transfer of energy to achieve order. However, these experiments were performed at equilibrium; the cooling produced a high correlation between the charges which resulted in crystallization. The observations in this thesis are of a system that is far from equilibrium.

The second major advance reported here builds upon the demonstration by Tseng et. al. [12] that a single electron in a Penning trap is a good approximation of an ideal parametric oscillator. The ideal parametric oscillator is a phase bistable system, but we have studied the conditions under which random phase switching occurs due to the presence of noise. Such abrupt transitions had been observed with many electrons [7], but were not initially expected for a single electron. Two and three electrons that are fully synchronized show similar phase switching behavior to a single electron. The transition rates are exponentially lower for more electrons, presumably due to a higher efficiency of cavity cooling of the internal motions. If the cavity cooling is decreased, the flip rate for more than one electron increases with the loss of synchronization. This work stimulated a theory by Maloney, et. al. of the Dykman group at Michigan State University [13] that agrees with our measurement. Double well systems such as this were first described by Kramers in 1940 in the context of chemical reactions [14]. The field has been expanded and refined over the years to explain phase switching in electric circuits and Josephson junctions [5, 15–17].

Chapter 1 discusses the individual motions of an electron in a trap, the interaction of the electron with the cavity, and fluid behavior of a large plasma of electrons. Chapter 2 covers the details of the experimental apparatus. Chapter 3 develops the parametric oscillator in the context of a single electron, and Chapter 4 discusses the onset of rigid behavior for many electrons. Chapter 5 presents the measurements of phase flips of a single electron and Chapter 6 describes how the flip rates for many electrons differ from those of a single electron. Chapter 7 presents some conclusions and suggests future directions of this work.

1.2 Electron Motions

The motions of a single electron in a Penning trap are very well understood [18–20]. There are three fundamental oscillatory motions, the axial, the cyclotron and the magnetron. Each motion would be independent except for couplings by electrostatic anharmonicity, magnetic gradients, special relativity and, with more than one particle, the Coulomb

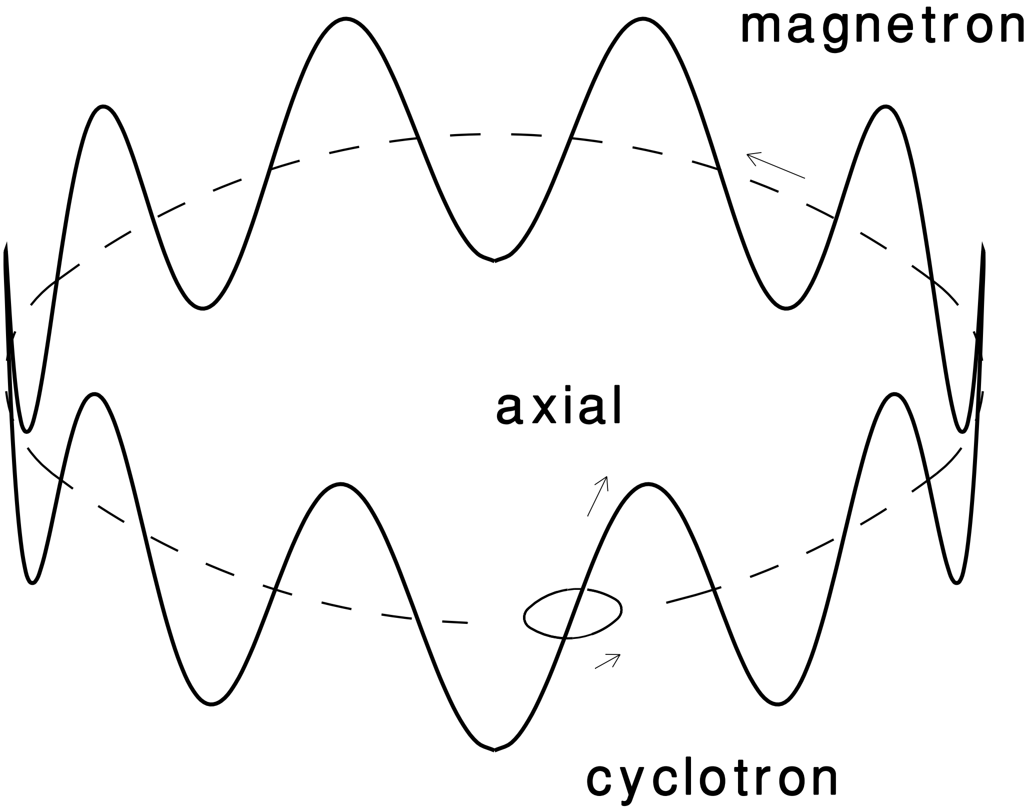

Figure 1.1: The three fundamental motions of an electron in a Penning Trap

interaction. Although it has been shown that the cyclotron motion of a single electron at 4 Kelvin is intrinsically quantum mechanical, the energy and rapid decoherence of our cyclotron oscillators make a quantum mechanical treatment unnecessary. In this section we shall discuss the classical motions of a single electron. The full equations of motion for an arbitrary number of electrons, including the Coulomb interaction, will be discussed in Section 1.4.

The electron is confined by and oscillates in an electrostatic quadrupole potential

$$V(\vec{r}) = V_o \frac{z^2 - \frac{1}{2}\rho^2}{2d^2}\left[1 + C_2\right] \tag{1.1}$$

where V_o is the voltage applied between the ring and endcaps, C_2 is a dimensionless constant dependent on the trap geometry, and d is a characteristic trap dimension defined in terms of the axial and radial trap dimensions, z_o and ρ_o

$$d = \sqrt{\frac{1}{2}\left(z_o^2 + \frac{1}{2}\rho_o^2\right)} = 0.354\,\text{cm}. \tag{1.2}$$

For the perfect quadrupole in Eq. 1.1, the axial motion along the direction of a uniform magnetic field is a harmonic oscillator with an angular frequency given by

$$\omega_z^2 = \frac{eV_o}{md^2}[1 + C_2]. \tag{1.3}$$

V_o is a potential applied to electrodes comprising the trap by an extremely stable solid state power supply and voltage divider and is typically about 10 V. For our cylindrical cavity trap, C_2 is about 0.1 [21, 22]. This gives an axial frequency of approximately 60 MHz. In reality, the potential is not a perfect quadrupole because the electrodes are not the equipotential surfaces of an ideal quadrupole. Therefore, the trap contains two compensation electrodes with voltages set to minimize the anharmonicity. The actual potential in the Penning trap can be written as a series expansion given by

$$V(\vec{r}) = V_o\left(\frac{z^2 - \frac{1}{2}\rho^2}{2d^2}\right) + \frac{1}{2}V_o \sum_{k\text{ even}}^{\infty} C_k \left(\frac{r}{d}\right)^k P_k(\cos\theta). \tag{1.4}$$

The sum is only over even n because the potential must be symmetric under axial reflections. P_k are Legendre polynomials in cylindrical coordinates. The expansion coefficients can be written as

$$C_k = C_k^{(0)} + D_k \frac{V_c}{V_o} \tag{1.5}$$

where C_k^0 and D_k are calculable near the center of a perfectly aligned trap. The expansion converges rapidly for small oscillations so only the terms C_2, C_4 and C_6 are considered. Table 1.2 gives the calculated coefficients for an ideal cylindrical trap with no gaps or slits in the electrodes [21]. The compensation potential, V_c can be set to make $C_4 = 0$ which is considered to be the point at which the trap is "tuned." This tune point can be seen

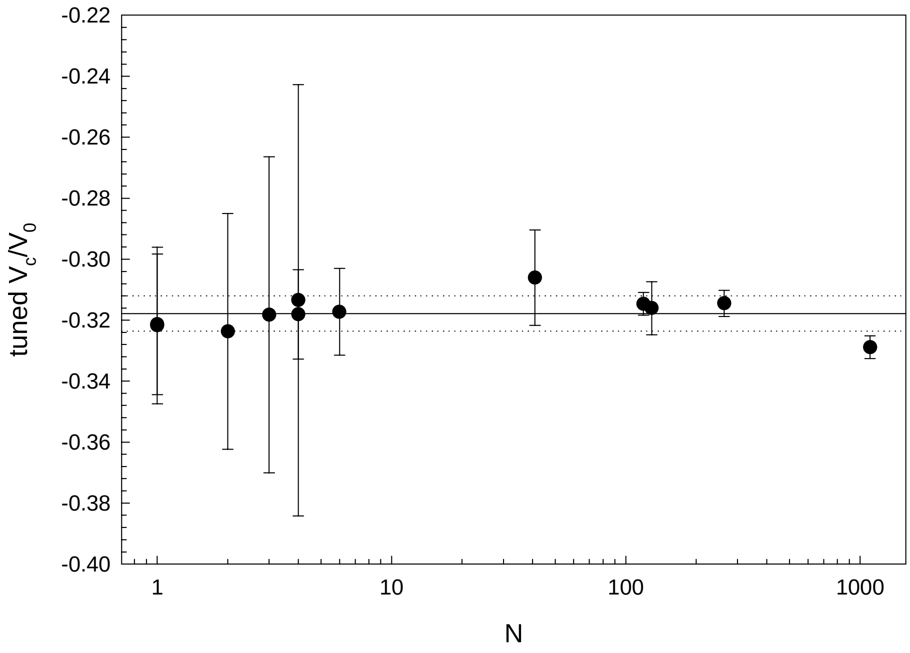

Figure 1.2: Setting of the compensation voltage, V_c, to make $C_4 = 0$ determined from fits of parametric lineshapes. See Chapter 3 for details. The tune point is consistent for 1 to 1000 electrons.

experimentally with both coherent and parametric detection as is seen in Fig. 1.2 which shows that the tune point is valid for up to 1000 electrons.

The cyclotron motion is the circular motion that occurs when a charged particle moves in the presence of a magnetic field. In this case the magnetic field lines are highly homogeneous and aligned with the z axis of the trap so the cyclotron motion is entirely orthogonal to the axial motion. The cyclotron frequency is given by

$$\omega_c = \frac{eB}{m} \tag{1.6}$$

where m is the mass of the electron and e is the charge. The superconducting magnet used in these experiments has a continuously variable field of up to 6 Tesla so the cyclotron

k	C_k^o	D_k
2	0.125	0.000428
4	-0.0164 ± 0.0009	-0.0551± 0.0004
6	-0.0905	0.0123

Table 1.1: Calculated values of anharmonicity coefficients for an ideal cylindrical trap with no slits in its electrodes. The errors for $k = 4$ come from a calculated error in the trap dimensions based on a measurement of many cavity standing wave modes (see Fig. 1.3)

frequency can be set between 0 and 160 GHz.

The last motion is a magnetron motion in the x-y plane caused by perpendicular electric and magnetic fields. The frequency is given by

$$\omega_m = \frac{\omega_z^2}{2\omega_c'} \tag{1.7}$$

where $\omega_c' = \omega_c - \omega_m$. The magnetron frequency, $\omega_m/2\pi$, ranges between 11 and 20 kHz. Unlike the axial and cyclotron motion, the magnetron motion is unstable as the orbit sits on a potential hill with larger orbits having lower energies. However, the damping time is very long with such a large magnetic field and the motion for a single electron has been shown to be "cooled" (pushed up the potential hill) by a drive applied at $\omega_z + \omega_m$ [18].

1.3 Electromagnetic Cavity Modes

The electrodes that create the trapping potential for the Penning trap necessarily form a microwave cavity which may enhance or inhibit synchrotron radiation of the electrons. This trap was designed to approximate a perfect cylindrical cavity without slits and holes and with walls of infinite conductivity. In a perfect cavity, the radiative mode structure is well understood. The standing wave field vanishes at the walls which gives TM and TE fields in cylindrical coordinates (ρ, ϕ, z) as [23]

TM Fields

$$\begin{aligned}\vec{E}_t &= \frac{p\pi\rho_0^2}{z_0\chi_{mn}^2}\sin\left(\frac{p\pi z}{z_0}\right)\vec{\nabla}_t\psi\\ \vec{B}_t &= \frac{i\epsilon\omega\rho_0^2}{c\chi_{mn}^2}\cos\left(\frac{p\pi z}{z_0}\right)\hat{z}\times\vec{\nabla}_t\psi\\ E_z &= \psi(\rho,\phi)\cos\left(\frac{p\pi z}{z_0}\right)\\ H_z &= 0\end{aligned} \tag{1.8}$$

$$\psi(\rho,\phi) = E_0 J_m\left(\frac{\chi_{mn}\rho}{\rho_0}\right)e^{\pm im\phi} \tag{1.9}$$

TE Fields

$$\begin{aligned}\vec{E}_t &= \frac{-i\omega\rho_0^2}{c\chi_{mn}'^2}\sin\left(\frac{p\pi z}{z_0}\right)\hat{z}\times\vec{\nabla}_t\psi\\ \vec{B}_t &= \frac{p\pi\rho_0^2}{z_0\chi_{mn}'^2}\cos\left(\frac{p\pi z}{z_0}\right)\vec{\nabla}_t\psi\\ E_z &= 0\\ B_z &= \psi(\rho,\phi)\sin\left(\frac{p\pi z}{z_0}\right)\end{aligned} \tag{1.10}$$

$$\psi(\rho,\phi) = E_0 J_m\left(\frac{\chi_{mn}'\rho}{\rho_0}\right)e^{\pm im\phi} \tag{1.11}$$

$$m = 1, 2, 3 ... \infty$$

$$n = 0, 1, 2 ... \infty$$

$$p = 0, 1, 2 ... \infty$$

where χ_{mn} is the nth root of the equation $J_m(x) = 0$ and χ_{mn}' is the nth root of $J_m'(x) = 0$.

The frequency of the TM fields are given by

$$\omega_{mnp} = c\sqrt{\left(\frac{\chi_{mn}}{\rho_o}\right)^2 + \left(\frac{p\pi}{2z_o}\right)^2}. \tag{1.12}$$

The frequencies of the TE fields have the same form except χ'_{mnp} is substituted for χ_{mnp}. Fig. 1.3 compares measured and calculated frequencies m=0 TE modes.

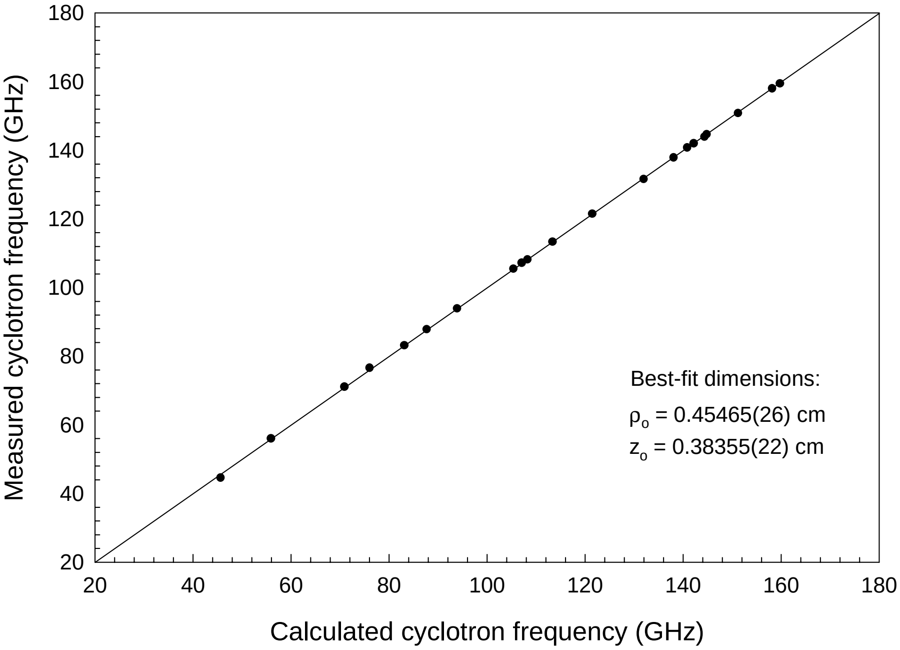

Figure 1.3: Comparison of measured and calculated frequencies for TE modes where m=0.

Of particular interest are the modes where m=1 and p is odd. These "strongly coupled" modes have a standing wave maximum (an antinode) at the center of the trap in the radial electric field which strongly couples the cavity and the cyclotron motion of electrons at the center of the trap.

An electron cyclotron oscillator in a cavity may have inhibited or enhanced emission of synchrotron radiation depending on the detuning of cyclotron frequency from a TE or TM cavity mode [24]. If the modes are well separated in frequency, the shift in the cyclotron frequency due to the interaction with the cavity mode is given by [25]

$$2\pi\Delta\nu = \frac{1}{2}\gamma Q_M \delta_M \tag{1.13}$$

$$\gamma = A_M \frac{Q_M}{1+(Q_M\delta_M)^2} \tag{1.14}$$

where $\delta_M = 2(\omega_c - \omega_M)/\omega_M$ is the detuning of the cyclotron frequency from the mode center frequency and Q_M is the quality factor of the mode. The frequency shifts are of importance in precision measurements, such as a measurement of the anomalous magnetic moment of the electron. The most precise measurement of the magnetic moment was made in a hyperbolic Penning trap several years ago [26, 27]. The damping rate of the cyclotron motion was observed to be 3 times smaller than that of free space, indicating the cavity was inhibiting synchrotron radiation [24]. This was the leading order uncertainty in that measurement. Since the cavity mode structure of a hyperbolic trap is difficult to understand, a new series of measurements is planned for the cylindrical trap in which the cavity shifts can be well understood. If ω_M and Q_M can be measured to high level of certainty, the cyclotron frequency can be set to the point where the frequency shift is zero. The resulting measurement of the magnetic moment is free of the effects of the cavity.

An important component of this new measurement of the anomalous magnetic moment is the accurate measurement of the frequency and quality factor of the cylindrical cavity. Previous work has shown [7, 25, 28] that the electrons in the trap may be used as a probe of the cavity. When the cyclotron frequency is resonant with a cavity mode, the energy in the cyclotron motion is more efficiently transferred to the cavity than when the cyclotron frequency is detuned from the mode. When more than one particle is in the trap, the Coulomb interaction transfers energy between the cyclotron and axial motions so the cavity mode cools the axial energy as well. Since theoretically the cooling rate depends on the detuning of the cyclotron frequency as given in Eq. 1.14, the observed modes can be fit to Lorentzians, yielding a center frequency and a width. If a Lorentzian shape is seen in the cavity mode structure independent of the motion of the trapped electrons and the strength of the parametric drive, it is assumed that what is measured is this cooling rate. Fig. 1.4 shows observation of such modes (the details of how electrons are used to probe the cavity will be discussed in Chapter 4). The frequencies of the observed modes agree well with those predicted by the dimensions of the trap, but the quality factors of the modes depend on more subtle details of the cavity such as machining imperfections and gaps between the electrodes. Therefore the measurement of the widths of these Lorentzians are the best measurement of the quality factors. However, Chapter 4 will show that the nonlinear dynamics of the cloud of electrons sometimes produces cavity mode lineshapes that are not Lorentzian. These effects will be explored in later chapters.

1.4 Full Equations of Motion

The full equations of motion for the kth electron in a plasma are [7]

$$\begin{aligned}\ddot{z_k} + \gamma_z \sum_{i=0}^{N} \dot{z}_i + \omega_z^2 z_k + \lambda_4 \omega_z^2 (2z_k^2 - 3\rho_k^2) z_k \\ +\lambda_6 \omega_z^2 (3z_k^4 - 15 z_k^2 \rho_k^2 + \frac{45}{8}\rho_k^4) z_k \\ = \omega_{ee}^2 \sum_{i \neq k}^{N} \frac{(z_k - z_i)}{\mid \vec{r}_{ik} \mid^3}\end{aligned} \tag{1.15}$$

$$\begin{aligned}\ddot{x_k} - \omega_c \dot{y_k} - \frac{1}{2}\omega_z^2 x_k - 3\lambda_4 \omega_z^2 (z_k^2 - \frac{\rho_k^2}{4}) x_k - \\ \frac{15}{2}\lambda_6 \omega_z^2 (z_k^4 - \frac{3}{2} z_k^2 \rho_k^2 + \frac{1}{8}\rho_k^4) x_k \\ + \sqrt{\frac{r_e}{z_o}} \omega_M \Lambda_M(\vec{r}_k) \dot{f}_x \\ = \omega_{ee}^2 \sum_{i \neq k}^{N} \frac{(x_k - x_i)}{\mid \vec{r}_{ik} \mid^3}\end{aligned} \tag{1.16}$$

$$\ddot{y_k} + \omega_c \dot{x_k} - \frac{1}{2}\omega_z^2 y_k - 3\lambda_4 \omega_z^2 (z_k^2 - \frac{\rho_k^2}{4}) y_k -$$

$$\begin{aligned}\frac{15}{2}\lambda_6\omega_z^2(z_k^4 - \frac{3}{2}z_k^2\rho_k^2 + \frac{1}{8}\rho_k^4)y_k& \\ +\sqrt{\frac{r_e}{z_o}}\omega_M\Lambda_M(\vec{r}_k)\dot{f}_y& \\ = \omega_{ee}^2\sum_{i\neq k}^{N}\frac{(y_k - y_i)}{\mid \vec{r}_{ik}\mid^3}& \end{aligned} \qquad (1.17)$$

$$\begin{pmatrix}\ddot{f}_x\\ \ddot{f}_y\end{pmatrix} + \Gamma_M\begin{pmatrix}\dot{f}_x\\ \dot{f}_y\end{pmatrix} + \omega_M^2\begin{pmatrix}f_x\\ f_y\end{pmatrix} - \sqrt{\frac{r_e}{z_0}}\omega_M\sum_{k=1}^{N}\Lambda_M(\mathbf{r_k})\begin{pmatrix}\dot{x_k}\\ \dot{y_k}\end{pmatrix} = 0 \qquad (1.18)$$

Eq. 1.18 gives the equation of motion for the dimensionless field components (f_x, f_y) for an m=1 cavity mode near the center of the trap. Table 1.2 gives the values of the frequencies and damping rates [7]. The frequency domain of this system spans many orders of magnitude. The experimental consequence is that each of the motions can be driven separately without perturbing the other motions. However, the greatly separated timescales makes the dynamics of the system very hard to calculate numerically, particularly when the interesting motion is the axial oscillation (which is what is observed). The calculation must compute many axial bounces to see the effect of the axial damping (For example, the onset of parametric excitation occurs on the order of the axial damping time). Another computational difficulty is the long range Coulomb interaction. Unlike other many body systems (such as a collection of molecules) there are no shielding effects of the surrounding electrons to shorten the range of the electric field from one particular electron. Therefore, the repulsion force has to be calculated between each and every electron pair. These equations contain all the natural motions and damping mechanisms, but none of the externally applied drives and noise that is seen in the actual experiment. As will be seen in Chapter 4, it is the relative balance of the noise and damping mechanisms that determines the observed coherence of the electron plasma.

Electron parameters		
Axial damping width	$\gamma_z/2\pi$	14 Hz
Collision constant	$\omega_{ee}/2\pi$	12 kHz
Axial frequency	$\omega_z/2\pi$	61.6 MHz
Cyclotron Frequency	$\omega_c/2\pi$	30 - 160 GHz
Mode Parameters (TE_{115})		
Mode Frequency	$\omega_M/2\pi$	98 GHz
Mode damping width	$\Gamma_M/2\pi$	300 MHz
Electron Cavity Coupling	Λ_M	0.31

Table 1.2: Typical values for electron and mode parameters.

1.5 Plasma Behavior

Since the equations in the previous section become unwieldy for more than a small number of electrons, a kinetic fluid description has been developed for a general collisionless nonneutral plasma based on the Vlasov-Maxwell equation which gives a rigid rotor distribution function rotating at ω_r [29]

$$f(\vec{r},\vec{v}) = n_o \left[\frac{m}{2\pi kT}\right] e^{-\frac{H+\omega l_z}{kT}} \tag{1.19}$$

$$H = \frac{1}{2}mv^2 + q\phi(r,z) \tag{1.20}$$

$$l_z = mv_\theta r + \frac{qBr^2}{2} \tag{1.21}$$

where H is the Hamiltonian for charges q in a Penning trap and l_z is the canonical angular momentum. The distribution function is separable into spatial and velocity parts

$$f(\vec{r},\vec{v}) = n(r,z) \left[\frac{m}{2\pi kT}\right] e^{-\frac{m(\vec{v}+mr\hat{\theta})}{2kT}} \tag{1.22}$$

where

$$n(r,z) = n_0 e^{-\frac{q\phi(r,z)+\frac{1}{2}m\omega(\omega_c-\omega)r^2}{kT}} \tag{1.23}$$

At T=0, the density, $n(r, z)$, is zero unless

$$q\phi(r, z) + \frac{1}{2}m\omega_r(\omega_c - \omega_r)r^2 = 0 \tag{1.24}$$

Therefore the density is a constant inside the plasma and zero outside the plasma. For $T > 0$, the constant density goes to zero outside the cloud on the order of the Debeye length [30]

$$\lambda_0 = \sqrt{\frac{\varepsilon_o kT}{n_0 q^2}} \tag{1.25}$$

which is approximately 10 μm for this experiment at $T = 4.2$ K.

Using Poisson's equation, the constant density can be determined from Eq. 1.24 to be

$$n_o = \frac{2\varepsilon_0 m\omega_r(\omega_c - \omega_r)}{q^2}. \tag{1.26}$$

We define the plasma frequency as

$$\omega_p^2 = \frac{q^2 n_0}{\varepsilon_0 m} = 2\omega_r(\omega_c - \omega_r) = \omega_z \frac{\alpha^2 - 1}{Q_1^0\left[\frac{\alpha}{\sqrt{\alpha^2-1}}\right]} \tag{1.27}$$

where Q_1^0 is an associated Legendre polynomial of the 1st order and $\alpha = z/r$ is the aspect ratio of the cloud. Therefore the density can be determined from the aspect ratio which in turn may be determined from other measurable frequencies described in the next section.

The potential experienced by the charges inside the plasma may be split into two parts, the trap potential and the space charge potential given by

$$\begin{aligned} \phi_T(r, z) &= \tfrac{m\omega_z^2}{4q}(2z^2 - r^2) \\ \phi_I(r, z) &= \left[\tfrac{m\omega_z^2}{4q} - \tfrac{m\omega_r(\omega_c-\omega_r)}{2q}\right] r^2 - \tfrac{m\omega_z^2}{4q} z^2 \\ &= \tfrac{m\omega_p}{6q}[a(\alpha)r^2 + b(\alpha)z^2] \end{aligned} \tag{1.28}$$

The space charge potential is of the form of a uniformly charged spheroid, an ellipse rotated about the z axis.

1.6 Electrostatic Fluid Modes

The isotropic nature of the Coulomb repulsion of the electrons allows energy to be transferred from one degree of freedom to another. Calculations by Dubin and others [31, 32] have shown that a trapped nonneutral plasma has an infinite number of electrostatic fluid modes which are calculated from a perturbation expansion of the trap potential, density and fluid velocity. Accounting for the plasma frequency (ω_p) as defined in the previous section and the vortex frequency ($\Omega_v = \omega_c - \omega_m$) , the Poisson equation for the perturbed trap potential (ψ) can be written as

$$\nabla \cdot \vec{\varepsilon} \cdot \nabla\psi = 0 \tag{1.29}$$

which is just Maxwell's equation $\nabla \cdot \vec{D} = 0$ for a medium with a linear frequency -dependent anisotropic dielectric tensor given by

$$\vec{\varepsilon} = \begin{pmatrix} \varepsilon_1 & -i\varepsilon_2 & 0 \\ i\varepsilon_2 & \varepsilon_1 & 0 \\ 0 & 0 & \varepsilon_3 \end{pmatrix} \tag{1.30}$$

$$\varepsilon_1 = 1 - \frac{\omega_p^2}{\omega^2 - \Omega_v^2} \tag{1.31}$$

$$\varepsilon_2 = \frac{\Omega_v \omega_p^2}{\omega(\omega^2 - \Omega_v^2)} \tag{1.32}$$

$$\varepsilon_3 = 1 - \frac{\omega_p^2}{\omega^2} \tag{1.33}$$

inside the plasma. $\vec{\varepsilon} = 1$ outside the plasma. The inner and outer solutions to Eq. (1.29) must be matched across the boundary according to

$$\psi^{in} = \psi^{out} |_{boundary} \tag{1.34}$$

$$\hat{n} \cdot \vec{\varepsilon} \cdot \nabla\psi^{in} = \hat{n} \cdot \nabla\psi^{out} \mid_{boundary} . \tag{1.35}$$

The solution is only separable in spheroidal coordinates (ξ_1, ξ_2, ϕ). Surfaces of ξ_1 are confocal spheroids; surfaces of ξ_2 are confocal hyperboloids. ϕ is the usual azimuthal angle. The solutions inside the plasma are of the form

$$\psi = AQ_l^m(\xi_1/d)P_l^m(\xi_2)e^{i(m\phi-\omega t)} \tag{1.36}$$

where A is a constant and Q_l^m and P_l^m are associated Legendre functions. The frequencies are given by the equation

$$\varepsilon_3 P_l^{m\prime} + m\alpha\left[\alpha^2 - \frac{\varepsilon_3}{\varepsilon_1}\right]^{1/2} P_l^m \varepsilon_2 - \left[\frac{\alpha^2 - \epsilon_3/\varepsilon_1}{\alpha^2 - 1}\right] P_l^m \frac{Q_l^{m\prime}}{Q_l^m} = 0 \tag{1.37}$$

where $P_l^m = P_l^m(\alpha/(\alpha^2 - \varepsilon_3/\varepsilon_1)^{1/2}), Q_l^m = Q_l^m(\alpha/(\alpha^2-1)^{1/2}), \alpha = z_o/\rho_o$, and the primes denote differentiation with respect to the entire argument.

The lowest order mode (1,0) is the rigid motion of the center of mass. Higher order modes contain internal motions that change the shape of the plasma such as the mode (2,0) in which the aspect ratio of the spheroid oscillates from large (long and thin) to small (broad and flat). Some of these modes have been observed in ion [32] and electron [33] plasmas. Because the frequencies of these modes depend on the steady state aspect ratio and hence the density of the cloud, detection and identification of several modes could give a good measure of the these parameters.

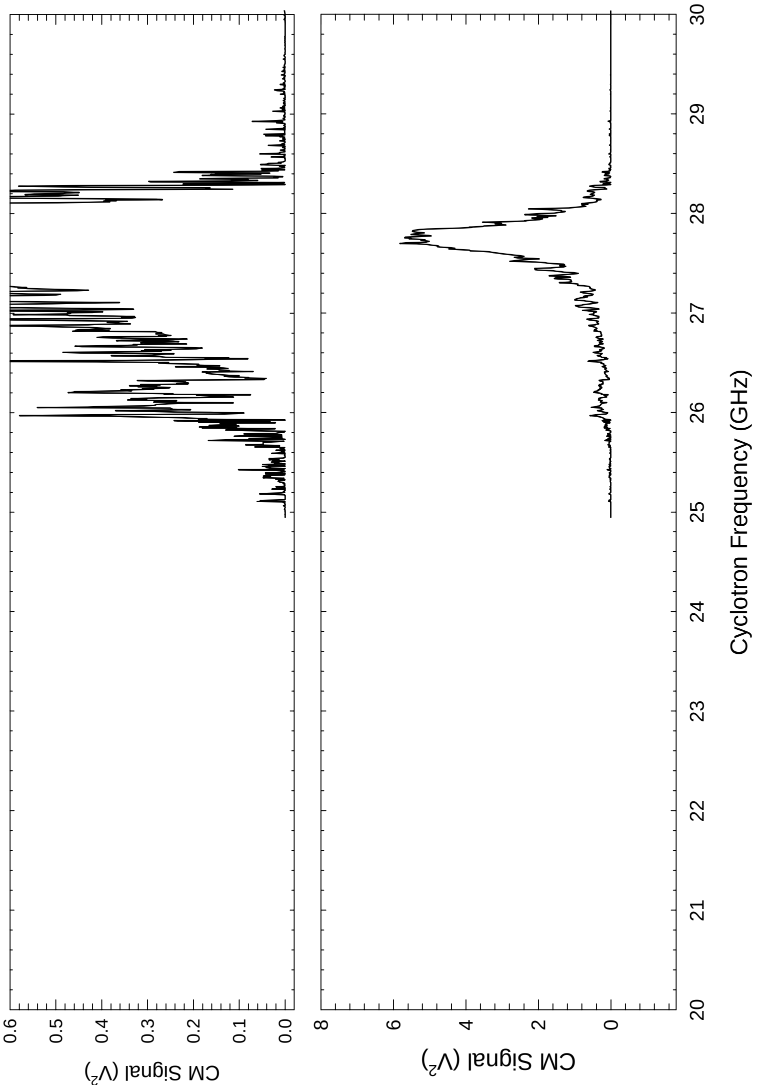

Figure 1.4: Observed cavity modes of the cylindrical Penning trap.

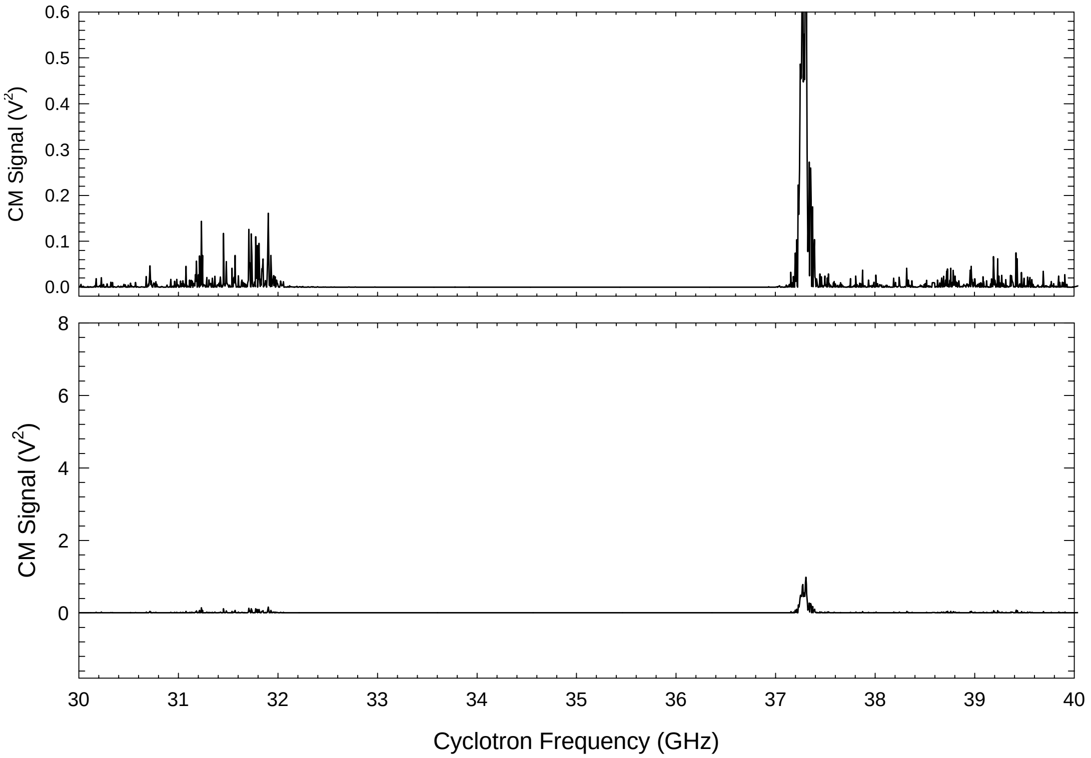
CM Signal (V^2)
0.6
0.5
0.4
0.3
0.2
0.1
0.0
CM Signal (V^2)
8
6
4
2
0
30
31
32
33
34
35
36
37
38
39
40
Cyclotron Frequency (GHz)

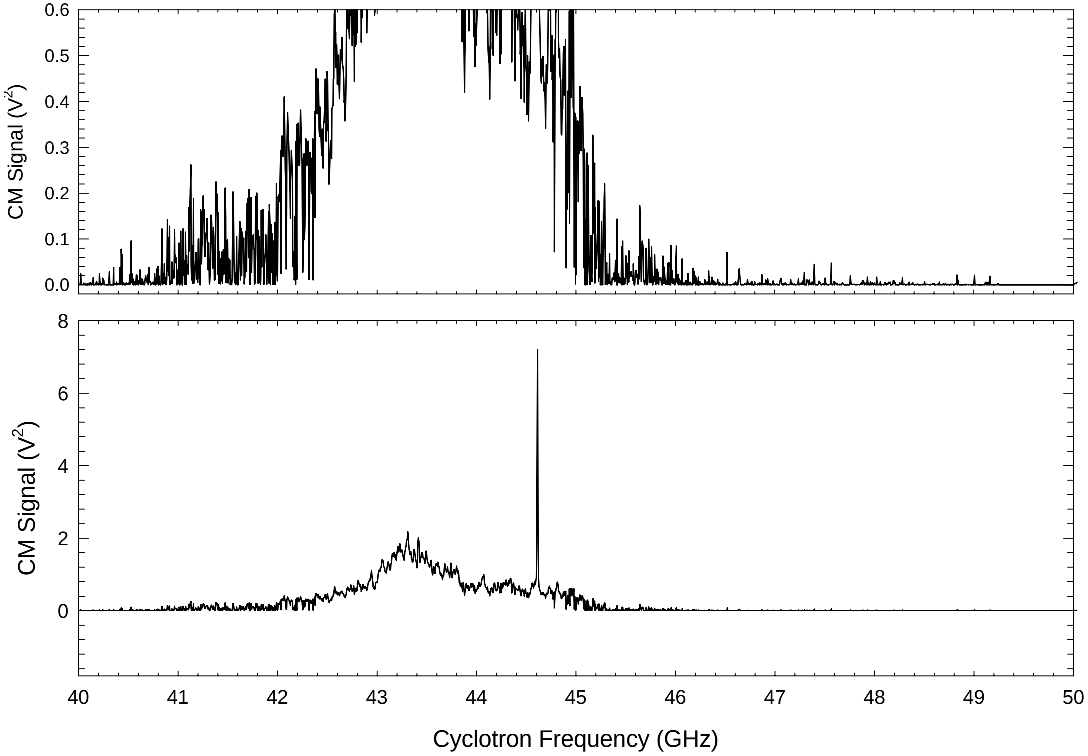
0.6
0.5
0.4
0.3
0.2
0.1
0.0
CM Signal (V^2)
8
6
4
2
0
CM Signal (V^2)
40
41
42
43
44
45
46
47
48
49
50
Cyclotron Frequency (GHz)

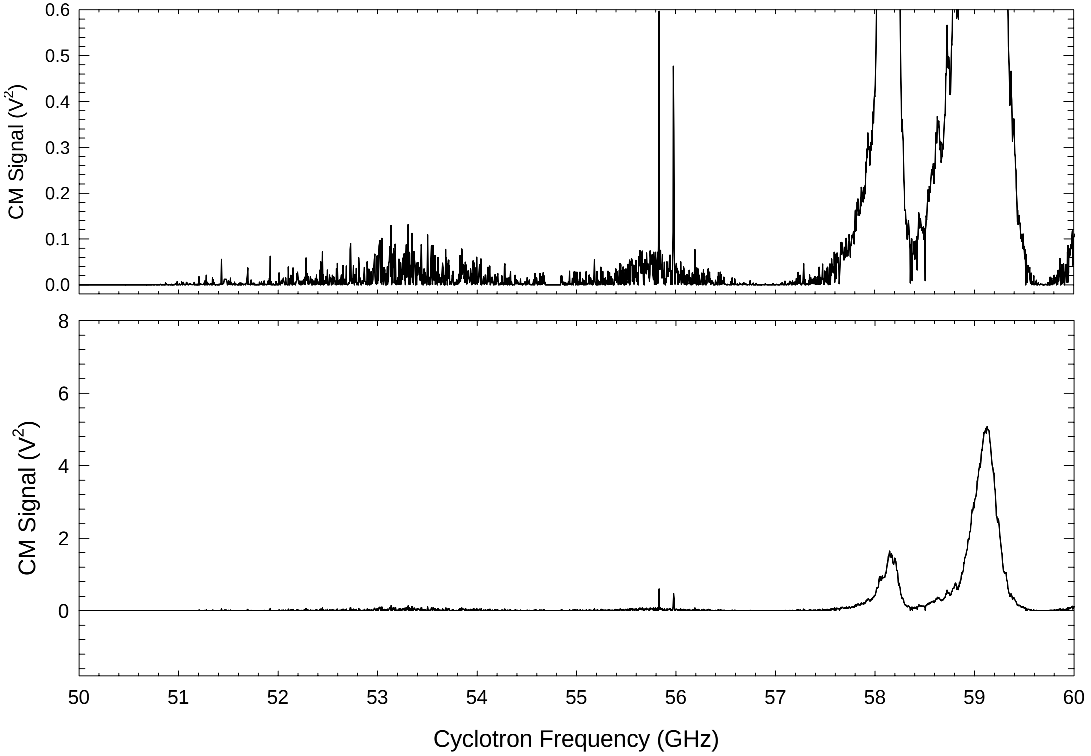

CM Signal (V^2)
0.6
0.5
0.4
0.3
0.2
0.1
0.0
CM Signal (V^2)
8
6
4
2
0
50
51
52
53
54
55
56
57
58
59
60
Cyclotron Frequency (GHz)

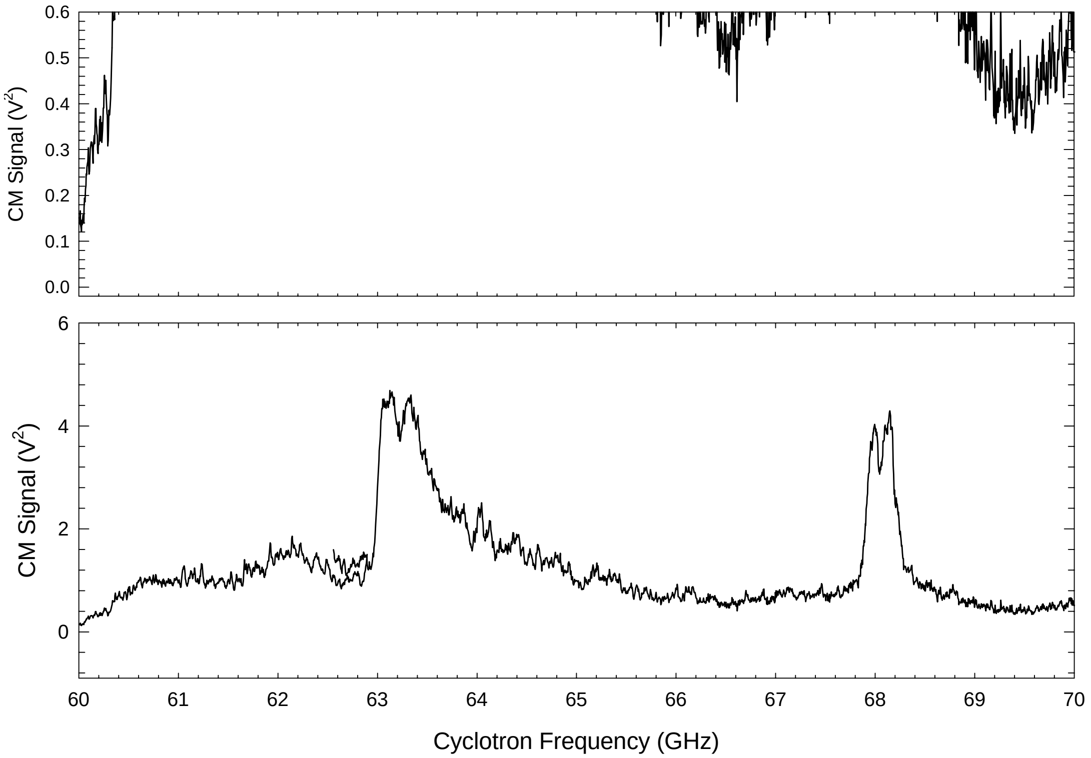
0.6
0.5
0.4
0.3
0.2
0.1
0.0
CM Signal (V^2)
6
4
2
0
CM Signal (V^2)
60
61
62
63
64
65
66
67
68
69
70
Cyclotron Frequency (GHz)

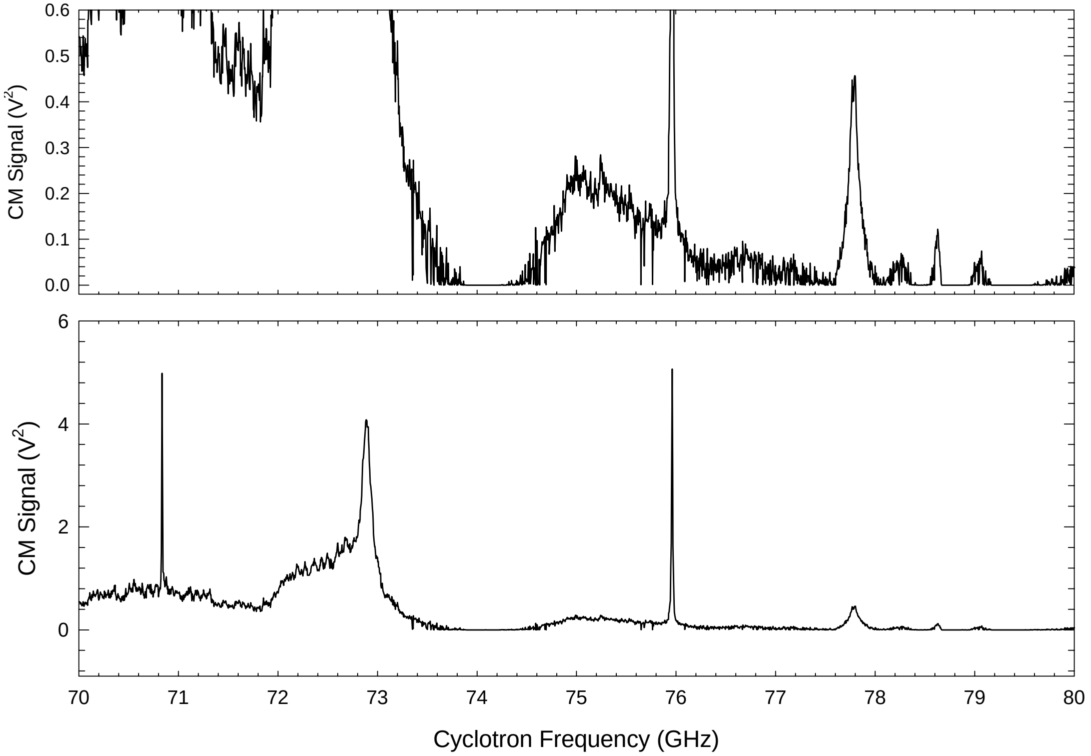
0.6
0.5
0.4
0.3
0.2
0.1
0.0
CM Signal (V^2)
6
4
2
0
CM Signal (V^2)
70
71
72
73
74
75
76
77
78
79
80
Cyclotron Frequency (GHz)

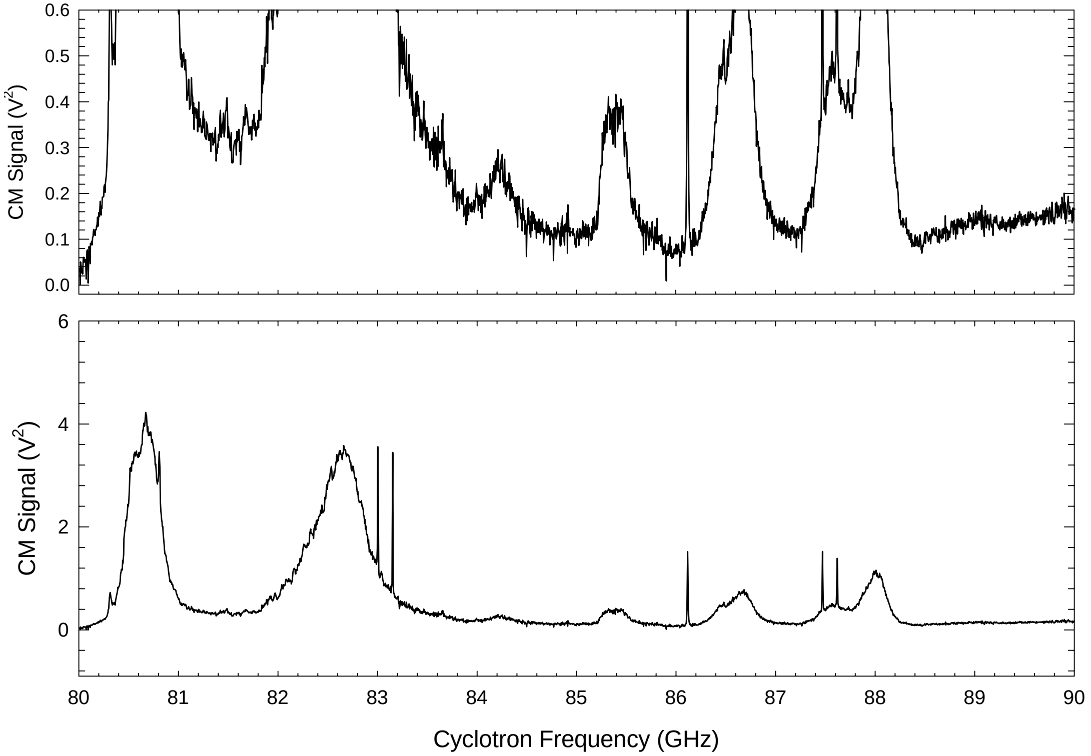
CM Signal (V^2)
0.0
0.1
0.2
0.3
0.4
0.5
0.6
CM Signal (V^2)
0
2
4
6
80
81
82
83
84
85
86
87
88
89
90
Cyclotron Frequency (GHz)

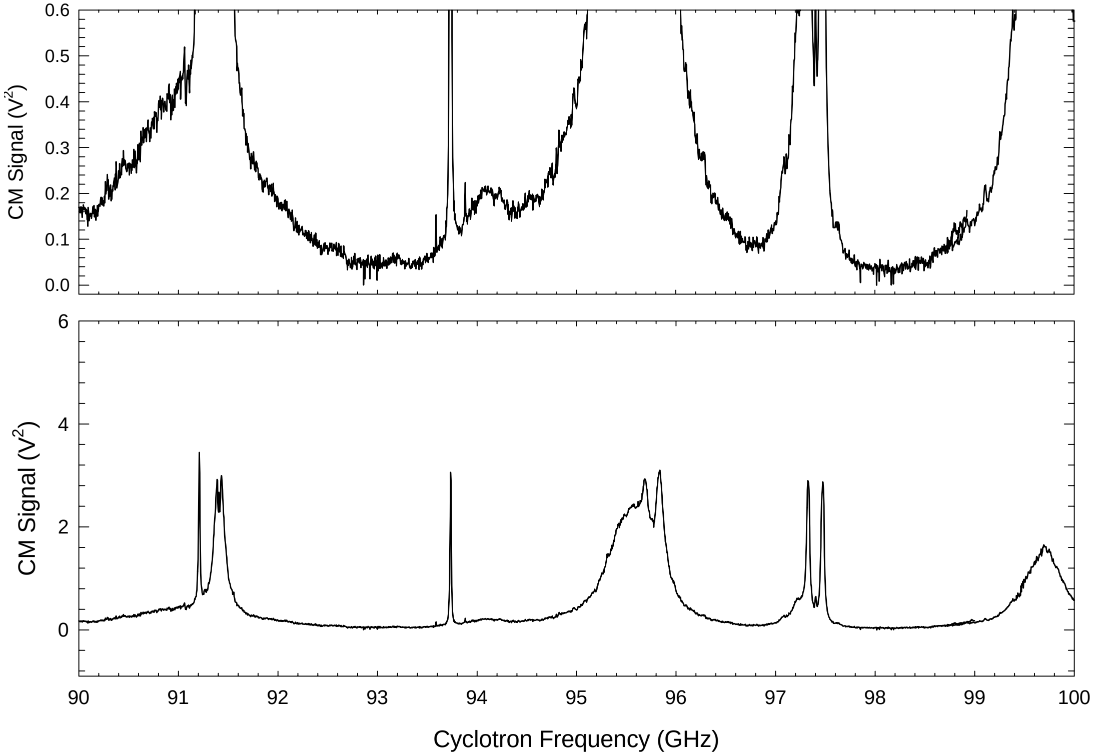
CM Signal (V^2)
0.6
0.5
0.4
0.3
0.2
0.1
0.0
CM Signal (V^2)
6
4
2
0
90
91
92
93
94
95
96
97
98
99
100
Cyclotron Frequency (GHz)

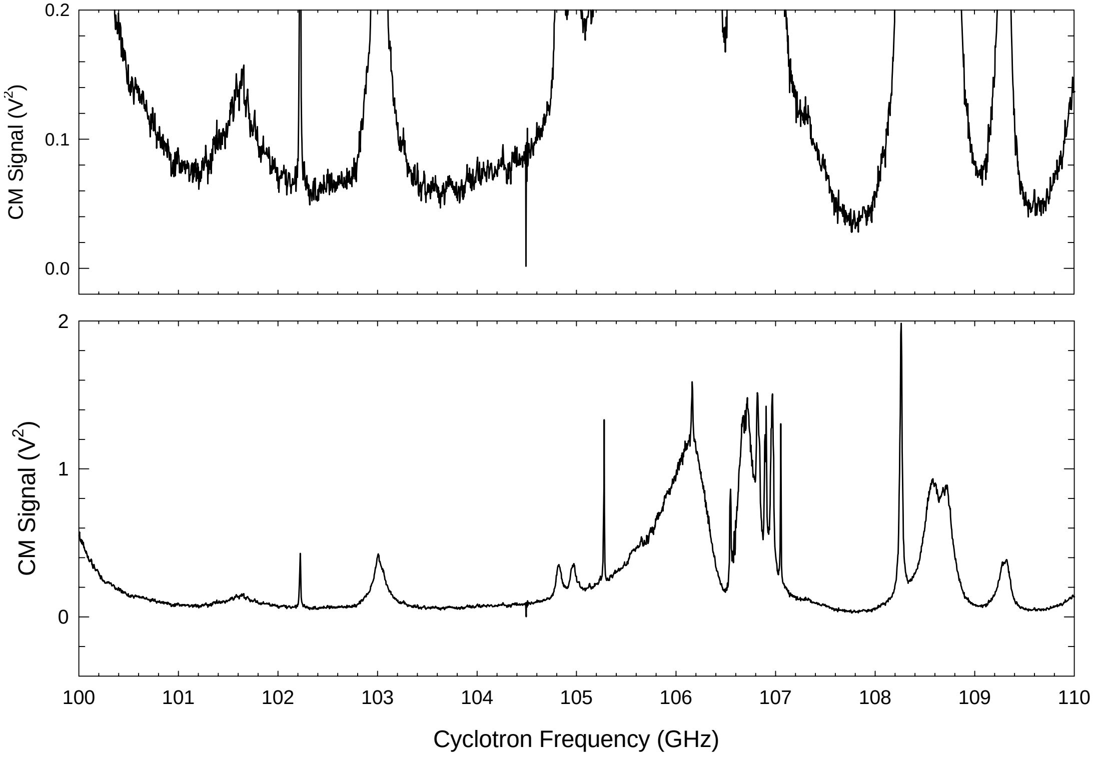
0.2
0.1
0.0
CM Signal (V^2)
2
1
0
CM Signal (V^2)
100
101
102
103
104
105
106
107
108
109
110
Cyclotron Frequency (GHz)

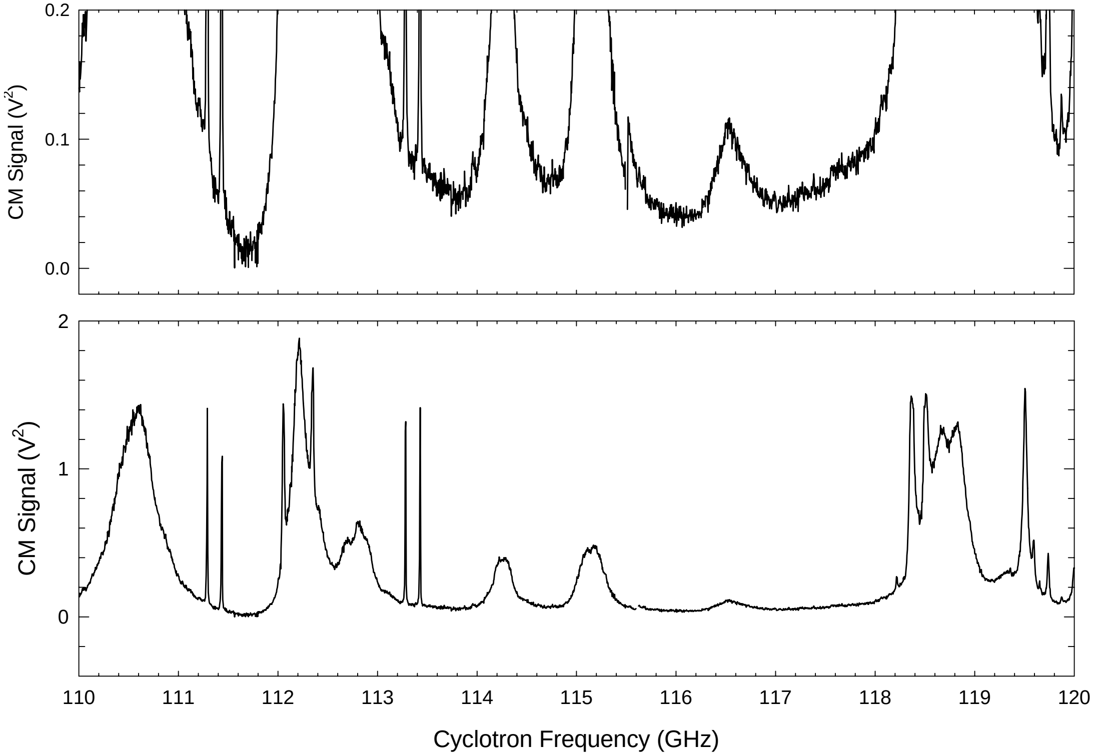
0.2
0.1
0.0
CM Signal (V2)
2
1
0
CM Signal (V2)
110
111
112
113
114
115
116
117
118
119
120
Cyclotron Frequency (GHz)

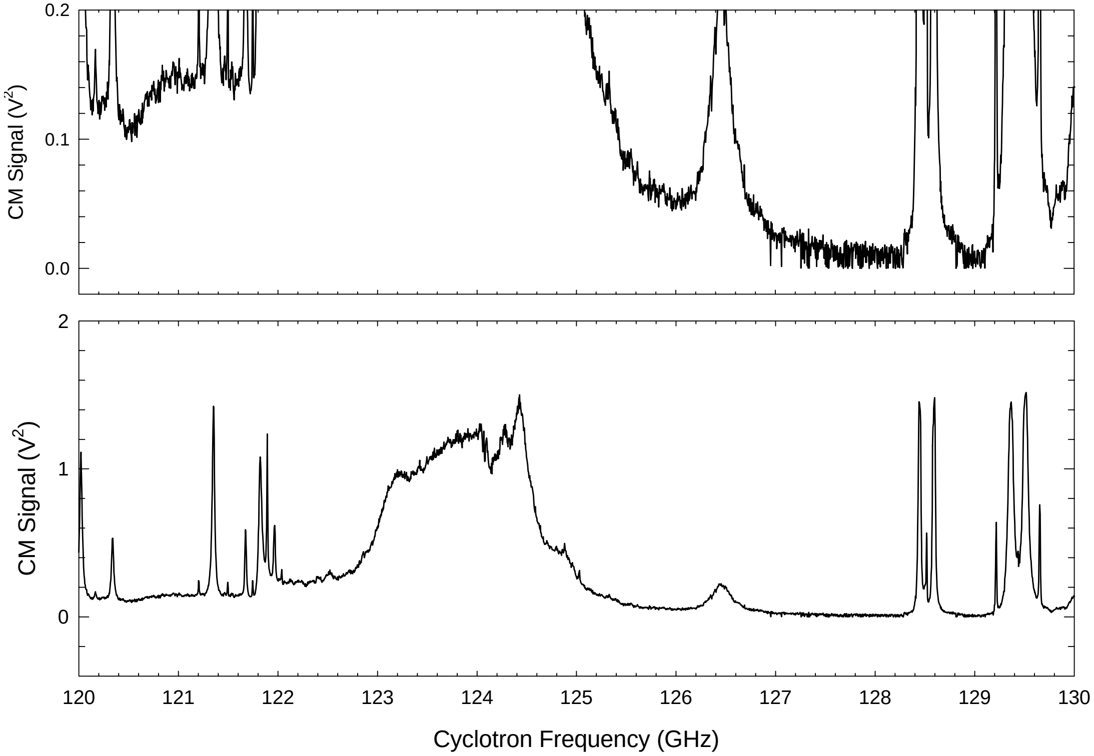
0.2
0.1
0.0
CM Signal (V^2)
2
1
0
CM Signal (V^2)
120
121
122
123
124
125
126
127
128
129
130
Cyclotron Frequency (GHz)

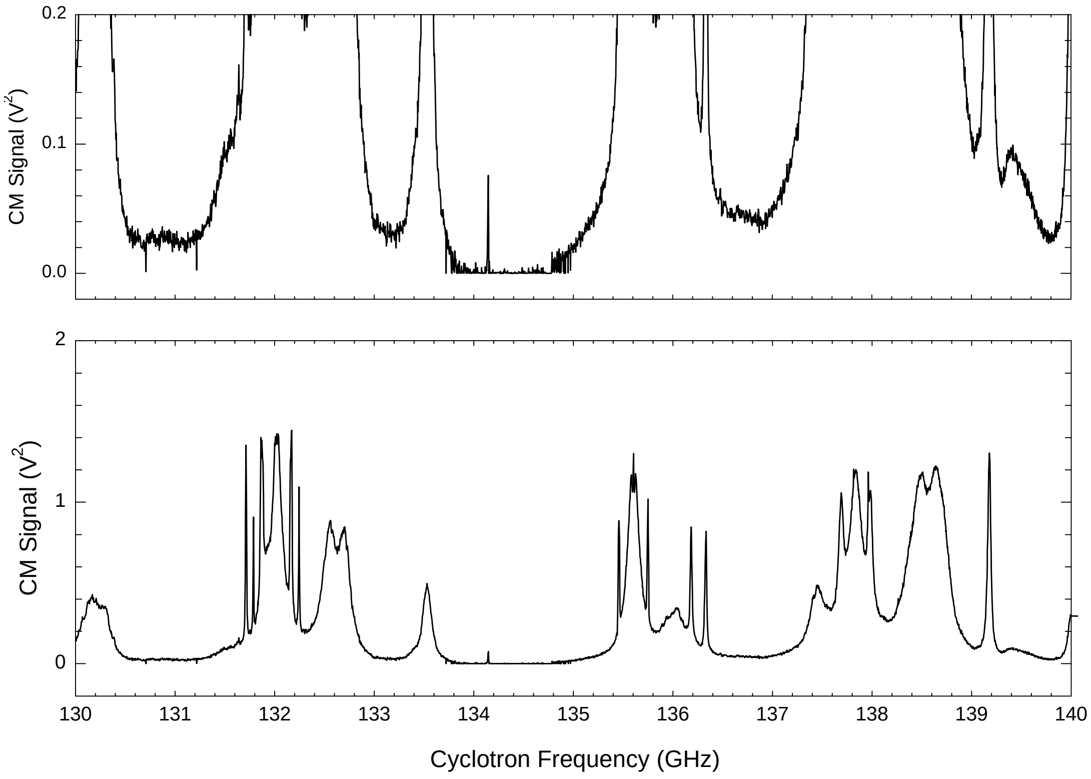
0.2
0.1
0.0
CM Signal (V^2)
2
1
0
CM Signal (V^2)
130
131
132
133
134
135
136
137
138
139
140
Cyclotron Frequency (GHz)

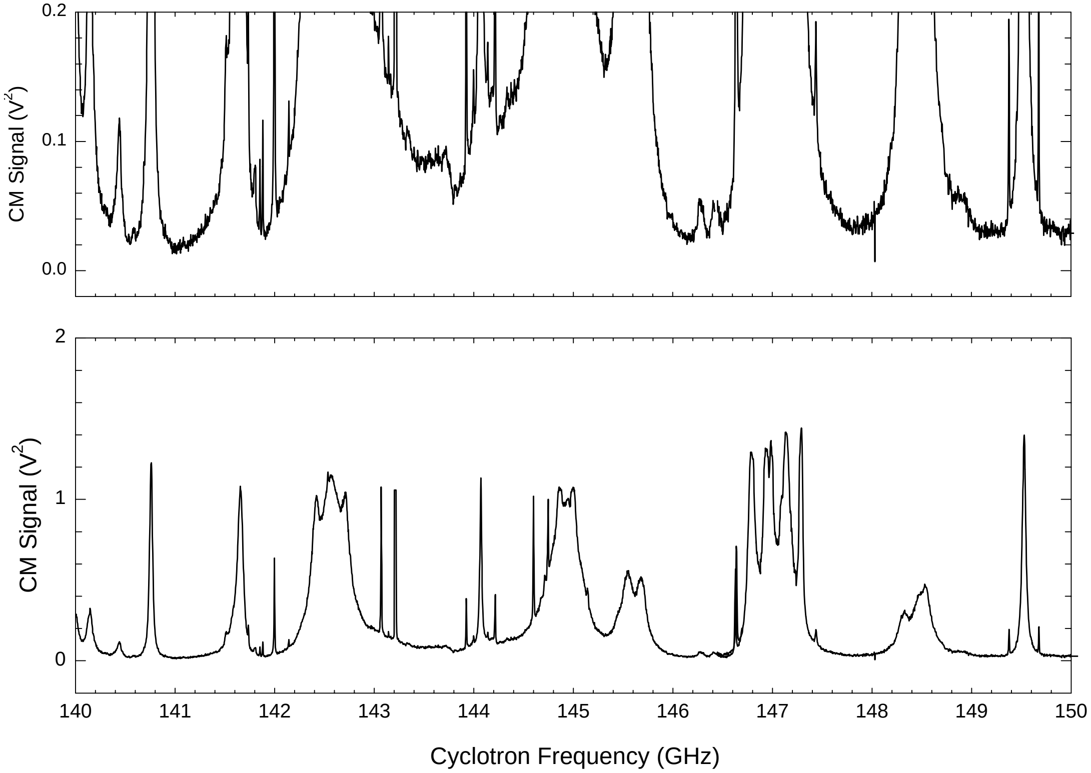
0.2
0.1
0.0
CM Signal (V^2)
2
1
0
CM Signal (V^2)
140
141
142
143
144
145
146
147
148
149
150
Cyclotron Frequency (GHz)

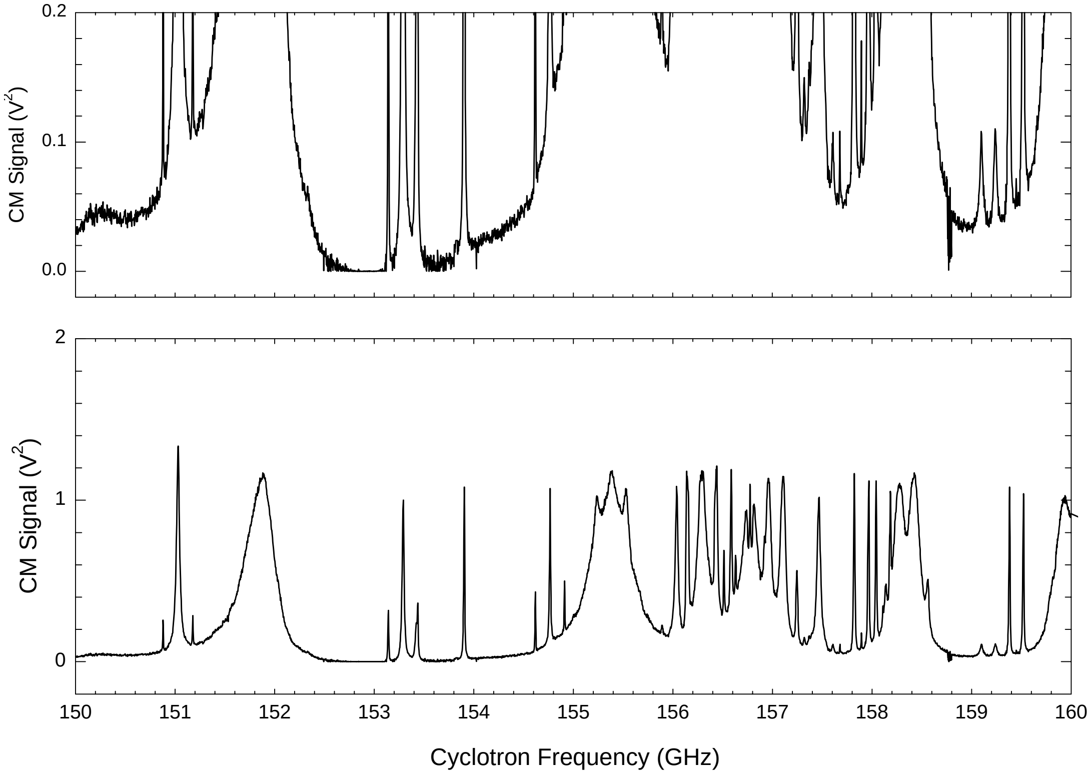
0.2
0.1
0.0
CM Signal (V^2)
2
1
0
CM Signal (V^2)
150
151
152
153
154
155
156
157
158
159
160
Cyclotron Frequency (GHz)

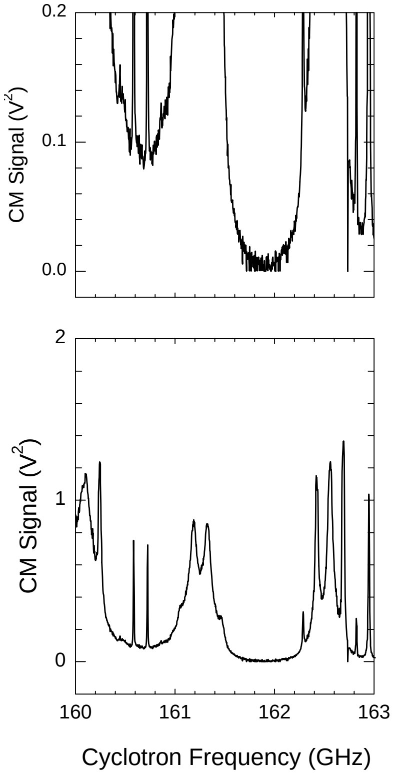
0.2
0.1
0.0
CM Signal (V2)
2
1
0
CM Signal (V2)
160
161
162
163
Cyclotron Frequency (GHz)

Chapter 2

Experimental Apparatus

2.1 Cylindrical Trap

The first Penning traps were made of electrodes that closely followed the quadrupole equipotential surfaces [20]. The endcaps were hyperboloids and the ring had a hyperbolic cross section. The cavity mode structure was very difficult to calculate [34] and the modes detected were not well separated and hard to identify [24,26]. The inhibited emission of the electron synchrotron radiation was the leading systematic uncertainty in the measurement of the anomalous electron magnetic moment [26].

To produce a more easily understood set of radiation modes, a new type of trap was proposed that approximated a right circular cylinder [21]. The cavity modes for this geometry are easily understood as described in Chapter 1. To make the five separate electrodes closely resemble an ideal cylindrical cavity, the OFHC copper electrodes were machined to a precision of better than 0.001 inch, the surfaces were polished to have a high degree of reflectivity and gaps between the electrodes have been minimized and contain choke flanges. The cavity modes for this trap were measured and shown to be well separated and of high quality (see Fig. 1.4). The trap also contains a waveguide to pass microwaves into the trap (for cyclotron frequency measurements) and a tungsten field emission point (FEP) to load electrons into the trap. (see Fig. 2.1)

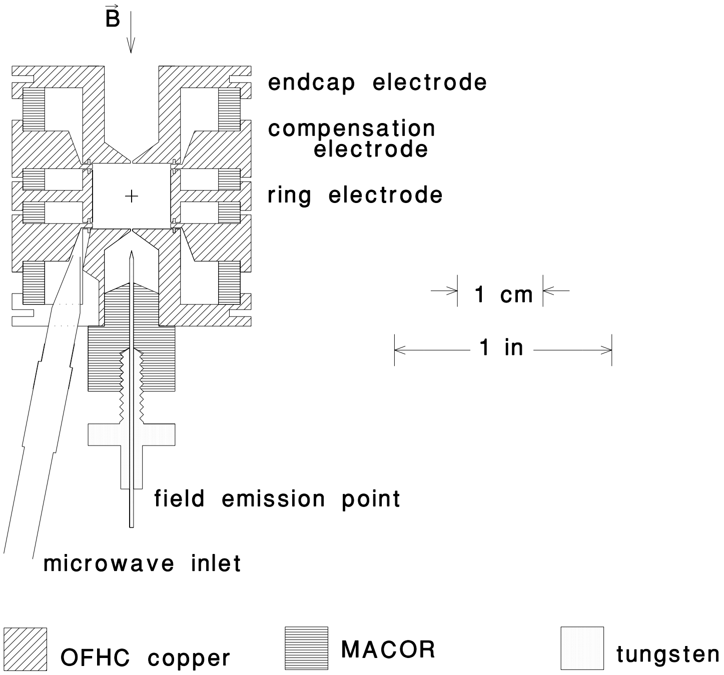
$\vec{B}$
endcap electrode
compensation electrode
ring electrode
1 cm
1 in
field emission point
microwave inlet
OFHC copper
MACOR
tungsten

Figure 2.1: Cross section of cylindrical Penning trap

The challenge of designing this trap was to produce a sufficiently good electrostatic quadrupole potential to allow the observation of a single trapped electron. This was accomplished with two annular compensation electrodes located between the ring and the endcaps that are used to tune out the higher order anharmonic terms in the potential due to the fact that the equipotential surfaces are not hyperboloids. These compensation electrodes are more prominent than those of a hyperbolic trap but the voltage can be set to make C_4 approach zero. $C_6 \approx 0.1$ is relatively unaffected by the compensation voltage; it is larger than that of a hyperbolic trap, but is still small enough so as not to interfere with the detection of small numbers of particles.

2.2 Cryostat

The trap is enclosed in a sealed vacuum can which is coupled to a liquid helium reservoir, thereby achieving a high quality vacuum through cryopumping without the use of any

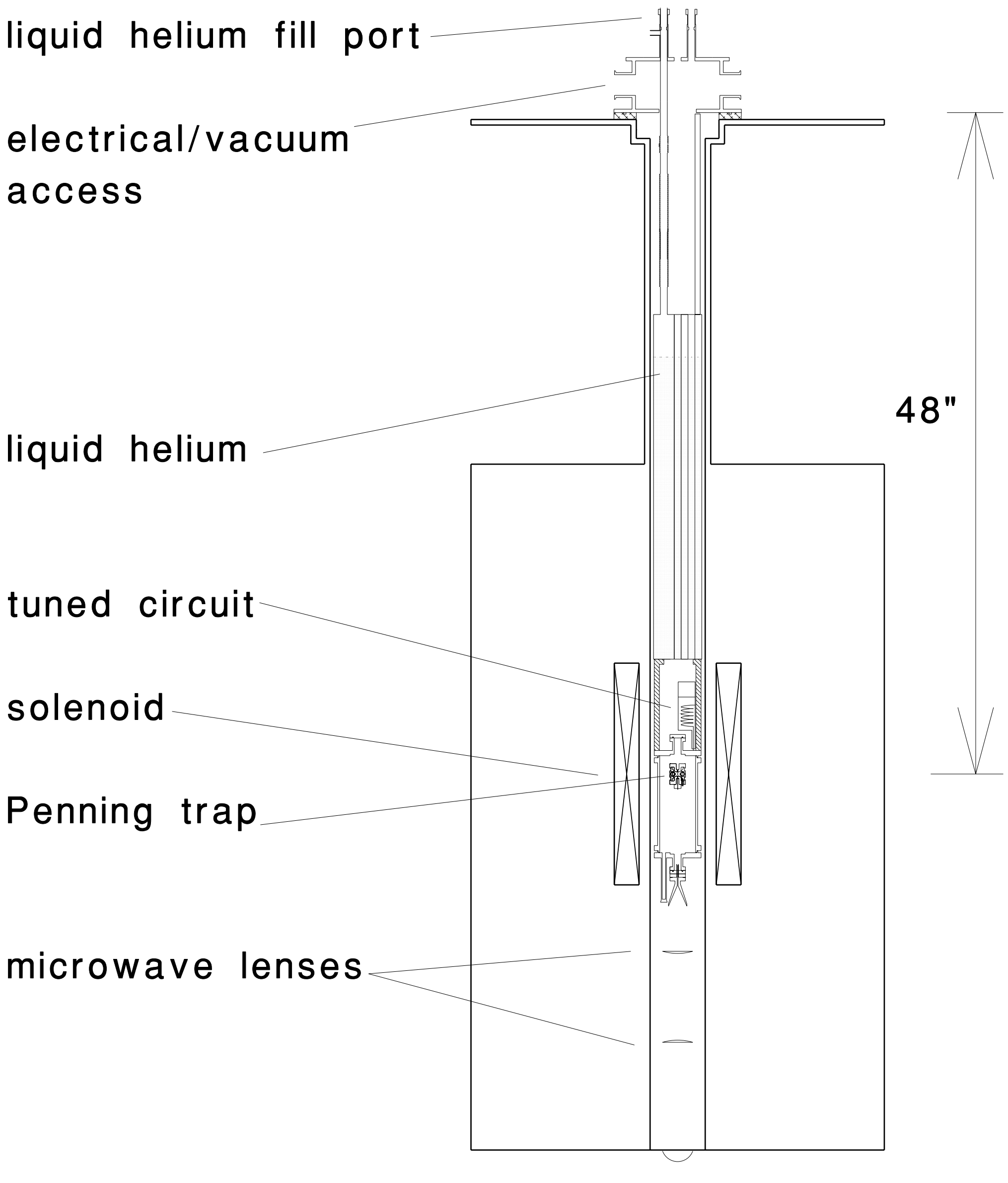
liquid helium fill port
electrical/vacuum access
liquid helium
48"
tuned circuit
solenoid
Penning trap
microwave lenses

Figure 2.2: Cold finger dewar system

mechanical pump. Two different schemes of coupling the trap to a liquid helium reservoir were used in this experiment. The first was a cold finger system where the trap can is suspended below a dewar and cooled conductively through a structure of OFHC copper (see Fig. 2.2). The entire system is suspended in the bore of the magnet which is evacuated to provide long “hold time” of liquid helium in the dewar (5 days). This system easily cools the vacuum can and electrodes but not the FET which provides the first stage of amplification of the axial signal (see section 2.4) and sits just above the vacuum can but is not well heat sunk to the dewar. It will be shown later that the power generated by the FET dissipates quite a lot of heat which couples back into the electron plasma and destroys the synchronization. Therefore, the experiment was continued in a bucket dewar system where the vacuum can, amplifier and all other electronics near the trap are submerged in a large dewar filled with liquid helium (see Fig. 2.3). The FET is then maintained much closer to 4 K regardless of the power dissipated.

2.3 Superconducting Magnet

The magnetic field is provided by a superconducting solenoid that can carry up to 40 Amps, creating a field at the center of a solenoid of up to 6 Tesla. This field can be precisely controlled by a power supply and a superconducting switch. The power supply provides a current given by

$$I(t) = \frac{V}{R} + J(t) \tag{2.1}$$

where V is the voltage provided by the power supply, R is the shunt resistance in the power supply provided by a protection resistor and the superconducting switch, and $J(t)$ is the current in the solenoid. Since the rate of current change in a solenoid depends inversely on the inductance of the solenoid, the solenoid current is given by

$$J(t) = J(0) + \frac{V}{L}t \tag{2.2}$$

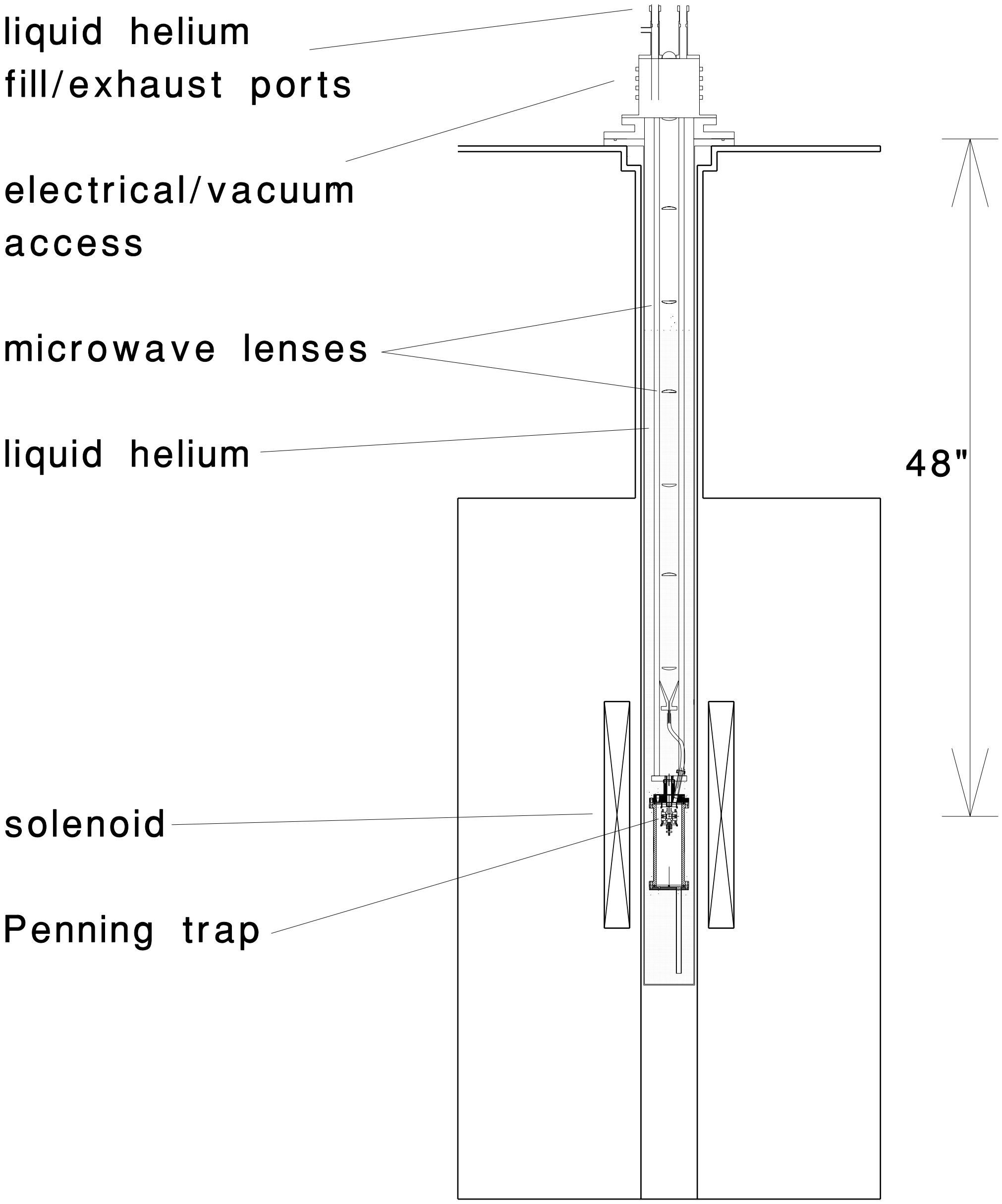
liquid helium
fill/exhaust ports
electrical/vacuum
access
microwave lenses
liquid helium
48"
solenoid
Penning trap

Figure 2.3: Bucket dewar system

and the magnetic field is

$$B(t) = g\left[J(0) + \frac{V}{L}t\right] \tag{2.3}$$

where g depends on the geometry of the solenoid. The current produced by the power supply, I(t), is what is experimentally monitored. Therefore it is convenient to define a time constant as

$$\frac{V}{R} = \frac{V}{L}\tau_o \tag{2.4}$$

such that the magnetic field is given by

$$B(t) = g\left[I(0) + \frac{V}{L}(t - \tau_o)\right]. \tag{2.5}$$

The measured cyclotron frequency is

$$\nu_c = \frac{e}{m}g\left[I_{meas} - \frac{V}{L}\tau_o\right] \tag{2.6}$$

where eg/m is the factor that converts the solenoid current to cyclotron frequency for $dI/dt = 0$. By using a microwave source to excite the cyclotron oscillator, the conversion for Nalorac magnet 43 is experimentally determined to be

$$\frac{eg}{m} = \frac{\nu_c}{I} = 4.1397\,\mathrm{GHz/A}. \tag{2.7}$$

The time constant τ_o is determined by using a high Q cavity mode as a marker during sweeps of various speeds of the magnetic field. If the current of this marker is plotted versus the sweep rate, the slope of the resulting line gives τ_o (see Fig. 2.4).

When a mode map is made, data is simultaneously collected on the center-of-mass amplitude of the electron plasma, the current in the power supply and the time ($\sim$ 3 points/sec). The sweep rate is determined by fitting the time-stamped current to a line. The fitted function generates a new set of current values that removes small amounts of jitter in the data due to inaccuracies in the shunt resistor. The new current values are

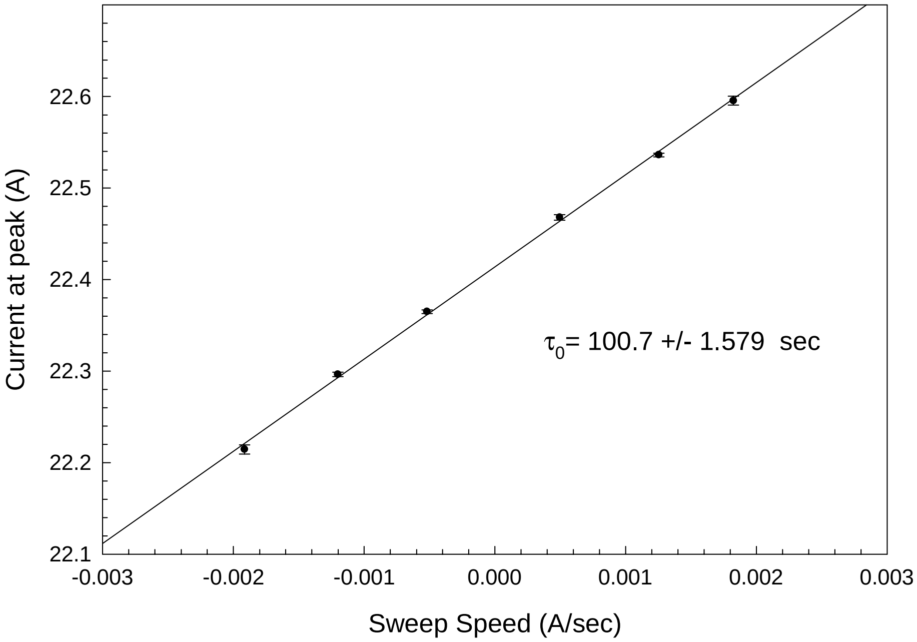

Figure 2.4: Calibration of effective time constant of magnet shunt resistor

adjusted with the sweep rate and converted to the cyclotron frequency with Eq. 2.6. This set of cyclotron frequencies are then plotted versus the center of mass amplitudes.

2.4 Detection

All information about the electrons in the trap is collected by the tuned circuit amplifier which measures the current induced in the endcaps by the electrons as they oscillate axially. The inductive amplifier is a six turn coil inside of a cylindrical can of OFHC copper. One end of the coil is grounded and the other end is connected to one endcap. The signal is tapped one turn from ground and capacitively coupled to a Mitsubishi dual gate GaAs FET. The trap and amplifier can be modeled as a parallel LRC circuit (see Fig. 2.5b) where the capacitance is determined by the electrodes and the inductance and resistance is determined by the coil. The Johnson noise in the resistor is amplified near

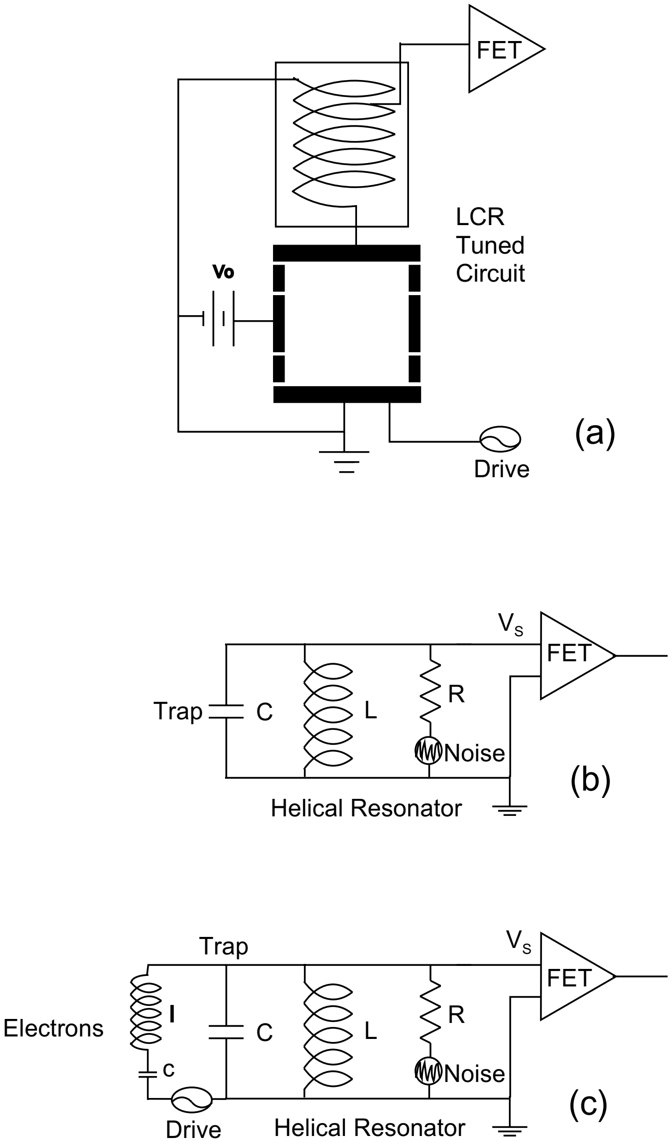
FET
LCR
Tuned
Circuit
Vo
(a)
Drive
Vs
FET
Trap
C
L
R
Noise
(b)
Helical Resonator
Trap
Vs
FET
Electrons
l
C
L
R
c
Noise
(c)
Drive
Helical Resonator

Figure 2.5: (a)The trap and inductive amplifier. (b)The equivalent LCR circuit which is resonant at $\omega_0^2 = 1/LC$. (c)The equivalent LCR circuit with the addition of electrons which short out the noise at $\omega_z^2 = 1/lc$.

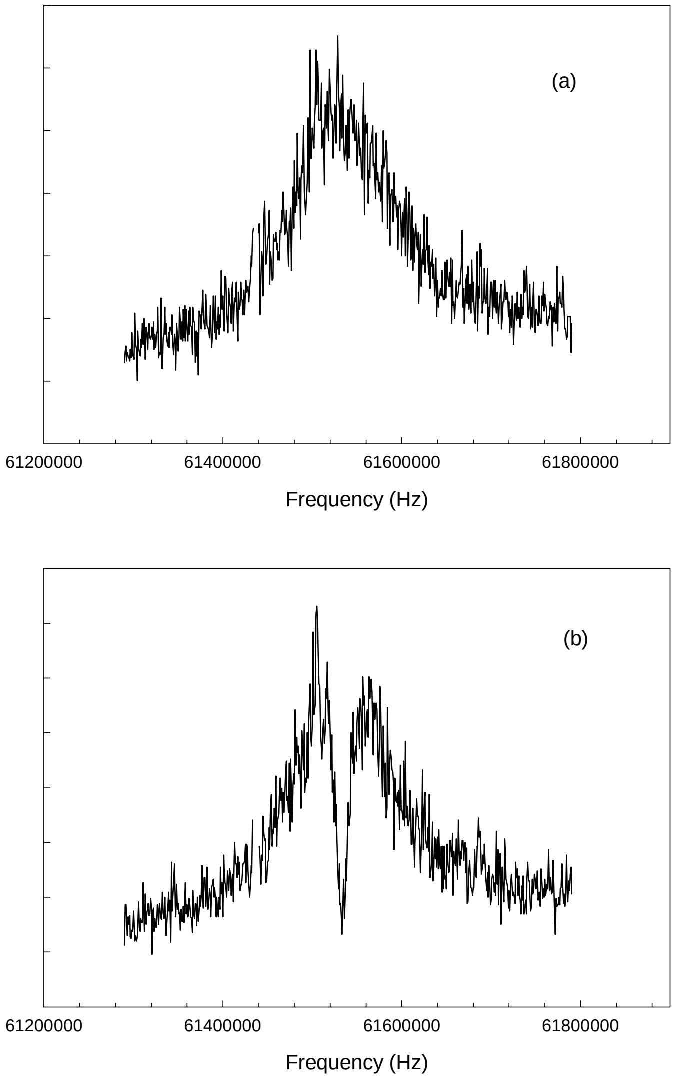

Figure 2.6: (a) Johnson noise induced in a tuned circuit. (b) Johnson noise shorted by approximately 1000 resonantly tuned electrons.

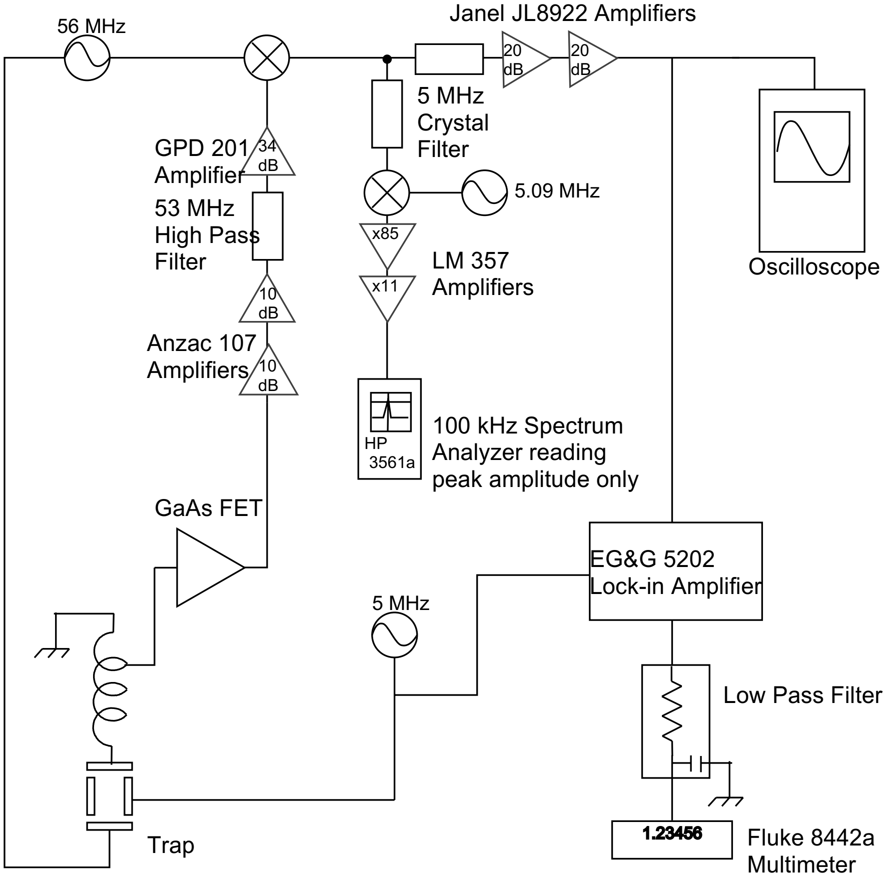
Janel JL8922 Amplifiers
56 MHz
20 dB
20 dB
5 MHz Crystal Filter
GPD 201 Amplifier
34 dB
5.09 MHz
53 MHz High Pass Filter
x85
x11
LM 357 Amplifiers
Oscilloscope
10 dB
Anzac 107 Amplifiers
10 dB
HP 3561a
100 kHz Spectrum Analyzer reading peak amplitude only
GaAs FET
EG&G 5202 Lock-in Amplifier
5 MHz
Low Pass Filter
1.23456
Trap
Fluke 8442a Multimeter

Figure 2.7: Detection scheme for electrons in a Penning trap

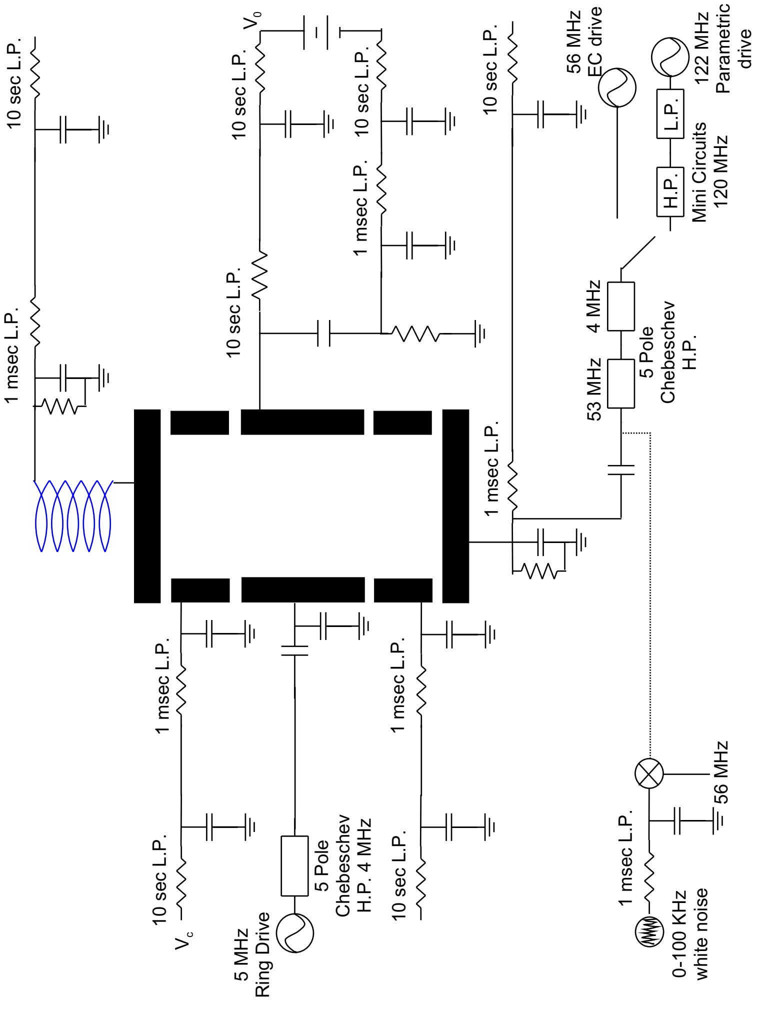
10 sec L.P.
1 msec L.P.
10 sec L.P.
V0
10 sec L.P.
1 msec L.P.
10 sec L.P.
10 sec L.P.
56 MHz
EC drive
122 MHz
Parametric
drive
L.P.
H.P.
Mini Circuits
120 MHz
4 MHz
53 MHz
5 Pole
Chebeschev
H.P.
1 msec L.P.
1 msec L.P.
10 sec L.P.
Vc
5 MHz
Ring Drive
5 Pole
Chebeschev
H.P. 4 MHz
1 msec L.P.
10 sec L.P.
56 MHz
1 msec L.P.
0-100 KHz
white noise

Figure 2.8: Filters applied to trap for noise suppression

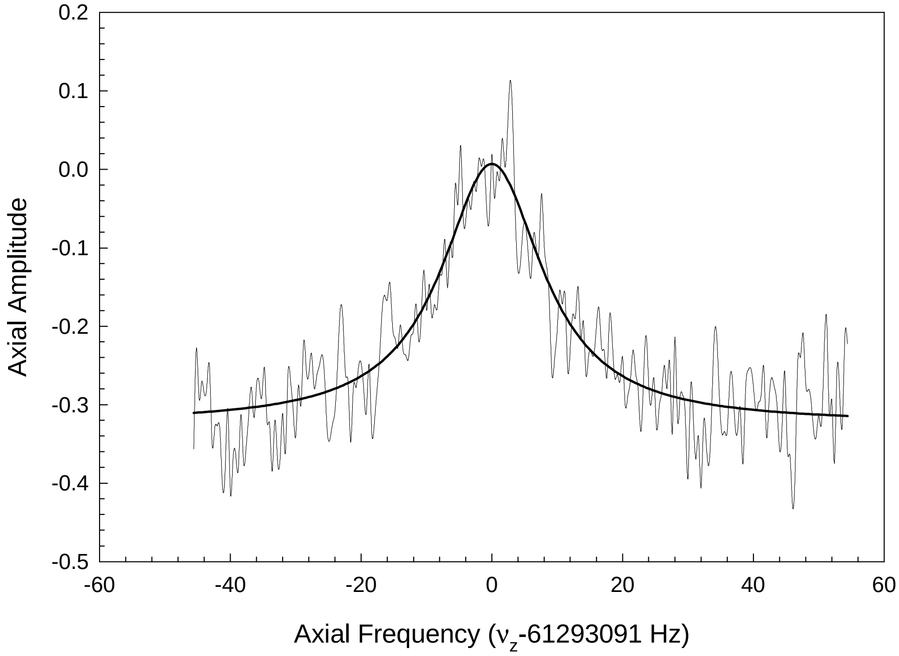

Figure 2.9: Coherent detection of one electron

the resonant frequency of the circuit in a Lorentzian form [35]

$$V_s^2 \propto \frac{R^2}{1+\left(\frac{RC}{\omega}\right)^2\left(\omega^2-\frac{1}{LC}\right)^2} \tag{2.8}$$

$$\propto \frac{R^2\left(\frac{1}{2\tau}\right)^2}{(\omega-\omega_0)^2+\left(\frac{1}{2\tau}\right)^2} \tag{2.9}$$

where $\omega_o^2 = 1/LC$ is the resonant frequency of the LCR circuit and $\tau = RC$ is the inverse of the damping rate and we have assumed $\omega \approx \omega_0$. The quality factor, $Q = \omega_0\tau$, of a resonance is made as large as possible to improve the signal to noise and is typically 500-800.

Electrons in the trap can be modeled as an inductor and capacitor in series (see Fig. 2.5c) [36]. This circuit is then placed in parallel with the LRC circuit of the trap and amplifier. When the natural frequency of the electron circuit (i.e. the axial frequency of the electrons given by Eq. 1.3) driven by thermal noise is resonant with the natural frequency of the amplifier and trap, the electrons “short out” the Johnson noise amplified by the circuit, creating a “dip” in the Lorentzian lineshape whose width is proportional to the number of electrons in the trap (see Fig. 2.6).

Though not impossible [37], it is difficult to see the signal from small numbers of electrons with the passive detection described above. Therefore a coherent detection scheme was employed most of the time to count the number of electrons in the trap. The axial signal is amplified at 4 K and at room temperature, filtered and mixed to a convenient frequency to and detected with a lockin amplifier (see Figs. 2.7 and 2.8. The phase is tuned so that the output signal is a Lorentzian in the frequency domain (see Fig. 2.9). The FWHM of the Lorentzian equals $N\gamma_z$ where N is the number of electrons and γ_z is the damping rate. Fig. 2.11 shows that for small numbers of electrons, the widths are discrete multiples of the width for one electron. The damping rate depends on the detuning of the axial frequency from the noise resonance; it is maximized when the detuning is zero and decreases linearly with the fractional height of the noise resonance, as is shown in Fig. 2.11. The maximal γ_z which is the FWHM of a single coherently detected electron, is approximately 14 Hz (See Fig. 2.10).

If the phase is tuned so that the output is a dispersive curve, the amplitude on the tail is proportional to the number of electrons. For sufficiently high drives and large filtering, the loading of individual electrons can be viewed in real time, allowing precise control of the number of electrons in the trap (see Fig. 2.10).

Though the electron motion is driven for coherent detection, the axial amplitude of the electrons is still quite small compared with the amplitude of the electrons when parametrically excited which can reach 10% of the length of the trap and which can be detected with a straight forward square law detection scheme (see Fig. 2.7). However, since the amplitude varies across a mode from the large oscillations mentioned above to essentially a thermal excitation, a detector with a very large dynamic range is required. Therefore the signal is mixed down to 90 kHz and fed into a Hewlett Packard 3561a spectrum analyzer

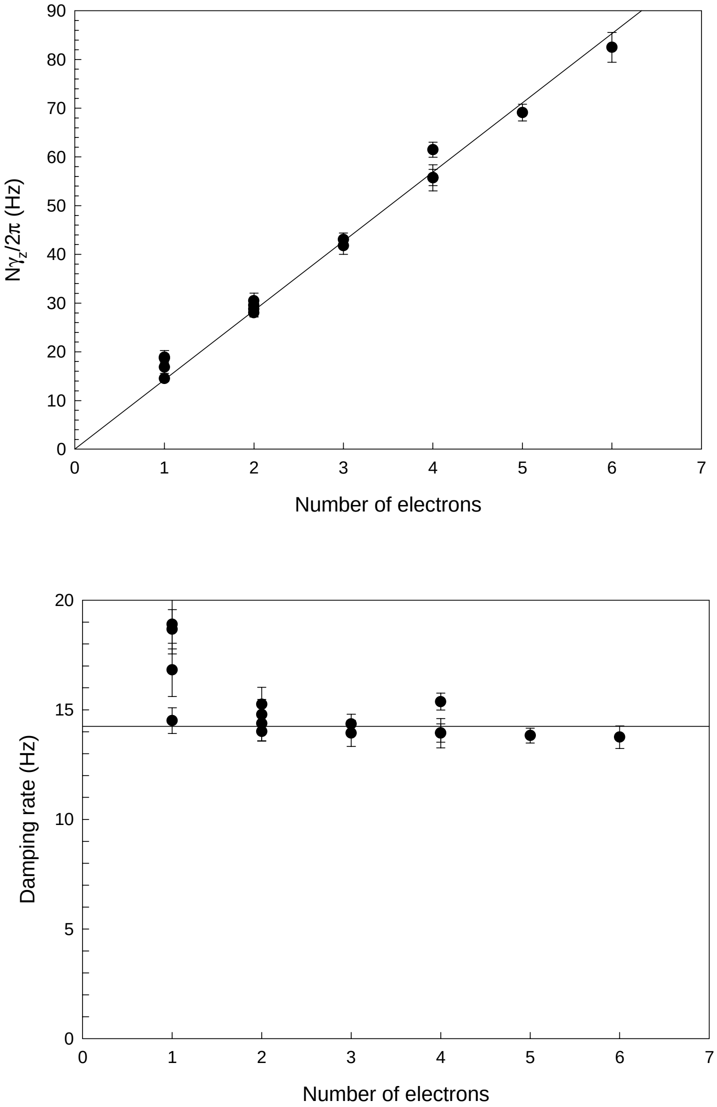

Figure 2.10: FWHM of coherently detected Lorentzian lineshapes for small numbers of electrons. The widths are clearly discrete multiples of the width for one electron.

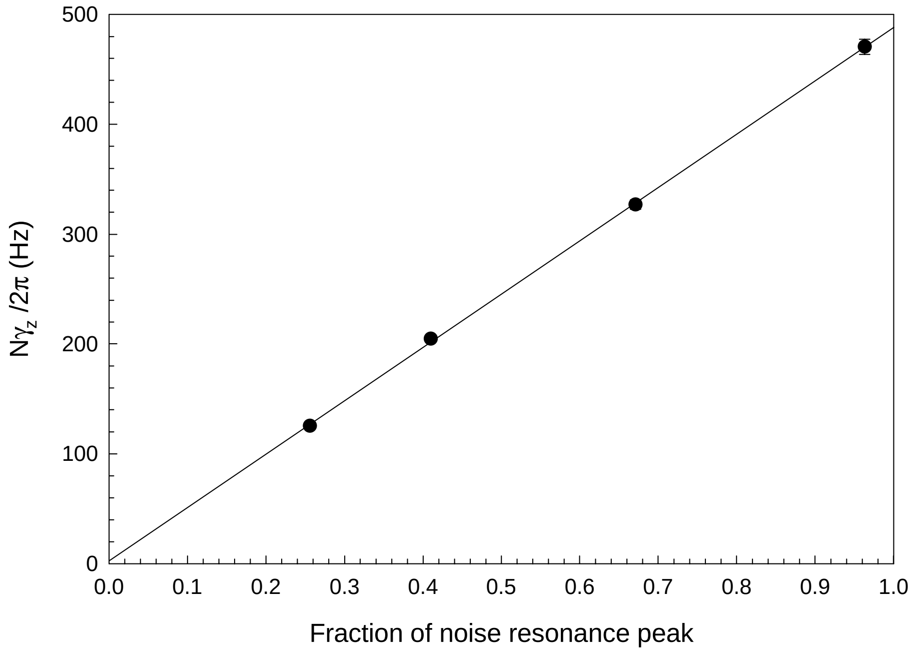

Figure 2.11: Amplitude of noise resonance relative to peak amplitude versus measured FWHM of a cloud of electrons

which returns the amplitude in the 90 kHz channel only. This signal is squared and passed to a computer which records all the data taken in this experiment. Fig 2.13 shows that most of the dynamic range is needed to adequately display certain modes.

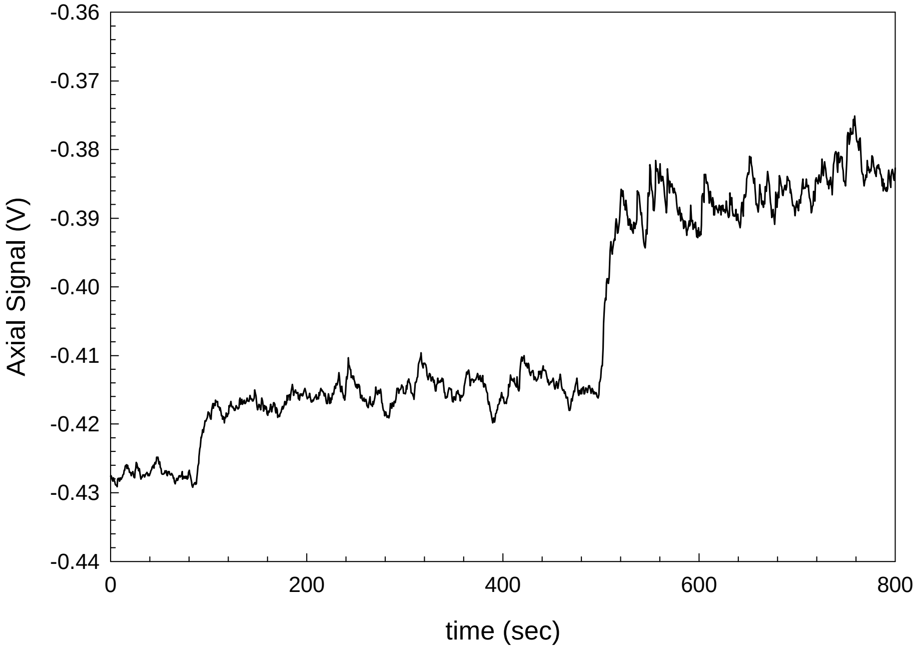

Figure 2.12: Successive loading of 3 electrons

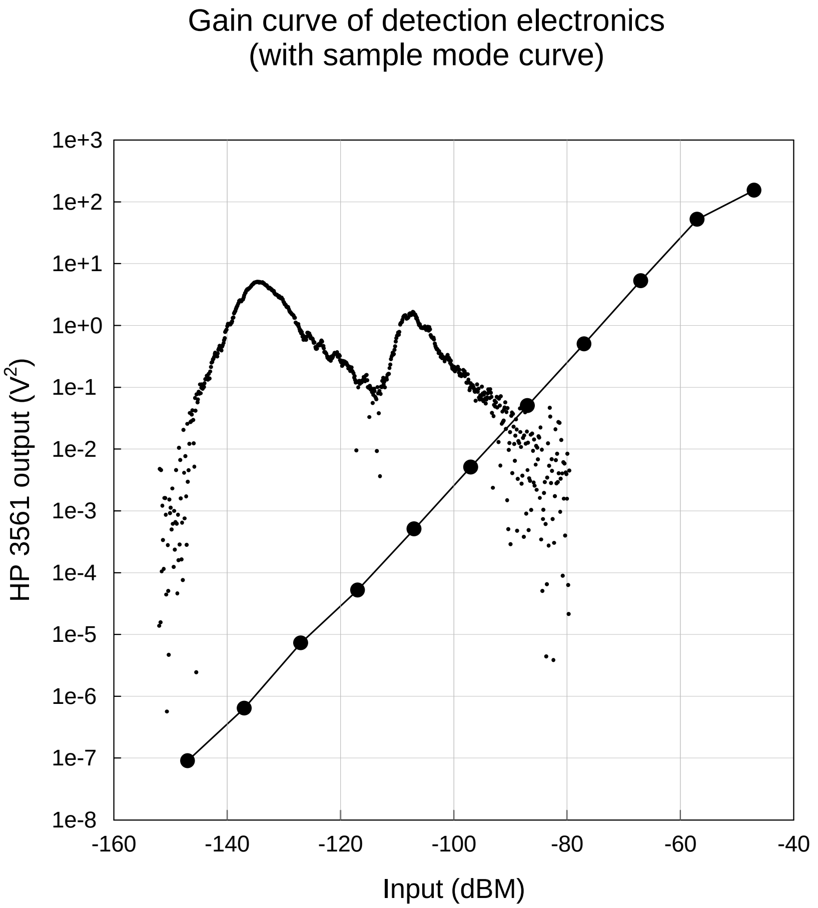

Figure 2.13: Linearity of complete detection circuit and a typical measured cavity mode

Chapter 3

Parametric Excitation of One Electron

The phenomenon of a one dimensional, parametrically excited oscillator is well understood. Simply stated, an oscillator that is driven above a threshold strength at twice its natural frequency will respond with a large amplitude at the natural frequency [38, 39]. If the oscillator is undamped, the amplitude of the response increases exponentially over time without bound. The damping and anharmonicity of the actual system keep the amplitude finite. In this chapter we build on the demonstration by Tseng et. al. [12] that the axial motion of one electron in a Penning trap is a good approximation of an ideal parametrically excited oscillator. Using the model of the parametric oscillator, we measure the axial amplitude by calibrating the gain in the detection circuit. In the next chapter we will compare what we observe with one electron to what is observed for the center of mass motion of more than one electron, which was first studied by Tan and Gabrielse [7], looking in particular for differences arising from the internal motions of the electrons.

3.1 Single Electron as a Parametric Oscillator

The equation of motion of the parametrically driven, anharmonic oscillator with charge Ne and mass Nm is given by

$$\ddot{Z} + N\gamma_z \dot{Z} + \omega_z^2(1 + h\cos\omega_d t)Z + \lambda_4\omega_z^2 Z^3 + \lambda_6\omega_z^2 Z^5 = 0. \tag{3.1}$$

We take Z to be the particle's axial position scaled by the trap dimension, d. The drive strength is given by h, ω_d is the drive frequency, and the anharmonicity coefficients, λ_n, can be expressed in terms of the coefficients of the Legendre expansion of the potential discussed in Chapter 1

$$\lambda_4 = \frac{2C_4}{1 + C_2} \tag{3.2}$$

$$\lambda_6 = \frac{3C_6}{1 + C_2}. \tag{3.3}$$

There occurs a resonant response at drive frequencies near

$$\omega_d \approx \frac{2\omega_z}{n}; \tag{3.4}$$

we will only consider $n = 1$ here because excitations from the higher harmonics are harder to produce. An excited solution, $Z \neq 0$, occurs only for frequencies defined by

$$\epsilon_- < \omega_d/2 < \epsilon_+ \tag{3.5}$$

$$\epsilon_\pm = \pm\frac{1}{4}\omega_z\sqrt{h^2 - h_T^2} \tag{3.6}$$

and for drive strengths above the threshold

$$h_T = \frac{2N\gamma_z}{\omega_z} \tag{3.7}$$

See Fig. 3.1 for the parameter space defined by Eqs. 3.6 and 3.7; an excitation only occurs

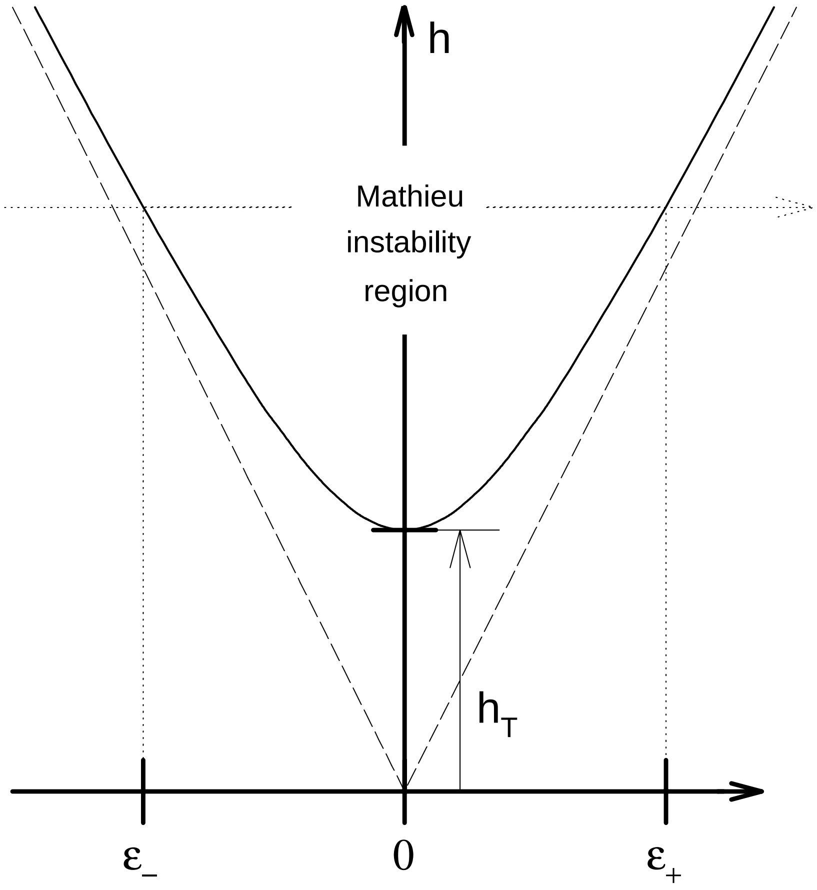
h
Mathieu
instability
region
h_T
ε_
0
ε_+

Figure 3.1: Dynamic regions of the parametric oscillator without anharmonicity ($\lambda_4, \lambda_6 = 0$)

within the hyperbolic Mathieu instability region.

The experimental observations well match the predictions of the previous paragraph. Fig. 3.2a shows that an excitation only occurs within a well defined region, which increases with drive strength, h, as seen in Fig. 3.3. Fig. 3.2b shows the sharp threshold for a single frequency. Hysteresis outside the hyperbola shown by Fig. 3.1 is observed in both frequency and drive strength. For example, for the lineshape shown in Fig. 3.4, if the drive frequency is moved from inside the hyperbola to a lower frequency outside the hyperbola, the excitation can be maintained [12].

Inside the hyperbola we have solutions to Eq. 3.1 of the form

$$Z(t) = A(t)\cos[(\omega_z + \epsilon)t + \Psi(t)] \tag{3.8}$$

where A(t) and $\Psi(t)$ are slowly varying and defined by the first order differential equations

$$\frac{dA}{dt} = \frac{\gamma_z}{2} A \left[1 - \frac{h}{h_T}\sin 2\Psi\right] \tag{3.9}$$

$$\frac{d\Psi}{dt} = -\epsilon + \frac{1}{4}h\omega_z\cos(2\Psi) + \frac{3}{8}\lambda_4\omega_z A^2 + \frac{5}{16}\lambda_6\omega_z A^4 \tag{3.10}$$

For the steady state solutions, $\dot{A} = 0$ and $\dot{\Psi} = 0$ which gives

$$\sin(2\Psi) = \frac{h}{h_T} \tag{3.11}$$

$$\frac{5\lambda_6\omega_z}{16}A_\pm^4 + \frac{3\lambda_4\omega_z}{8}A_\pm^2 + \epsilon_\pm - \epsilon = 0. \tag{3.12}$$

Eq. 3.11 is invariant under the transformation $\Psi \rightarrow \Psi + \pi$ which implies that the excited state is phase bistable. However, it will be shown in Chapter 4.2 that the bistability is not strictly preserved due to diffusion between the two stable states in the presence of noise. Eq. 3.12 implies that the lineshape of the squared amplitude (which is what is measured)

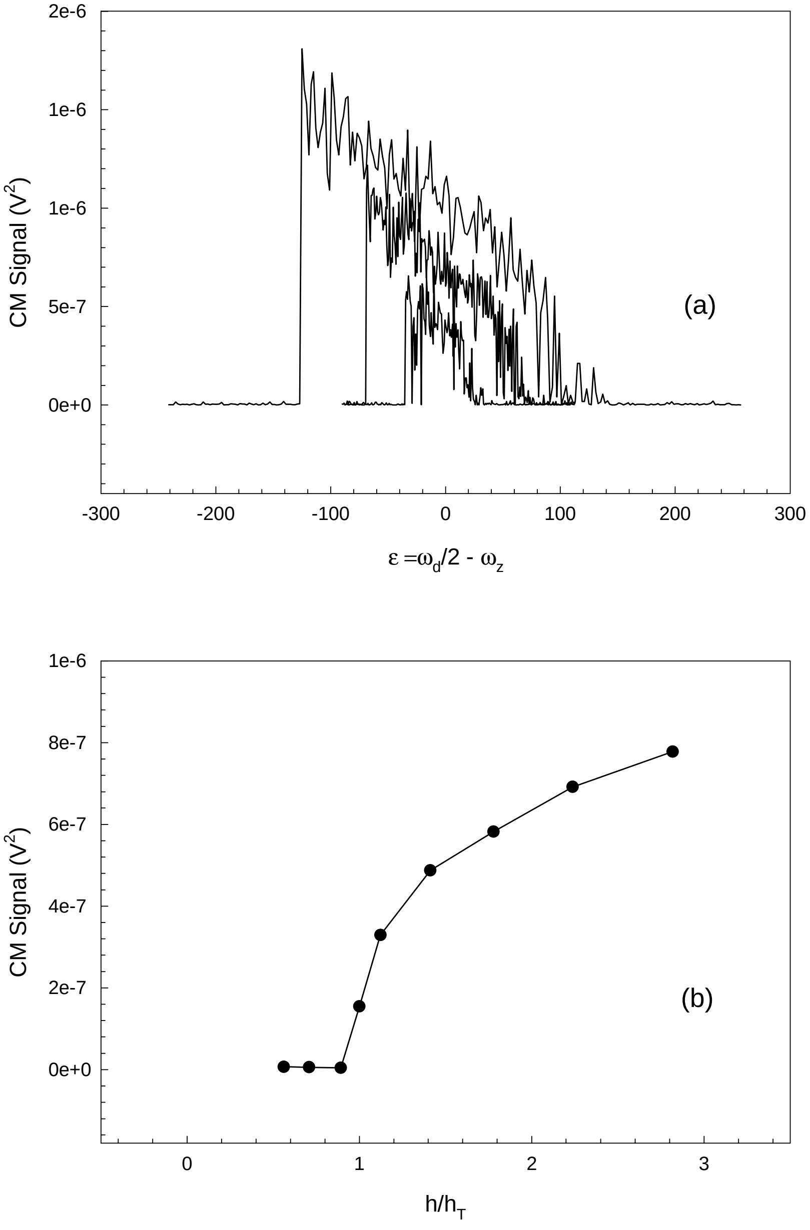

Figure 3.2: Parametric lineshapes (a) and amplitude at $\epsilon = 0$ (b) of one electron for various drive strengths

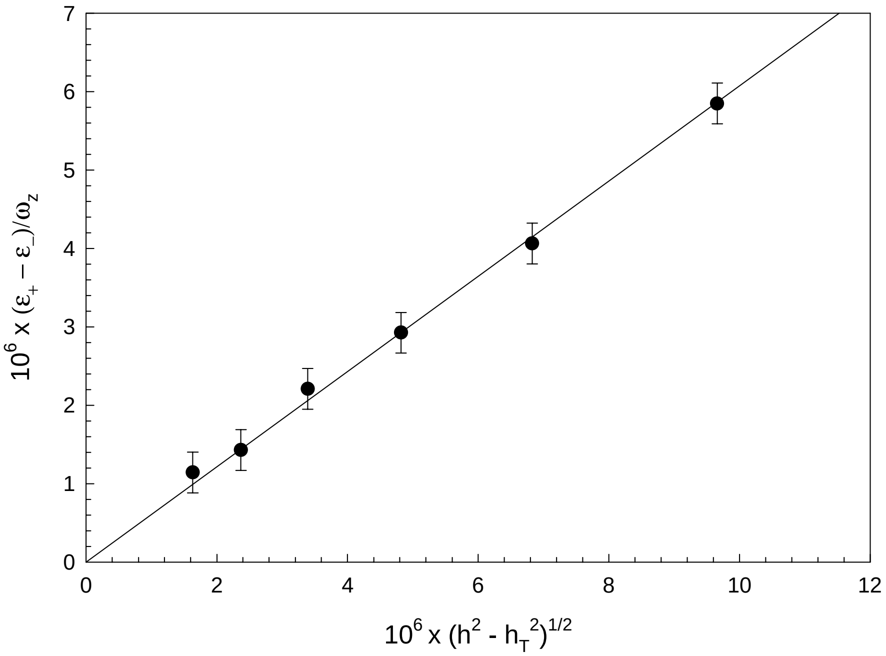

Figure 3.3: Parametric width versus drive strength for one electron

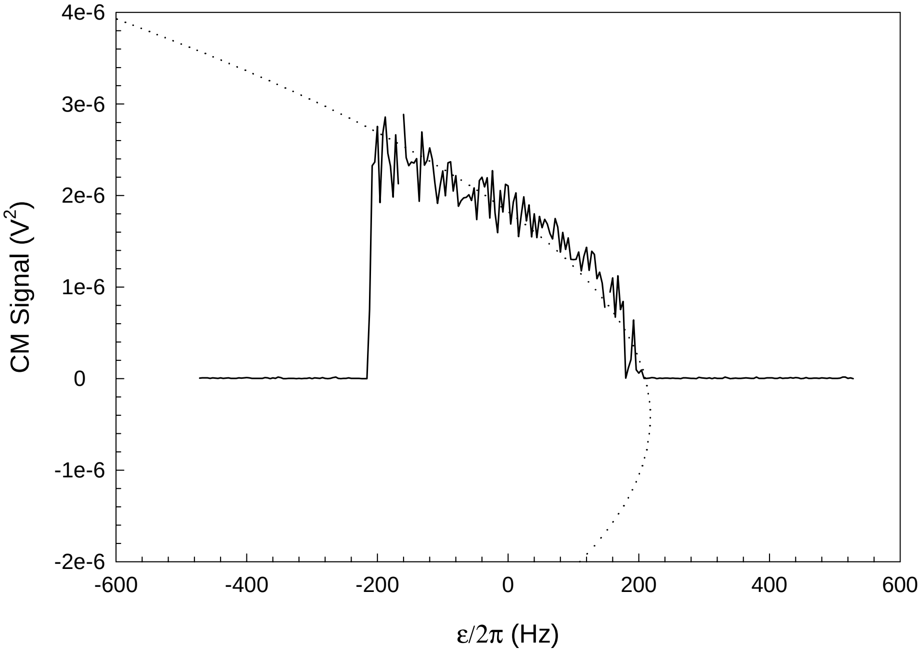

Figure 3.4: Parametric resonance with predicted parabolic lineshape

is a parabola with the exact parameters of the lineshape determined by the anharmonicity constants C_4 and C_6. As was discussed in Chapter 1, C_6 is relatively insensitive to the value of the compensation voltage, V_c, but that is not true for C_4. Therefore, when C_4 is small the lineshape of A^2 looks parabolic, but when C_4 is made to contribute much more than C_6, the lineshape is closer to a line (see Fig. 3.5).

3.2 Measurement of the Axial Excursion of One Electron

The electrical signal, S, which we observe, is directly proportional to the amplitude, A, of the electron axial motion and is given by

$$S = N\alpha A, \tag{3.13}$$

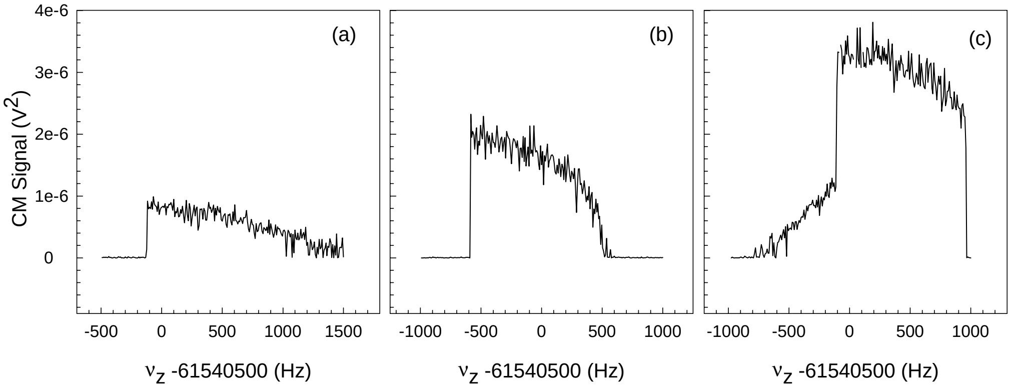

Figure 3.5: Parametric lineshapes for various C_4: (a) $C_4 = -3.86 \times 10^{-3}$; (b) $C_4 = 2.18 \times 10^{-4}$; (c) $C_4 = 2.81 \times 10^{-3}$

Calculated values	Measured values	α	error in α
D_4	m_b	0.0126	0.0015
C_4^0	b_b	0.0119	0.0013
C_4 and D_4	b (average)	0.0143	0.0043
D_4/D_6	m_b and m_a	0.0029	0.0105

Table 3.1: Measurements of α with one electron.

where α is a function of the gain in the detection circuit (never changed for any measurements) and $N = 1$. Deducing the amplitude of the axial motion, A, from the observed signal size, S, is extremely important for understanding the motion of many electrons.

For a drive strength much larger than threshold, h_T, we assume that electron acts as an ideal parametrically excited oscillator with a steady state amplitude, A, that depends on the drive frequency as

$$\frac{15C_6\omega_z}{16(1+C_2)}A_+^4 + \frac{3C_4\omega_z}{4(1+C_2)}A_+^2 + \epsilon_+ - \epsilon = 0 \tag{3.14}$$

where the anharmonicity coefficients C_2, C_4 and C_6 are defined in Chapter 1. We know A_+ is the relevant solution because $C_6 < 0$ and C_4 is typically small. We observe that S^2

as a function of relative detuning $\eta = \epsilon/\omega_z$ can be fit to a parabola

$$a(S^2)^2 + bS^2 + c = \eta \tag{3.15}$$

where

$$a = \frac{15}{16(1+C_2)\alpha^4}\left(C_6^0 + D_6\frac{V_c}{V_o}\right) \tag{3.16}$$

$$b = \frac{3}{4(1+C_2)\alpha^2}\left(C_4^0 + D_4\frac{V_c}{V_o}\right) \tag{3.17}$$

$$c = \frac{\epsilon_+}{\omega_z}. \tag{3.18}$$

Eqs. 3.16 and 3.17 can be used to determine the calibration constant, α, in three ways that produce answers that are in good agreement; a fourth method has too large an error to be useful. Table 3.1 summarizes the results. Both a and b can be measured as a function of the compensation potential, V_c, and fit to a line

$$a = m_a\frac{V_c}{V_0} + b_a \tag{3.19}$$

$$b = m_b\frac{V_c}{V_o} + b_b. \tag{3.20}$$

Because $D_6 < C_6^0$, a does not change appreciably as V_c changes. However, the value of b does change, so α can be computed as

$$\alpha^2 = \frac{3C_4^0}{4b_b(1+C_2)} = \frac{3D_4}{4m_b(1+C_2)}. \tag{3.21}$$

C_4^0 and D_4 are computed to good accuracy since the trap dimensions, ρ_o and z_o, are known to a very high accuracy from a fit of measured m=0 TE mode frequencies (See Fig. 1.3). The mode frequencies are calculated over a grid of values of ρ_o and z_o and compared to the measured frequencies. The best fit is taken to be the dimensions (ρ_o, z_o) which produces the least total deviation from the measured frequencies (see Chapter 1). The uncertainty in the trap dimensions is calculated from the error in the linear fit of the calculated and

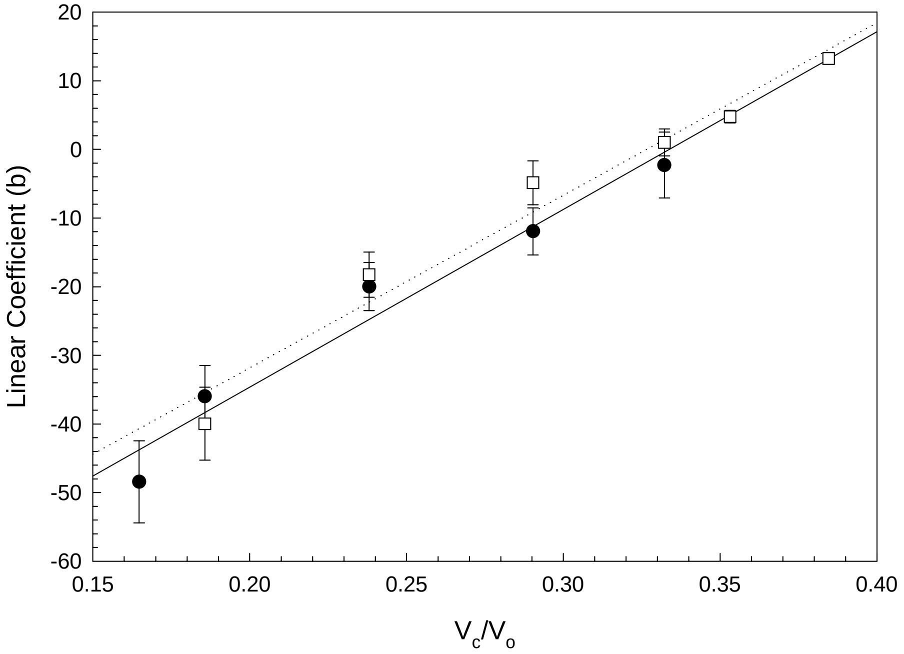

Figure 3.6: The linear coefficient (b) from the parabolic fits for various compensation voltage settings. The circles and squares represent two different drive strengths.

measured frequencies.

Alternatively, α, can be calculated for any particular V_c from

$$\alpha^2 = \frac{3}{4b(1+C_2)}\left(C_4^0 + D_4\frac{V_c}{V_o}\right) \tag{3.22}$$

with a much larger error than using Eq. 3.21, but a weighted mean of several such calculations improves the error somewhat.

A fourth method, first described in [12], calculates α using the slope of b and a as

$$\alpha = \sqrt{\frac{\frac{\Delta b}{\Delta V_c}}{\frac{\Delta a}{\Delta V_c}}\frac{5}{4}\frac{D_6}{D_4}} \tag{3.23}$$

However, for this trap C_6 is quite insensitive to changes in V_c, so $\Delta a/\Delta V_c$ is very small with a large relative error (95%). This gives an α whose error limits encompass the previously calculated values but whose absolute value is 10 times too small. For all measurements discussed in later chapters, we use $\alpha = 0.0126$ because of the small error in m_b and D_4.

Chapter 4

Observations of Large Clouds of Electrons

Within a cloud of electrons, each particle follows the equations of motion given in section 1.4. Because each particle experiences a slightly different force due to anharmonicity, the center-of-mass amplitude is typically small, dominated by the internal motions, even when driven parametrically. However, we observe that if the energy in the internal motions can be damped, synchronization is observed. This chapter explores synchronization due to damping to the 4.2 K microwave cavity.

4.1 Measurement of the Axial Excursion of Many Electrons

Measurements of the axial amplitude can be performed for the center-of-mass of more than one electron, using the calibration procedure outlined in the last chapter. Because the detection circuit measures the induced charge on one endcap by the trapped charges, the measured signal scales with the number of electrons. However, many particles need not act like a rigid oscillator because the internal motions may dominate, decreasing the center of mass amplitude. It is convenient to use the ratio A/A_{rigid}, where A is the actual center-of-mass amplitude, and A_{rigid} is the amplitude for N electrons rigidly attached together given by

$$\frac{15C_6\omega_z}{16(1+C_2)}A_{rigid}^4+\frac{3C_4\omega_z}{4(1+C_2)}A_{rigid}^2+\epsilon_\pm-\epsilon=0. \tag{4.1}$$

When $A/A_{rigid}=1$, the electron cloud oscillates like a rigid body. In general we would expect $A/A_{rigid}<1$. The measured signal, S, is related to A as

$$S=N\alpha\frac{A}{A_{rigid}}A_{rigid} \tag{4.2}$$

where α is the calibration obtained with one electron and N is the number of electrons in the trap.

As in the last chapter, a measurement of A is made by measuring parametric lineshapes for various anharmonicity settings, fitting the lineshapes to parabolas and relating the quadratic and linear coefficients of the fits to α as

$$a=\frac{15\left(C_6^0+D_6\frac{V_o}{V_o}\right)}{16(1+C_2)\left(N\alpha\frac{A}{A_{rigid}}\right)^4} \tag{4.3}$$

$$b=\frac{3\left(C_4^0+D_4\frac{V_c}{V_o}\right)}{4(1+C_2)\left(N\alpha\frac{A}{A_{rigid}}\right)^2}. \tag{4.4}$$

As before, the calibration, α, can be defined in terms of the slope or intercept of either Eq. 4.3 or Eq. 4.4, but we choose the slope of Eq. 4.4 to minimize the error. Therefore the calibration of the center-of-mass axial amplitude of an arbitrary number of electrons is

$$N\alpha\frac{A}{A_{rigid}}=\sqrt{\frac{3D_4}{4m_b(1+C_2)}}. \tag{4.5}$$

Fig. 4.1a shows the measured slopes for various size clouds up to 1000 electrons, and Fig. 4.1b shows the factor of rigidity for the same clouds. All measurements were made with the cyclotron frequency tuned near a cavity mode frequency, which, as we will see, is a crucial component in obtaining synchronization.

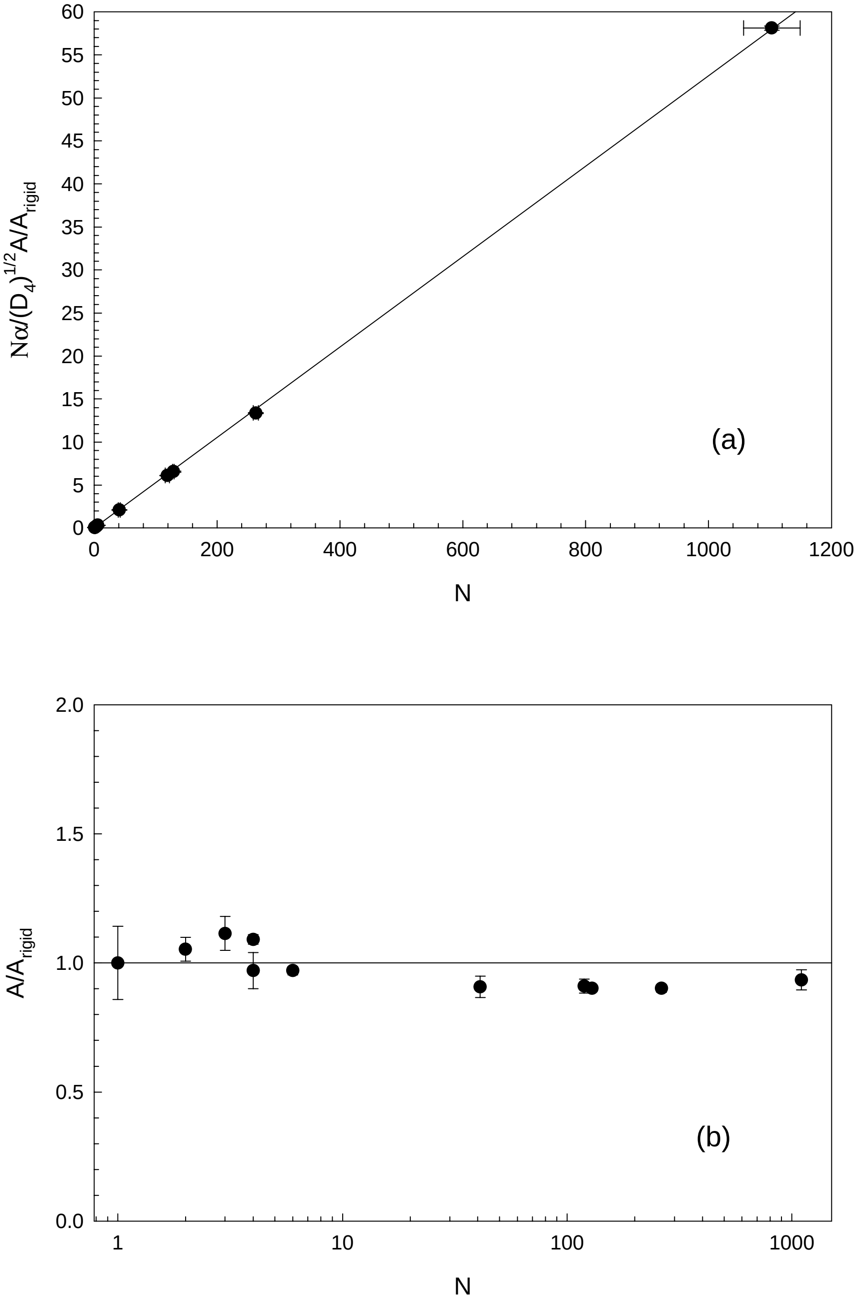

Figure 4.1: (a) Measured signal dependence on compensation voltage versus number of electrons. The line is the scaled calibration for 1 electron. (b)The ratio, A/A_{rigid} extracted from (a) versus number of electrons. $A/A_{rigid} \approx 1$, showing that with strong cavity cooling, the center-of-mass of each of these clouds oscillates with the same amplitude as a rigid ball of charge.

4.2 Axial Amplitude and Cyclotron Cavity Modes

As was described in Chapter 2, the detector is only sensitive to axial motion of the center-of-mass motion. However, the center-of-mass motion may be swamped by the internal motions due to anharmonicities, and the internal motions need to be cooled to observe a significant center-of-mass amplitude. One extremely effective way to do this is to cool the cyclotron energy to a TE or TM cavity mode. Near a mode the cyclotron motion is damped at a rate of

$$\gamma = \frac{\gamma_M}{1+\delta^2} \tag{4.6}$$

where γ_M is the damping on top of the mode and δ is the dimensionless detuning from the mode center frequency,

$$\delta = 2\frac{\omega_c - \omega_M}{\Gamma_M}. \tag{4.7}$$

Since the axial motion couples to the cyclotron motion through the Coulomb interaction, the axial motion can also be cooled by the cavity mode. If the square of the parametric amplitude, S^2 at $\omega_d = 2\omega_z$, is plotted as a function of ω_c (which is controlled by changing the magnetic field), the result is a series of well defined and well separated peaks that are well approximated by Lorentzians (see Fig 4.2). Therefore this "mode map" is really a representation of the cooling power of the modes of the cavity. It is important to stress that the parameter under control in this plot is the cyclotron frequency, and the observed parameter is the orthogonal axial motion whose frequency is 1000 times smaller than the cyclotron frequency, an indication that this is a highly nonlinear system.

The parametric amplitude may also be interpreted as the degree of synchronization of the electrons. If N electrons are fully synchronized, they oscillate like a rigid ball of charge Ne, and their center-of-mass amplitude is predicted by the rigid model described in Chapter 3. Under certain conditions the electrons near a cavity mode become fully synchronized and the cloud becomes rigid. When this rigid limit is reached, the parametric

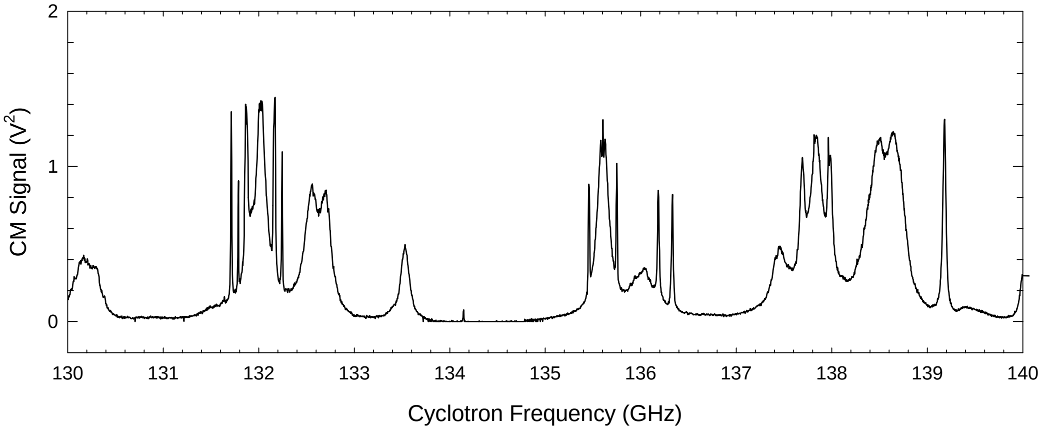

Figure 4.2: Axial signal versus cyclotron frequency. The amplitude increases as the cyclotron frequency comes into resonance with a cavity mode.

amplitude is maximized and any further increase in the cavity mode cooling power does not further increase the axial amplitude. In this configuration, the measured modes have flat tops (see Fig. 4.3b) rather than peaks as is seen in Fig. 4.3a. The unsaturated parts of the peaks can still be fit to Lorentzians. The measured amplitude of the saturated part is described by $A/A_{rigid} \approx 1$ as discussed in the previous section, indicating that the electrons are oscillating with same amplitude as a rigid charged ball. However, if noise is added to the system, such as from heat in the FET, the parametric amplitude shrinks from the rigid limit and the peaks appear Lorentzian as seen in Fig. 4.4.

If the amplitude of the measured cavity mode is probed more deeply, one finds that the parametric lineshape for large cavity detunings deviates significantly from that predicted by Eq. 3.14. Away from a cavity mode ($\delta \approx 1$), as the drive frequency is swept up, the amplitude jumps to the predicted value as the drive enters the region of excitation, but then collapses to a much smaller value. The amplitude remains small through the center

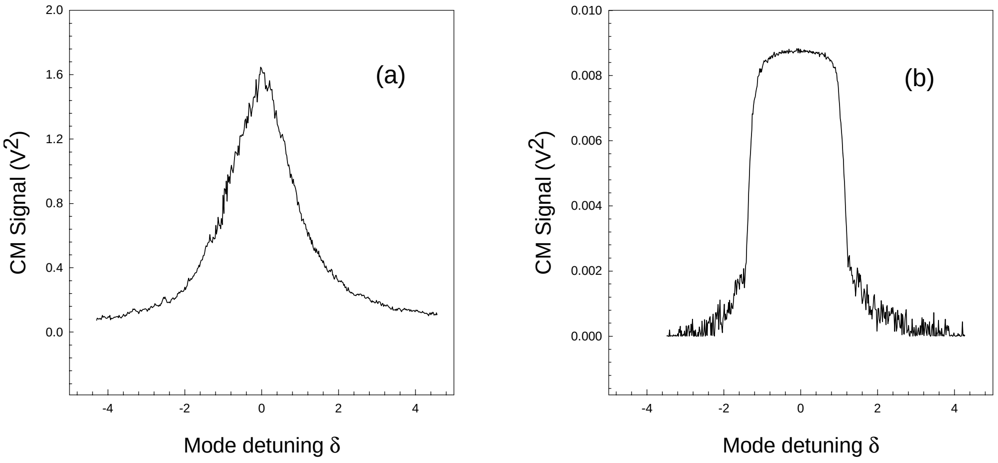

Figure 4.3: TE_{115} cavity mode when the electron cloud is (a) not fully synchronized and (b) fully synchronized near resonance. (a) and (b) were made with different size electron clouds so the signal size was also different.

of the resonance, but eventually climbs up to the predicted value and follows the parabola to the edge of the region of excitation. In fact, the initial spike is a transient effect; if the drive frequency is swept down, the amplitude remains low. This collapsed amplitude decreases with detuning, giving the cavity mode resonance it's Lorentzian wings. Fig. 4.5 shows the parametric lineshapes at various mode detunings.

When measuring the synchronization of the electrons near a mode, the nature of the unsaturated part of the lineshape seems to depend on several parameters such as drive strength and anharmonicity. One way to crudely parameterize the partial synchronization is to define a"flatness factor" of a mode, which is the ratio of the width of the saturated part to the width at half the maximum amplitude. When f =0, the lineshape is peaked (though need not be Lorentzian); when f=1, the lineshape is completely squared off. The flatness factor of observed lineshapes for large N never reaches 1 because of the characteristic knuckle on the trailing edge (see Fig. 4.6); this lineshape depends on which way the

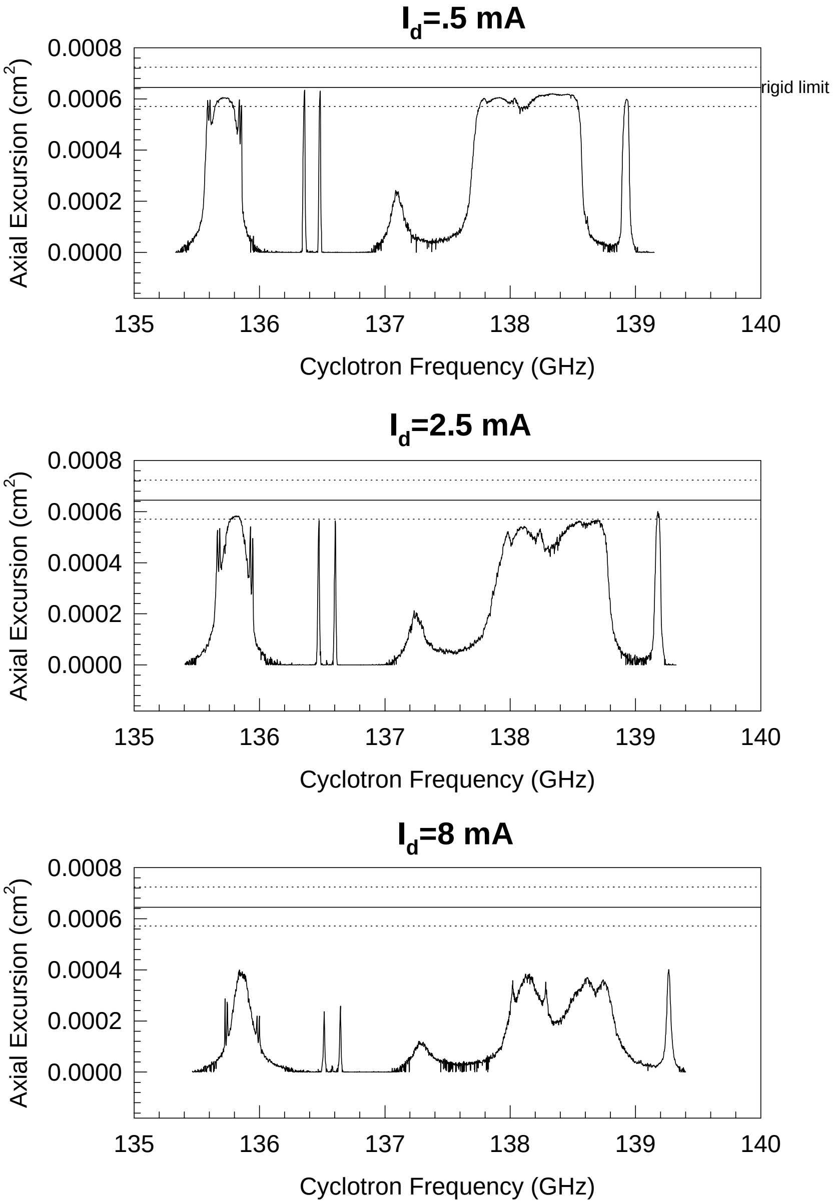

Figure 4.4: Mode maps at various FET drain currents when the FET is not submerged in liquid helium. As the heat dissipated in the FET increases, the noise environment of the electrons increases, and the level of synchronization decreases.

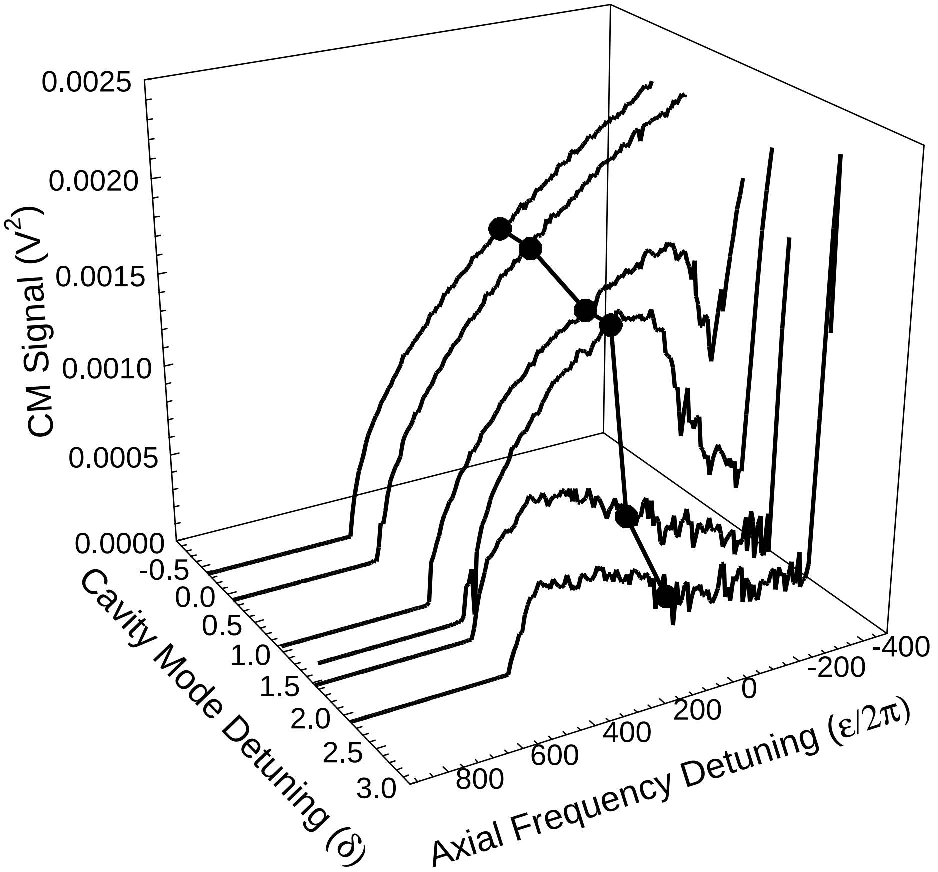

Figure 4.5: Parametric axial lineshapes for various detunings from the cyclotron cavity mode. The circles are the amplitudes that would be measured in a “mode map”.

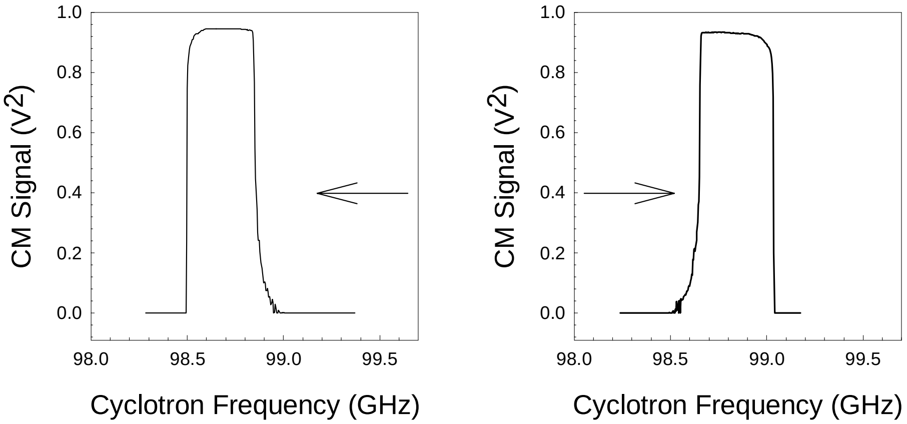

Figure 4.6: The shape of the TE_{115} becomes highly asymmetric for large N and depends on the direction the field is swept. (a) The field is swept down. (b) The field is swept up.

magnetic field is swept. Fig. 4.7 shows how the flatness of a mode changes with C_4, N, axial damping and drive strength. Since all of these parameters affect the rigid axial excursion, A_{rigid}, one might postulate that these mode lineshapes are distortions of how much larger A_{rigid}, predicted by the rigid model, is compared to the small unsynchronized axial excursion of the center-of-mass which is unchanged for various parameters. For example, as h increases, A_{rigid} increases so the lineshape appears more squared off as amplitude the rises steeply to a larger A_{rigid} (see Fig. 4.8). This may also explain the data for increasing N and γ_z. However, this does not explain the flatness dependence on anharmonicity, for when C_4 is large and positive, the mode lineshape is very square, but A_{rigid} is not as large as it is for other values of C_4. The asymmetric lineshapes observed for large N and large and positive C_4 are also not understood. Since both of these parameters affect the coupling of axial motion to the cavity mode (through the nonlinear terms in the equation of motion), the lineshape may depend on how fast the electrons synchronize in the rigid limit.

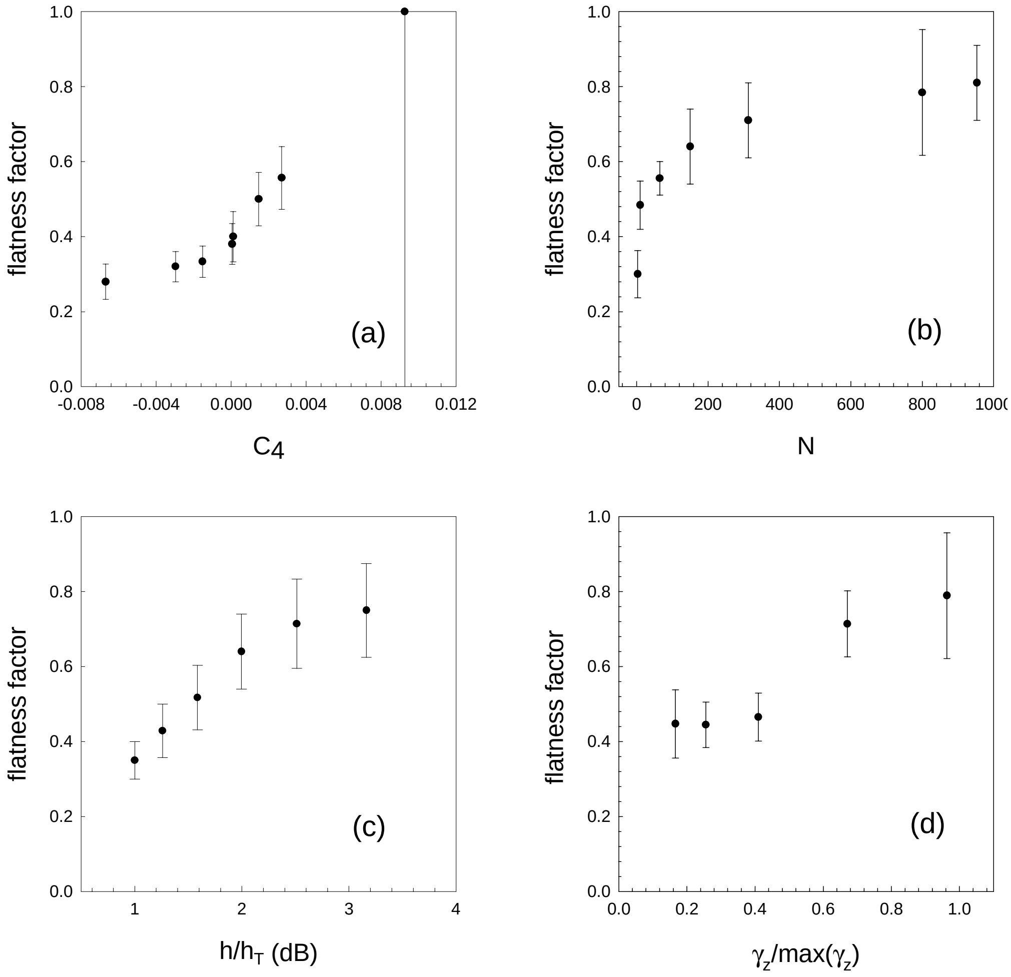

Figure 4.7: Flatness factor (flat top width/FWHM) versus (a) C_4, (b) number of electrons, (c) drive strength, and (d) axial damping.

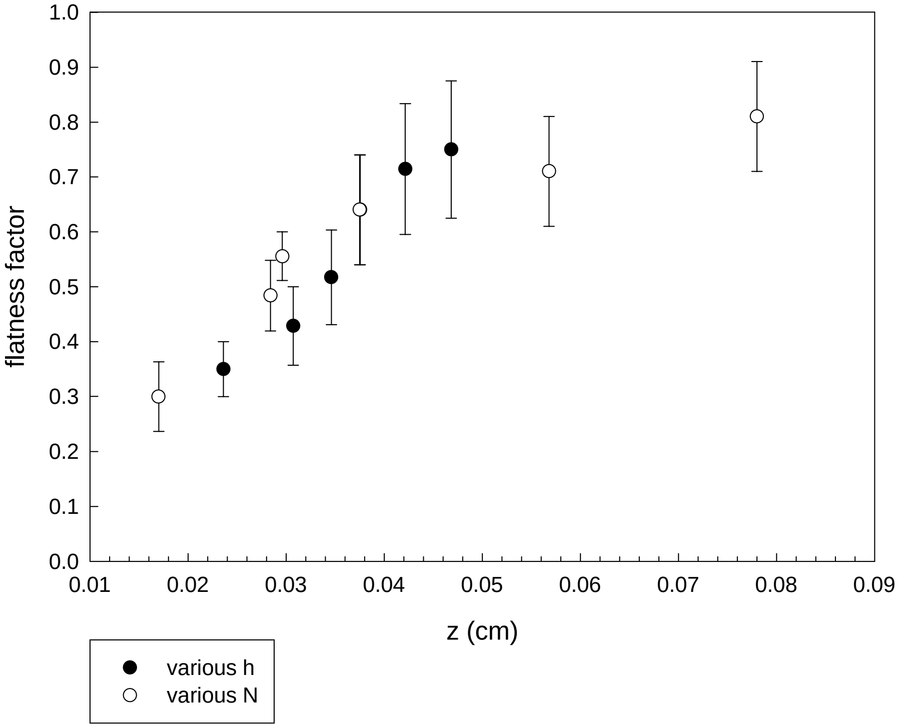

Figure 4.8: Flatness factors for various drive strength and number of electrons (figures 4.7b and 4.7c) plotted against axial excursion, $z \propto A_{rigid}$, near a cavity mode.

Chapter 5

Stochastic Behavior of One Electron

5.1 Phase Bistability of the Parametric Excitation

As was stated in Chapter 3, the phase of the parametric excitation of the axial motion for a single electron is given as

$$\sin(2\Psi) = \frac{h}{h_T}. \tag{5.1}$$

Since the drive frequency is twice the response frequency, there is an phase ambiguity of the response compared to the drive. Therefore, Ψ is only determined up to a value of π and there is a random choice of two phases in the excited state, Ψ or $\Psi + \pi$. Fig. 5.1 shows the phase space plot of this system.

In the noise-free description of Chapter 3, both phases are completely stable. However, random jumps in this phase have been observed for a single electron. Noise drives fluctuations in phase space that occasionally traverse the unstable point at the origin and land in the opposite basin of attraction, thereby switching phase. We observe that the level of noise relative to the amplitude of the excitation primarily determines the rate of these flips.

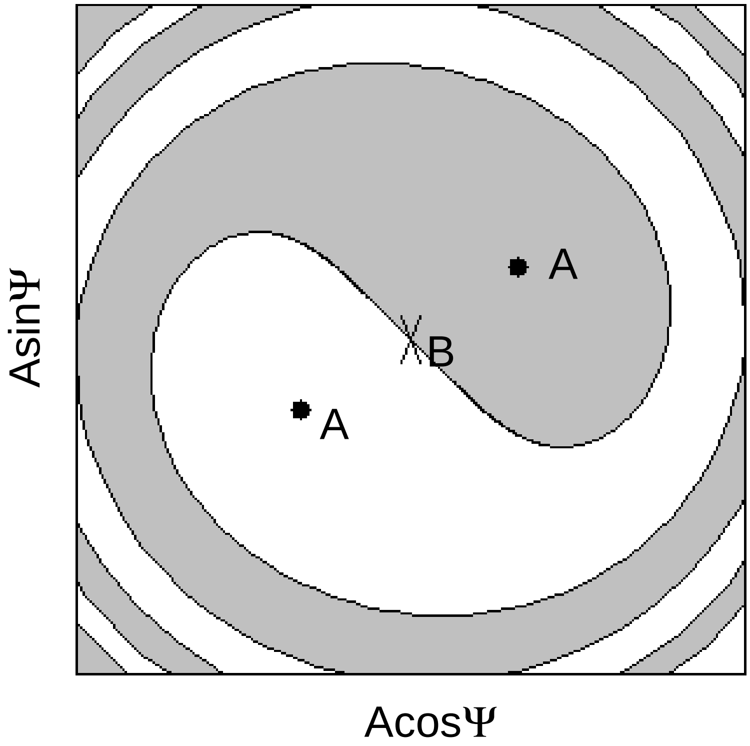

Figure 5.1: Phase space of parametrically excited oscillator. The dots (A) mark the stable points and the cross (B) marks the unstable point at the origin. The lines trace the separatrix of the two basin's of attraction.

5.2 A Model of Phase Flip Transition Rates

In this section we derive the rate at which the phase response flips by 180 degrees, using the model procedure described by the Dykman group [13]. We add a noise term, $\xi(t)$, to Eq. 3.1

$$\ddot{Z} + \gamma_Z \dot{Z} + \omega_Z^2 Z + \lambda_4 \omega_Z^2 Z^3 + \lambda_6 \omega_Z^2 Z^5 + h\omega_Z^2 \cos(\omega_d t) Z = \xi(t) \tag{5.2}$$

We assume that the noise in the system, $\xi(t)$, is white near the axial frequency. The noise intensity of the thermal noise is $D = 3|\lambda_4|kT/8md^2\omega_z\gamma_z$ where m is the electron mass and d is the trap size constant.

The details of the derivation of the flip rate in the limit of a strong drive compared to threshold are contained in Appendix A. Only the results will be discussed here. The general form of the flip rate (W) is

$$W \propto exp\left(-\frac{2h}{h_T}\left[\frac{[1-4\rho(1-\frac{\epsilon}{\epsilon_+})]^{3/2}+6\rho(1-\frac{\epsilon}{\epsilon_+})-1}{24\rho^2 D}\right]\right) \tag{5.3}$$

where $\rho = 5\lambda_6 h/9\lambda_4^2$ and $\lambda_4, \lambda_6 < 0$. See Fig. 5.2 for a definition of ϵ and ϵ_+. The expression for the flip rate is particularly simple when one of the anharmonic terms dominates the equation of motion. If the trap is tuned to make $|C_4| < 10^{-5}$, then $|C_4| \ll |C_6|A^2$, and the flip rate can be approximated as

$$W \propto exp\left(-\frac{16md^2\omega_z^{3/2}}{3\sqrt{5}k|\lambda_6|^{1/2}}\frac{(\epsilon_+-\epsilon)^{3/2}}{T\epsilon_+}\right) \tag{5.4}$$

If the trap is severely detuned so $|C_4| \gg |C_6|A^2$, $-\rho(1-\epsilon/\epsilon_+)$ is very small then Eq. 5.3 becomes

$$W \propto exp\left(-\frac{3\omega_z}{8|\lambda_4|k}\frac{(\epsilon_+-\epsilon)^2}{T\epsilon_+}\right) \tag{5.5}$$

These expressions are valid under several conditions. First is that a small displacement from one of the stable points in phase space is extremely underdamped as equilibrium is restored. The details of the damping condition are discussed in Appendix A. This damping condition requires that $\epsilon_+ - \epsilon$ be not too close to zero, which also ensures that the detuning is larger than the axial damping width. However, Eq. 5.3 breaks down for $(\epsilon_+ - \epsilon)/\epsilon_+$ greater than approximately 0.3, but Maloney, et. al. [13] have numerically calculated the flip rate over the entire range of the excitation. A fit of the numerical values gives an approximate flip rate of

$$W \propto \exp\left[\frac{0.85md^2\omega_z^{3/2}}{k|\lambda_6|^{1/2}}\frac{(\epsilon_+-\epsilon)^{0.89}}{\epsilon_+^{0.39}T}\right]. \tag{5.6}$$

When these numerical values are used, they will be noted in later sections. Finally, this theory assumes that the probability of switching phase is exponentially small, so it is not

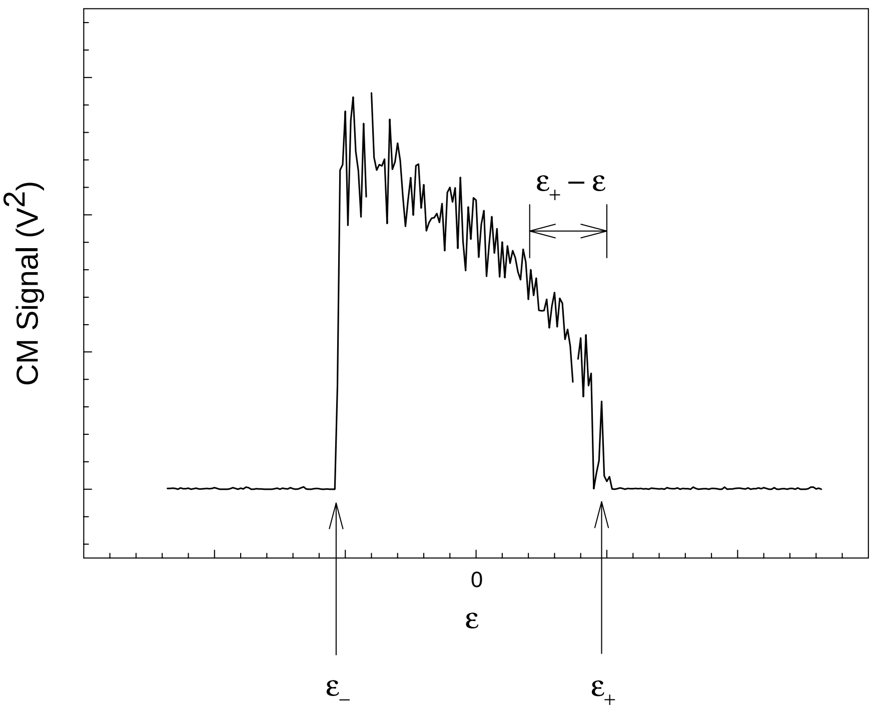

Figure 5.2: Parametric resonance of a single electron with the edges, $\epsilon_{\pm}$, marked.

valid for values of the exponential argument in Eq. 5.3 that are near zero.

Eqs. 5.4 and 5.5 imply that the flip rate depends on drive strength, detuning from the edge of the parametric resonance, and the effective temperature of the system. Since the detuning determines the axial amplitude, and the effective temperature determines the noise level, Eqs. 5.4 and 5.5 relate the flip rate to the amplitude of the oscillation and the level of residual noise. Thus if the temperature increases, such as by applying external noise, the flip rate increases; if the amplitude increases, such as by increasing the detuning, the flip rate decreases.

5.3 Data Acquisition

5.3.1 Statistical Errors

If the flips occur randomly, the events obey Poisson statistics, so the flip rate (W) may be given as

$$W = \frac{n-1}{\sum_i \tau_i} \pm \frac{\sqrt{n-1}}{\sum_i \tau_i} \tag{5.7}$$

where n is the number of flips recorded and τ_i is the elapsed time between flips. This definition is preferable to the somewhat simpler form

$$W = \frac{n}{T} \pm \frac{\sqrt{n}}{T} \tag{5.8}$$

where n is the number of flips in a period T. This is because we wish to examine the distribution of time between flips. It has been observed [7] that if a histogram of time between flips is not the exponential distribution as would be expected for a random system. Rather, there appeared to be more flips than expected for the shortest times. This phenomenon is also investigated in this experiment (discussed further in a section 5.4.4). The number of flips in Eq. 5.7 is smaller by 1 than Eq. 5.8 because within the period T the time before the first flip and the time after the last flip is ignored; the first flip and last flip serve as markers to begin counting time between flips.

Since the statistical error in the flip rate depends on the square root of the number of flips, a minimum number of flips must be accumulated to have a certain confidence in the flip rate. For most of the data collected, the minimum number of flips was 150, giving a fractional error in the flip rate of 8.2%. If the minimum number of flips is not exceeded after a single bin of time T, data in additional bins are acquired and the data are combined into a single set and averaged using Eq. 5.7. The acquisition bin widths are kept the same for a single flip rate measurement.

Data acquired in the manner described above, even for purely Poissonian statistics can lead to bias in calculating the flip rate if the number of flips per bin is small enough that the time discarded before the first flip and after the last flip is a significant fraction of the total bin. In other words, if a histogram of the number of flips per bin (x) for many bins were plotted, the distribution should follow a Poisson function centered around the mean number of flips (μ) [40],

$$P(x;\mu) = \frac{\mu^x}{x!} e^{-\mu}. \tag{5.9}$$

However, because the time at the beginning and end of the bin is discarded, there would be no measurements with 0 or 1 flip in a bin. This leads to a bias in the mean flip rate unless the mean number of flips per bin is much bigger than 1. The fractional bias error is given by the probability of a bin with 1 or 0 flips.

$$\sigma_b = P(0,1;\mu) = [1+\mu]e^{-\mu}. \tag{5.10}$$

If $\mu = 7$, $\sigma_b = 0.73\%$. Therefore, if the average number of flips per bin is near 7, the bias error is approximately 10 times smaller than the statistical error of 8.2% This requirement is ensured by crudely estimating the flip rate from preliminary measurements. Measurements of a wide range of flip rates typically needed 3 or 4 bins to acquire 150 flips.

5.3.2 Systematic Errors

Because the flip rate should depend on the drive strength (ϵ_+) and detuning ($\epsilon_+ - \epsilon$) (see Fig. 5.2), determining the edges of the resonance precisely is important. For C_4 small, ϵ_+ is at the extremum of the parabola (see Fig. 5.2) where $A \approx 0$ so its position can be easily masked by noise. The excited and unexcited amplitudes are both stable for frequencies below ϵ_- so hysteresis can bias the measurement of $\epsilon_+ - \epsilon_-$. Furthermore, the entire resonance can drift slowly over time due to drifts in the trapping potential; the drift rate is typically between 1 and 3 Hz per hour.

A method to determine the edge of the parametric resonance, ϵ_+, which is quite insensitive to noise is employed to determine the drive frequency, $2(\epsilon + \omega_z)$ and hence $\epsilon_+ - \epsilon$. The resonance is swept repeatedly, the amplitudes averaged and the smoothed data fit to a parabola, $\omega_d/2 = aS^4 + bS^2 + c$ where ω_d is the drive frequency, S is the measured signal proportional to the electron amplitude, A, and $c = \epsilon_+ + \omega_z$. This procedure is fairly quick (about 3 minutes) and is performed between each time bin. If many flip rate measurements are made with the same drive strength over several hours, the drift and scatter of the measurement of c can be determined. We assume that the drift is entirely due to the change in ω_z from changes in the trapping potential and the scatter is due to inaccuracies in determining ϵ_+. Therefore, the actual detuning from the edge, $\epsilon_+ - \epsilon$ can be determine according to how much c changed over the measurement time (T_{tot}), with an error of

$$\sigma_{\epsilon_+ - \epsilon} = \sqrt{\left(\frac{\Delta c}{\Delta t} T_{tot}\right)^2 + \sigma_c^2} \tag{5.11}$$

where σ_c is the scatter in the measurement of c without the drift.

The parabolic fit does not also determine ϵ_-. Instead, the width of the resonance, $\epsilon_+ - \epsilon_-$, is determined from a sweep of the region around the parametric resonance; the sweep always increases in frequency to minimize hysteresis. The data is then sorted from the lowest frequency to look for the first point in which the amplitude is above a threshold which gives ϵ_-. A similar procedure is performed from the highest frequency to determine ϵ_+. This measurement is repeated several times to average out the scatter due to noise.

5.4 Measured Flip Rates

5.4.1 Detuning and drive strength

The phase flip rate measured for various parameters are shown in Figs 5.3, 5.4 and 5.5. Fig. 5.3 shows the dependence of flip rate on the detuning of the drive frequency from the upper edge of parametric resonance, ϵ_+. The anharmonicity parameter, λ_4, is less than 2×10^{-5}; therefore the system is dominated by λ_6 and $lnW \propto (\epsilon_+ - \epsilon)^{3/2}$, as explained in section 5.2. However, because the range of $(\epsilon_+ - \epsilon)/\epsilon_+$ is outside the range prescribed by Eq. 5.4, the form of the expected flip rate dependence is given approximately by Eq. 5.6. The measured dependence is clearly exponential, though it is difficult to distinguish

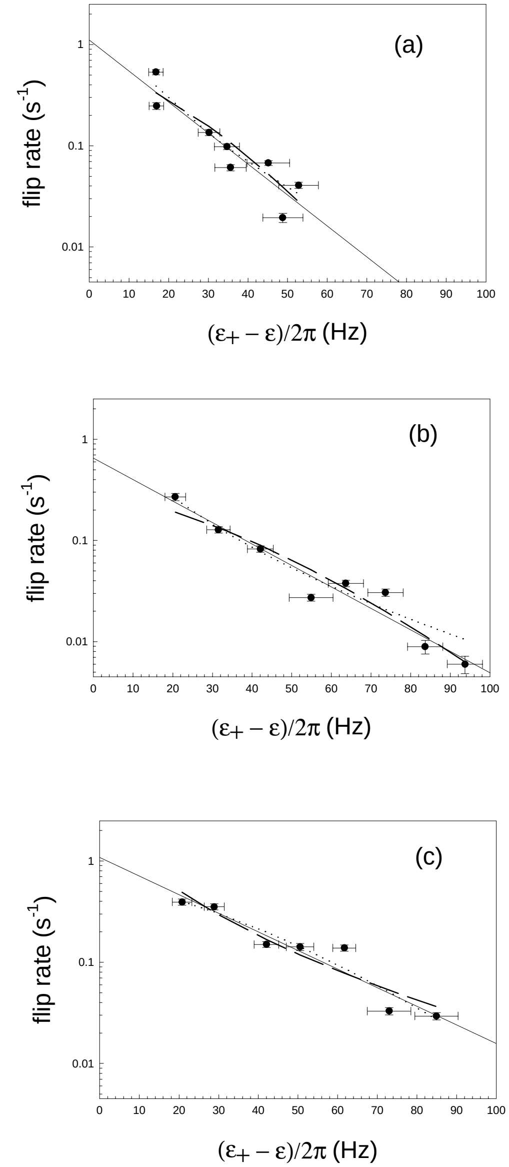

Figure 5.3: Flip rate versus detuning of drive frequency from upper edge of parametric resonance for various drive strengths. (a)$\epsilon_+/2\pi = 31$ Hz (b)$\epsilon_+/2\pi = 60$ Hz (c)$\epsilon_+/2\pi = 100$ Hz. The lines are fits to $lnW = a + b(\epsilon_+ - \epsilon)^c$ where c=1 (solid), c=1/2 (dotted) and c=3/2 (dashed). The data clearly is insensitive to the power of the fit.

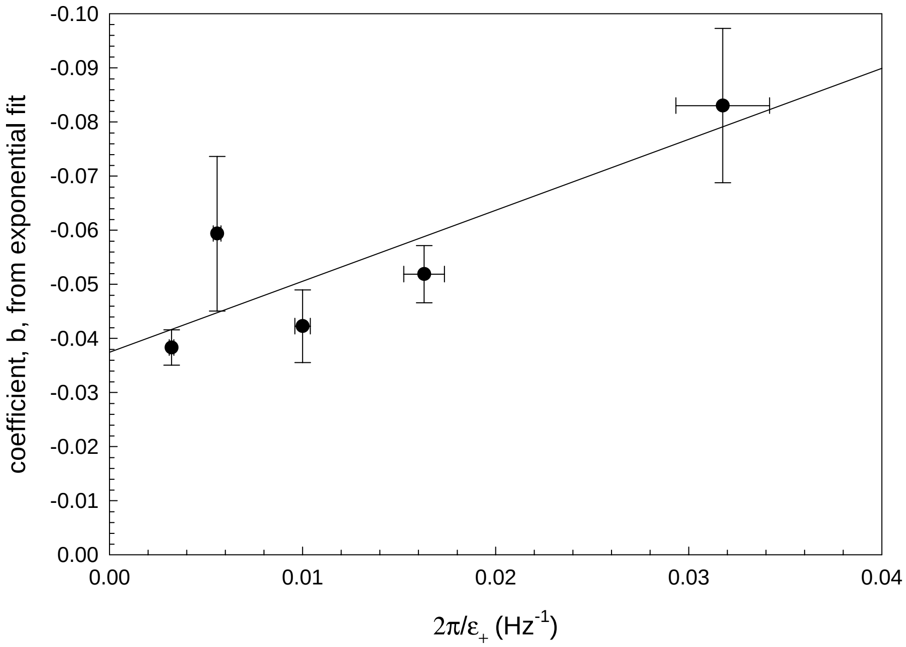

Figure 5.4: Linear coefficient of fit of $y = a\, exp(-b(\epsilon_+ - \epsilon))$ versus $1/\epsilon_+ \approx 4/h\omega_z$. A fit of $y = a\, exp(-b(\epsilon_+ - \epsilon)^{3/2})$ produces a similar line.

the appropriate exponent of $\epsilon_+ - \epsilon$. Each plot in Fig. 5.3 is for a different drive strength or ϵ_+; the slope decreases with increasing drive strength, as predicted by Eq. 5.4. The explicit dependence of this slope on ϵ_+ is shown in Fig. 5.4.

5.4.2 Externally Applied Noise

White noise is added to the system externally to simulate an increase in the thermal noise, D, which was present naturally in our apparatus. The noise is generated from a 100 kHz bandwidth noise source provided as part of an HP 3561a spectrum analyzer. The signal is then amplified, filtered down to 1 kHz, mixed to ν_z - 5 MHz, combined with the parametric drive and applied to one endcap (see Fig. 2.8). A 5 MHz drive is also applied to the ring electrode. The measured noise bandwidth at ν_z - 5 MHz is 2 kHz which is

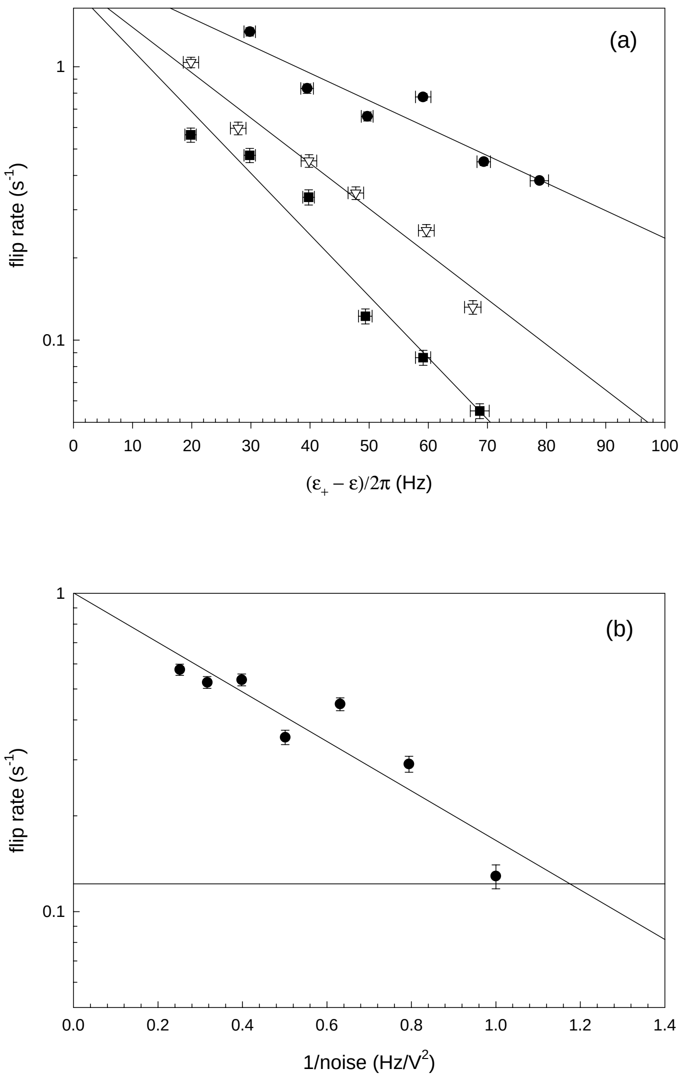

Figure 5.5: (a) Flip rates versus detuning from edge of parametric resonance for a single drive strength ($\epsilon_+/2\pi = 100$ Hz) and various noise power attenuations: -18 dB, circles; -21 dB, triangles; -30 dB, squares. The -30 dB line is not significantly different from data that had no noise present. (b) Flip rates versus the inverse noise relative to -30 dB for a detuning of 50 Hz. The horizontal line is the flip rate with no applied noise.

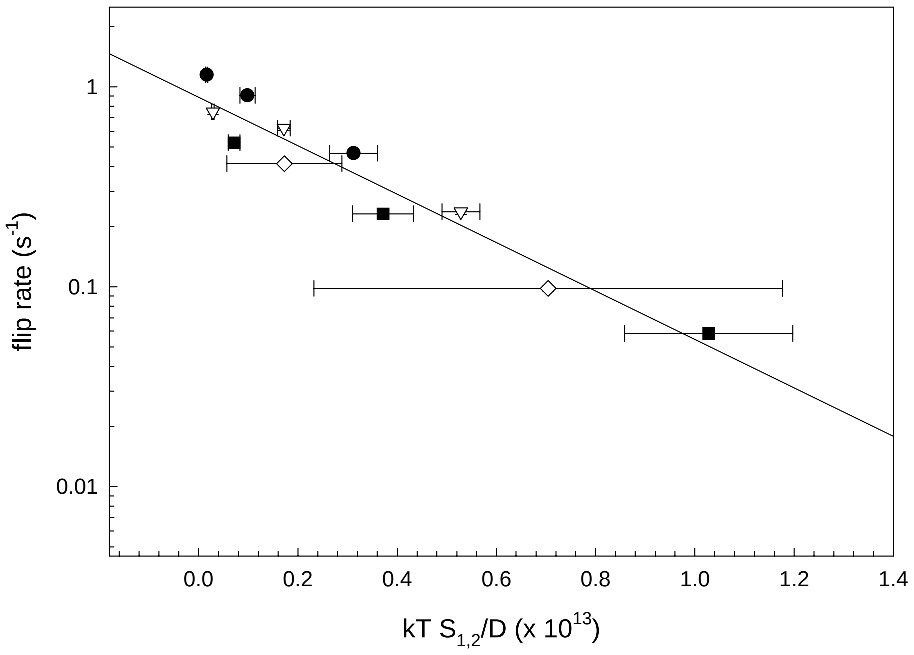

Figure 5.6: Flip rates of various detunings, drives and anharmonicities, shown together on the combined curve given by 5.3. The independent variable $kTS_{1,2}/D \propto \ln W$ is defined in Appendix A. The plotting symbols designate different detunings: 20Hz, circles; 50 Hz, triangles; 90 Hz, squares.

much larger than either the damping width (15 Hz) or the parametric width (200 Hz), thus effectively simulating white noise. The results are unchanged for a total bandwidth of 4 kHz. Fig. 5.5a shows that the slope of $\ln W$ versus $\epsilon_+ - \epsilon$ decreases for increasing noise, and Fig. 5.5b shows that the flip rate increases exponentially for increased noise with all other parameters held constant. There is a range of approximately 12 dB in noise power in which the noise changes the flip rate without wiping out the excitation. Systematic tests have shown noise applied at ν_z - 4 MHz with a ring drive at 5 MHz or at ν_z - 5 MHz with no drive on the ring have no effect on the flip rates.

5.4.3 Anharmonicity

Flip rates were measured for various values of λ_4. For the four compensation voltage settings shown in Fig. 5.6, the value of $\rho = 5\lambda_6 h/9\lambda_4^2$ varied between 0.01 and 750. Therefore, neither limiting case in anharmonicity for the flip rate given in Eq. 5.3 can be used so there is no simple dependence on λ_4. Instead, Fig. 5.6 shows the data on a combined curve with the x axis of lnW given by Eq. 5.3.

5.4.4 Distribution of Phase Residence Times

If phase flips are the manifestation of stochastic switching between two stable states, the distribution of times in each phase (the time between flips) would be exponential. Fig. 5.7 shows that for a wide variety of parameters, the distribution is indeed exponential. Earlier work [7] showed that for many electrons the distribution of flips was not quite exponential because there were extra flips at short times. The distribution of flips for more than one electron will be examined in the next chapter.

5.4.5 Correlation of Phase Flips and Amplitude Collapse

Examination of a section of raw data used for counting phase flips shows that for every phase flip there is a corresponding collapse in amplitude (see Fig. 5.8). The theory by Maloney et. al. suggests that the path in phase space from one stable point to the other must pass through the unstable point at zero amplitude. However, approximately 9% of the time there is an amplitude collapse that is not correlated with a phase flip. These may be cases of fluctuations that bring the amplitude close to zero but stop before traversing the unstable point and so fall back into the same basin without switching phase. It is not known why these events should occur 9% of the time.

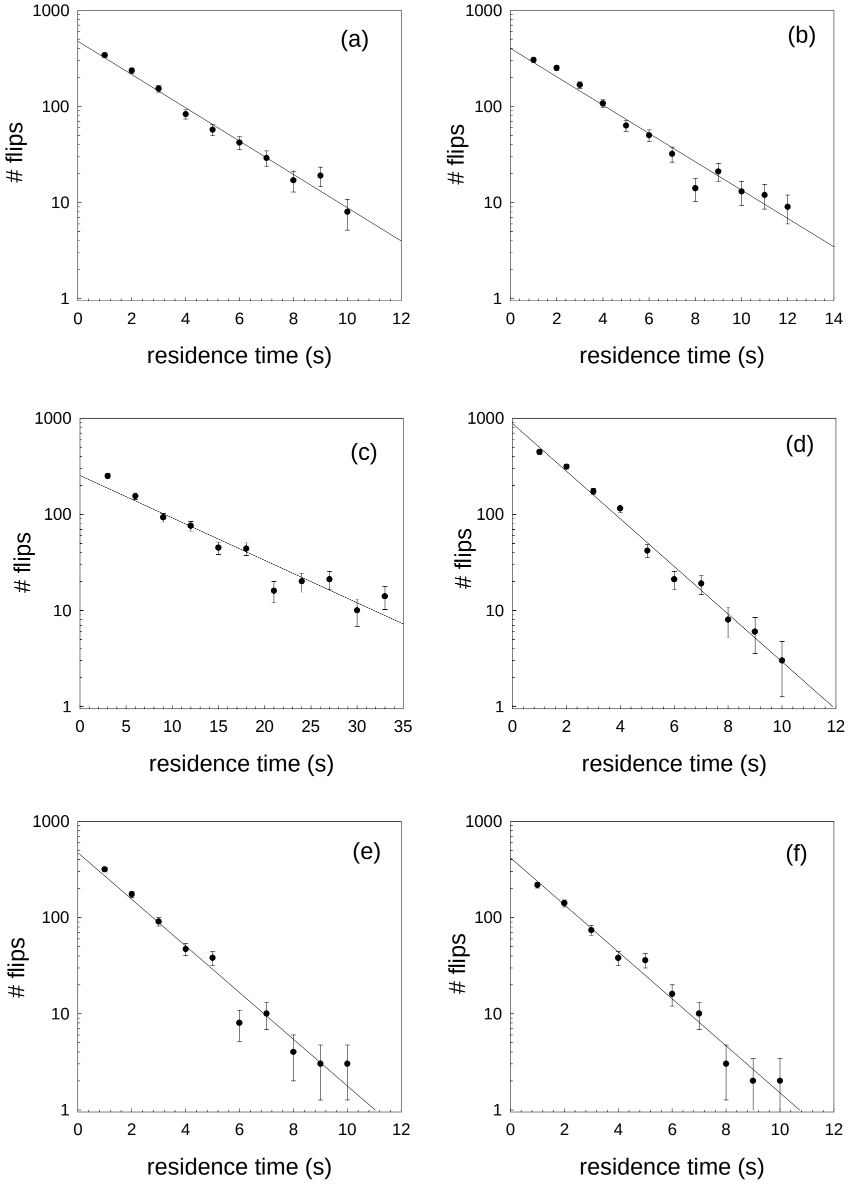

Figure 5.7: Histograms of time between flips for various parameter settings: (a) $\epsilon_+/2\pi =$ 100 Hz, $(\epsilon_+ - \epsilon)/2\pi = 20$ Hz; (b) $\epsilon_+/2\pi = 100$ Hz, $(\epsilon_+ - \epsilon)/2\pi = 50$ Hz; (c) $\epsilon_+/2\pi = 100$ Hz, $(\epsilon_+ - \epsilon)/2\pi = 90$ Hz; (d) $\epsilon_+/2\pi = 179$ Hz, $(\epsilon_+ - \epsilon)/2\pi = 20$ Hz;(e) $\epsilon_+/2\pi = 100$ Hz, $(\epsilon_+ - \epsilon)/2\pi = 100$ Hz with added noise; (f) $\epsilon_+/2\pi = 100$ Hz, $(\epsilon_+ - \epsilon)/2\pi = 50$ Hz, $C_4 = -1.72 \times 10^{-3}$ These plots show that an exponential distribution of time between flips is measured for a wide variety of parameters.

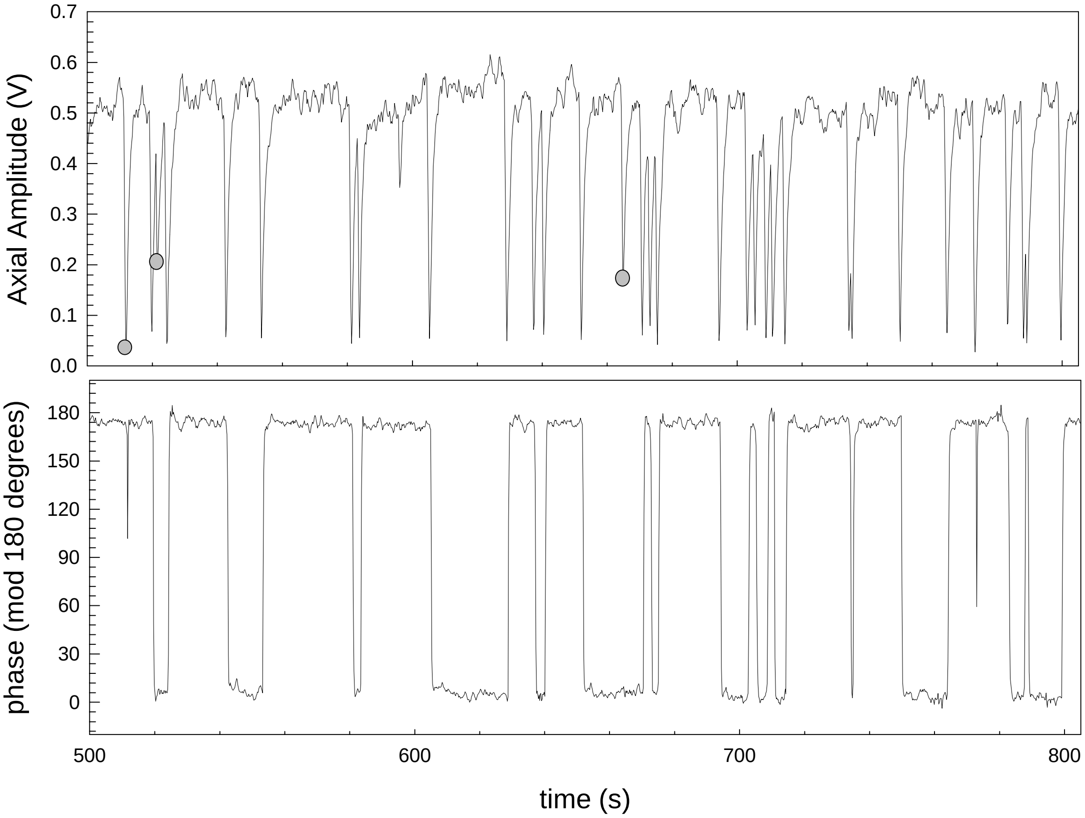

Figure 5.8: Sample of typical raw data of phase and amplitude over time. For every amplitude collapse, there is a corresponding phase flip except in three cases marked by grey circles.

Source	Type	Freq.	typ. V_{ω_z} $(V/\sqrt{\text{Hz}})$
1 MΩ on Ring	300 K Thermal ($<$ 25 mHz)	DC	3.1×10^{-10}
1 MΩ on Endcap	4.2 K Thermal	DC	2.3×10^{-9}
Fluke 732A on Ring	$1/f$ ($<$ 0.1 Hz)	DC	1.7×10^{-8}
PTS 250 and SRS 345 synth.	noise floor near $2\nu_z$	$2\omega_z$	7.1×10^{-10}
160 kΩ of inductive amplifier	$\approx$ 4 K Thermal	ω_z	1.0×10^{-8}

Table 5.1: Possible sources and types of noise, the frequency range and typical sizes at ω_z assuming $A = 0.05$. Narrow band noise was averaged over a bandwidth of $\epsilon_+/2\pi = 100$ Hz. See Fig. 2.8 for location of noise application.

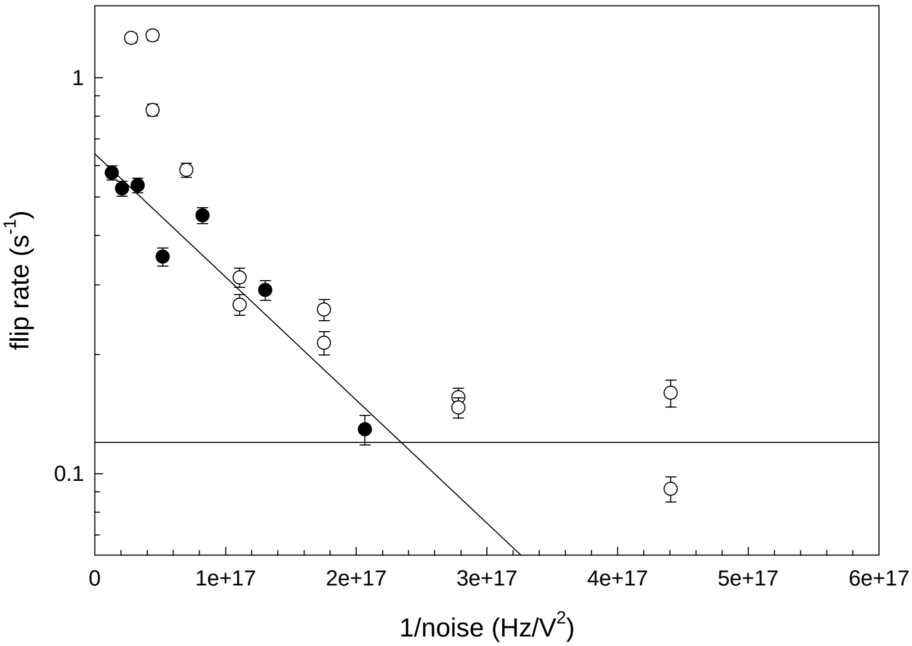

Figure 5.9: Flip rate versus noise power for externally applied white noise near ω_z (black) and $2\omega_z$ (white). The line is a fit for the black points only. The x axis was determined for each plot from independent calibrations of the drive strength.

5.5 Sources of Noise

The effective temperature of the system is a combination of all the sources of noise present. The theory by Maloney, et. al. [13] assumes that the noise is thermal white noise, but in the real experiment other forms contribute as well. Table 5.1 shows all likely sources of noise and their sizes. Noise only couples to the axial motion of the electron near the axial frequency, ω_z, but sources with frequencies near DC and $2\omega_z$ can mix with the axial oscillation to give noise near ω_z with strength

$$V_{\omega_z} \approx A\frac{2z_0}{d}\frac{1+C_2}{\kappa}V_{DC} \tag{5.12}$$

$$V_{\omega_z} \approx A\frac{z_0}{d}\frac{1+C_2}{\kappa}V_{2\omega_z} \tag{5.13}$$

where A is the axial amplitude, $C_2 \approx 0.1$ and $\kappa \approx 0.79$ are geometric constants and z_0 and d are the trap dimensions. Fig. 5.9 shows how the noise applied near $2\omega_z$ can be scaled to the noise near ω_z. Table 5.1 shows that only two sources of noise are significant, the Johnson noise at ω_z of the inductive amplifier, and the DC noise from the heavily filtered Fluke 732A power supply which provides the trapping potential. The next sections will discuss how the strengths of these sources are estimated.

5.5.1 Noise from the Inductive Amplifier

The rms voltage due to Johnson noise from a resistor, R, at temperature, T is given by [18]

$$V_{\omega_z} = \sqrt{4kTR}\left(\frac{\mathrm{V}}{\sqrt{\mathrm{Hz}}}\right) \tag{5.14}$$

where k is Boltzman's constant. The effective resistance of the inductive amplifier can be determined from the axial frequency and damping rate of the electron as [18]

$$R = \frac{m\gamma_z(2z_0)^2}{(e\kappa)^2} = 296 \pm 30 \text{ k}\Omega. \tag{5.15}$$

The noise from the amplifier is measured on a HP 8560 spectrum analyzer and can be related to the actual noise on the endcap with the relation [18]

$$V_{\omega_z} = \frac{\sqrt{2}mdz_0\gamma_z\omega_z}{e\kappa}\frac{S}{\alpha C} = (1.0 \pm .3) \times 10^{-8}\left(\frac{\mathrm{V}}{\sqrt{\mathrm{Hz}}}\right) \tag{5.16}$$

where α is the calibration constant given in Eq. 3.13 that relates the measured signal, S, at 90 kHz to the axial amplitude and C relates the signal measured at 61 MHz to S. The measured noise voltage implies the effective resistor has a temperature $T = 6.1 \pm 4$ K.

5.5.2 Noise from the Power Supply

The trapping voltage, V_0, is provided by a Fluke 732A solid state power supply which produces low frequency noise whose power density increases as $1/f$. The manufacturer specifications claim 1.1 μV of noise in the frequencies between 0.1 Hz and 10 Hz. However, an RC filter (R=1 MΩ, C=10 μF) on the ring removes all noise for frequencies above 0.1 Hz so this specification must be extrapolated to lower frequencies, specifically to $\nu_{min} = 1/2T$ where T is the bin time of a flip rate measurement. T varies from 500 to 5000 seconds and is set by an estimate of the flip rate. A characteristic of pink noise is that there is an equal amount of power in each decade of f so the total noise varies between 1.0 μV and 1.2 μV. Eq. 5.12 gives the noise at ω_z as typically

$$V_{\omega_z} = \tfrac{I}{\sqrt{\Delta\nu}} A \tag{5.17}$$

$$I^2 = \left(\tfrac{2z_0}{d}\tfrac{1+C_2}{\kappa}\right)^2 \int V_{DC}^2(\nu)d\nu = 1.2 \times 10^{-11}\ \mathrm{V}^2. \tag{5.18}$$

Because the DC noise is contained in a narrow frequency band, V_{ω_z}, the power density is an average of the total power over the bandwidth, $\Delta\nu$, for which the electron is sensitive to the noise. More theoretical work is needed to determine $\Delta\nu$, but it is probably related to ϵ_+ or $\epsilon_+ - \epsilon$. To test the significance of the noise from this power supply, a flip rate was measured with the power supply disconnected. The trapping voltage was maintained by the 10 μF capacitor on the ring line as well as a small voltage applied to the variable voltage line to counteract the small drift due to a leakage resistance that slowly discharged the capacitor. For the parameters $(\epsilon_+ - \epsilon)/2\pi = 50$ Hz and $\epsilon_+/2\pi = 100$ Hz, the flip rate decreased by approximately a factor of 5 with the removal of the power supply, indicating this source of noise is quite significant.

5.6 Measurement of Flip Rates from Sources of Noise

Eq. 5.4 assumes all the noise is thermal, but since a significant source of noise comes from the power supply, an extra term must be added and the flip rate becomes

$$W = C_1 exp\left(\frac{0.86md^2\omega_z^{3/2}}{k|\lambda_6|^{1/2}}\frac{(\epsilon_+ - \epsilon)^{0.89}}{\epsilon_+^{0.39}}\left[\frac{1}{T + (1/4kR)(I^2/\Delta\nu)A^2}\right]\right) \tag{5.19}$$

where $1/4kR = (6.07 \pm 0.61) \times 10^{16}$ (K Hz/V^2) scales the total DC noise (I) to a temperature, and C_1 is a constant about which little is theoretically known. The extra term in the denominator has several interesting implications for the results in section 5.4. First, since there is a term that depends on $A^2 \propto \sqrt{\epsilon_+ - \epsilon}$, there is no longer a simple dependence of flip rate on detuning which may explain why the data was so insensitive to the exponent of $(\epsilon_+ - \epsilon)$ in the fits shown in Fig. 5.3. Second, I^2 actually varies by 50% due to changes in the bin time, T, which varies with $(\epsilon_+ - \epsilon)$ and ϵ_+, so measurement of the actual contribution of this term will be fairly inaccurate. Finally, the effective temperature now consists of two parts, white noise from the inductive amplifier and narrow band DC noise mixed up to ω_z. Each component may be extracted from the fits described in next section, but combining the two into a single effective temperature may only be valid for a fixed drive strength (ϵ_+) and detuning ($\epsilon_+ - \epsilon$).

5.7 Measurement of the Strength of the Noise Sources

One way to measure the strengths of the noise sources is to observe the effect of externally added noise. For all measurements in this section, the detuning, $\epsilon_+ - \epsilon$, and the drive, ϵ_+, are kept constant as the noise is changed. In order to observe the flip rate change over a wide range with the application of noise, the choice of detuning and drive strength place the exponential argument of the theoretical flip rate, W, outside the region where Eq. 5.3 is valid. Therefore, the flip rate depends on the noise sources as

$$\frac{1}{\ln W - lnC_1} = f(T + X + T_{ext}) \tag{5.20}$$

$$f = -\frac{\sqrt{2\pi}\epsilon_+^{0.39}}{20.17(\mathrm{K}/\sqrt{\mathrm{Hz}})(\epsilon_+ - \epsilon)^{0.89}} \tag{5.21}$$

where X is the DC noise scaled by $\Delta\nu$ so it may be thought of as a temperature. The external noise was calibrated from independent measurements of the external noise with an uncertainty of 36%. The constant, C_1, is the coefficient of the exponent of Eq. 5.19 which

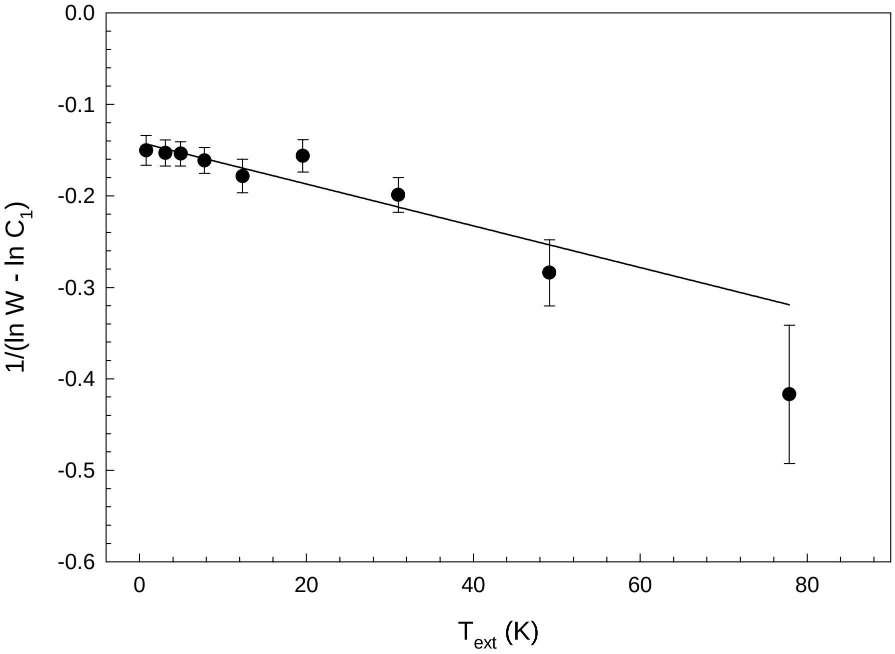

Figure 5.10: Inverse flip rate versus temperature of externally applied noise. The constant, lnC_1, is determined from fits in Fig. 5.3. The parameters, $\epsilon_+/2\pi = 300$ Hz and $(\epsilon_+ - \epsilon)/2\pi = 450$ Hz, are outside the region where $lnW \propto (\epsilon_+ - \epsilon)^{3/2}/\epsilon_+$ so a numerical value of the exponential argument is used.

we know little about theoretically, but can be obtained from the fits in Fig. 5.3. From Fig. 5.10 we may extract a $T + X = (70.0 \pm 3.8)$ K. For this particular drive strength and detuning ($\epsilon_+/2\pi = 300$ Hz, $(\epsilon_+ - \epsilon)/2\pi = 450$ Hz), $T + X$ may be thought of as the effective temperature. Using $T + X$ and assuming $T = 6.1$ K from the measurement of the inductive amplifier, we derive a value for the total DC noise of $I^2/\Delta\nu = 3.0 \pm 0.9 \times 10^{-13} (\mathrm{V}^2/\mathrm{Hz})$. This measurement of the noise is a factor of 8 larger than our estimate, assuming a bandwidth of 300 Hz.

Chapter 6

Stochastic Behavior of Many Electrons

The last chapter describes the stochastic behavior of a single parametric oscillator. Near a cavity mode, small numbers of electrons display similar phase switching behavior, acting like a rigid oscillator. Nevertheless, we observed that Coulomb interactions of a cloud affects the flip rate. This chapter will present the data for 2, 3 and 4 electrons and examine the differences and similarities to 1 electron.

6.1 Measured Flip Rates for 2, 3 and 4 Electrons

Flip rate measurements were made for 2, 3, and 4 electrons in the same manner as for 1 electron. The results show quite a number of similarities and some differences. First, the overall flip rate decreases exponentially with number, as seen in Fig. 6.1. Flip rates for more than 4 electrons could not be measured because the amount of time needed to measure a statistically significant number of flips (more than 4 hours per measurement) is so large that drift in the axial frequency greatly increases the error. The exponential dependence of flip rate on detuning $(\epsilon_+ - \epsilon)$ is also seen for more than one electron as seen in Figs. 6.2 and 6.3, but Fig. 6.4 shows that the slopes of the fit $\ln W = a + b(\epsilon_+ - \epsilon)$ are

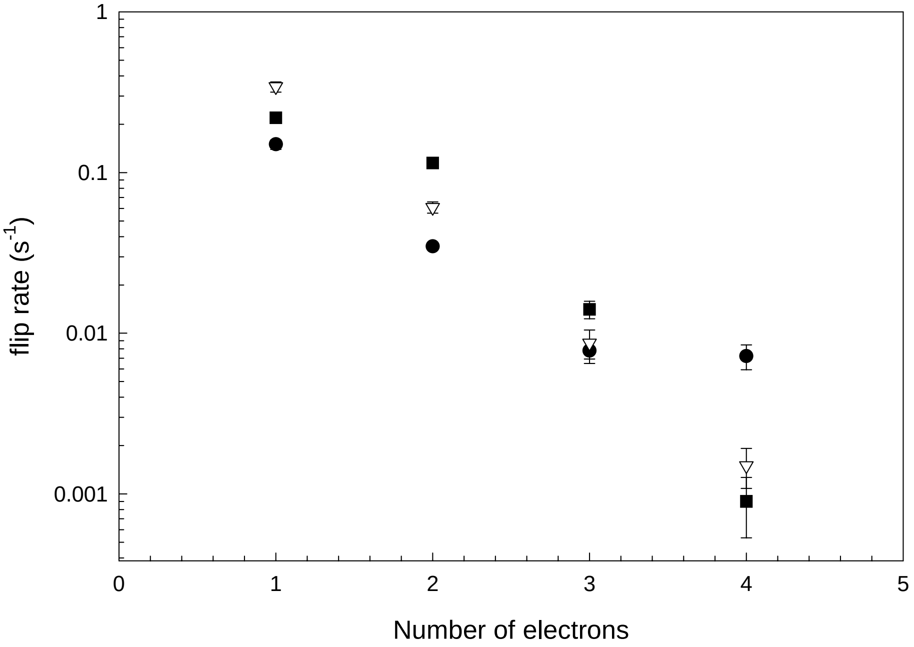

Figure 6.1: Flip rates versus number of electrons for $\epsilon_+/2\pi \approx 100$Hz and $(\epsilon_+ - \epsilon)/2\pi \approx 40$ Hz (circles), $\epsilon_+/2\pi \approx 60$Hz and $(\epsilon_+ - \epsilon)/2\pi \approx 20$ Hz (triangles), $\epsilon_+/2\pi \approx 300$ Hz and $(\epsilon_+ - \epsilon)/2\pi \approx 50$ Hz (squares)

different, especially for 3 electrons (see Fig. 5.4). Fig. 6.5 shows the increase in flip rate with the application of external white noise. These measurements clearly show that there is a difference in flip rates for different numbers of electrons even though the measured amplitudes are the same as for rigid motion. This raises the fundamental question, what is the difference in dynamics between a cloud of N electrons and a cloud of M electrons if each cloud is oscillating with the same phase and amplitude? The next section describes two possible answers to this question.

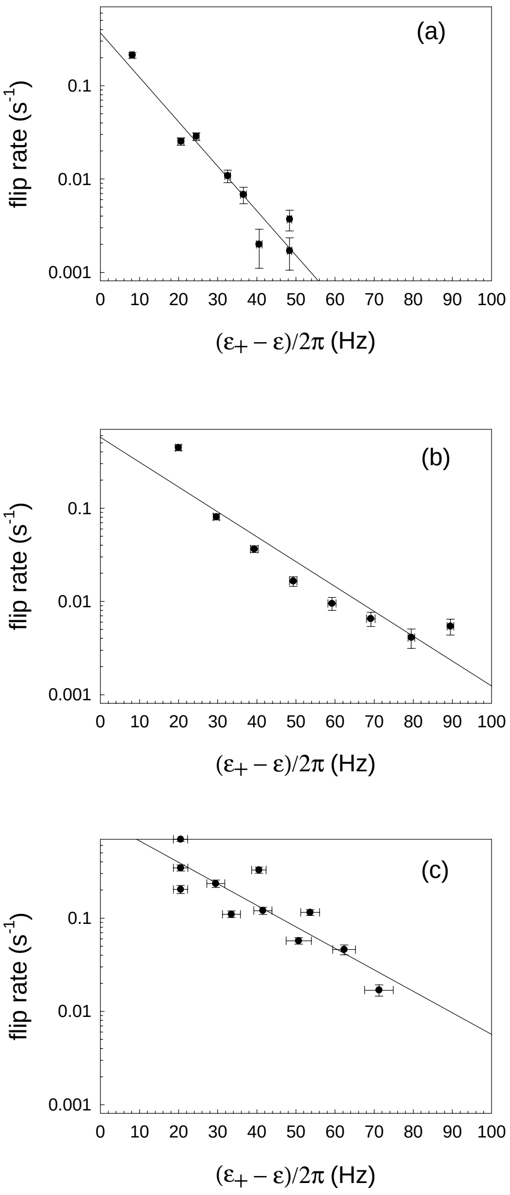

Figure 6.2: Flip rates of 2 electrons versus detuning $(\epsilon_+ - \epsilon)/2\pi$ for (a) $\epsilon_+/2\pi = 29.11$ Hz, (b) $\epsilon_+/2\pi = 91.78$ Hz and (c) $\epsilon_+/2\pi = 297.35$ Hz

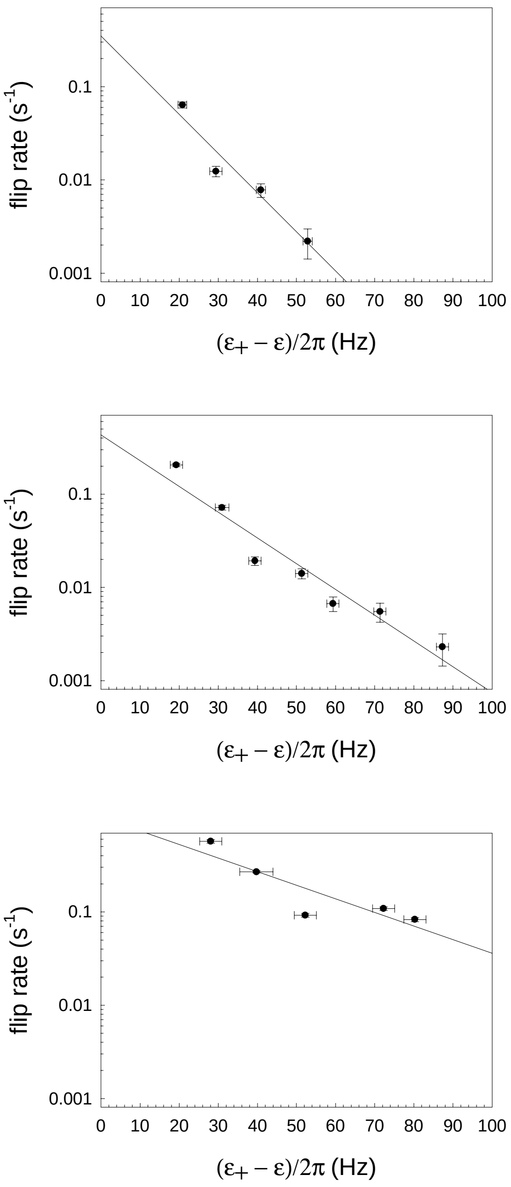

Figure 6.3: Flip rates of 3 electrons versus detuning $(\epsilon_+ - \epsilon)/2\pi$ for (a) $\epsilon_+/2\pi = 94.20$ Hz, (b) $\epsilon_+/2\pi = 304.39$ Hz and (c) $\epsilon_+/2\pi = 534.54$ Hz. These ϵ_+ represent the measurable range and should not be compared to the range in Fig. 6.2

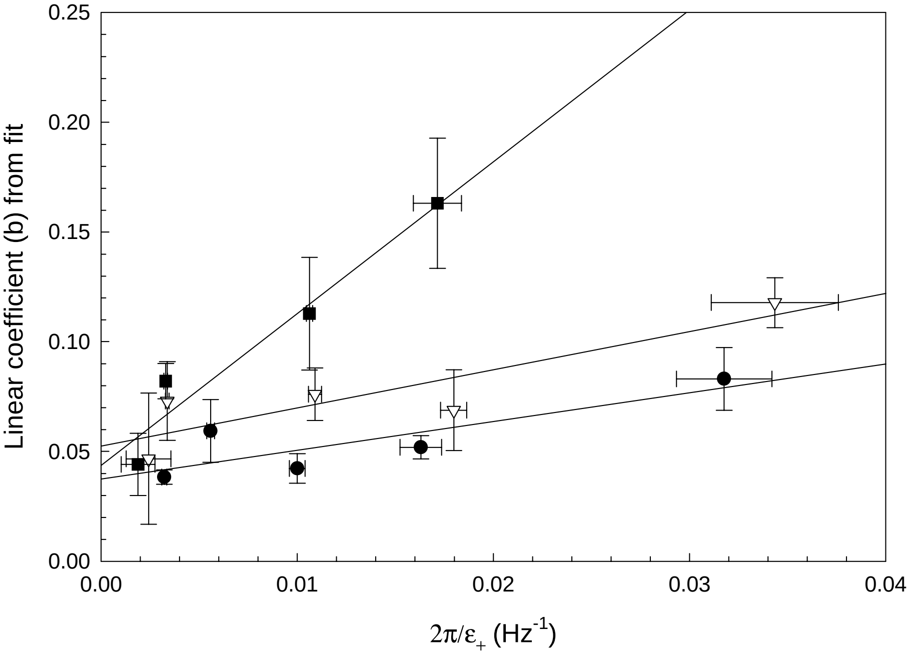

Figure 6.4: Coefficients from the fit of $lnW = a + b(\epsilon_+ - \epsilon)$ for 1 (circles), 2 (triangles) and 3 (squares) electrons versus $1/\epsilon_+$

6.2 Differences between 1, 2, and 3 electrons

6.2.1 Axial Damping and Flip Rates

One answer to the question put forth in the last section is that increasing the damping rate would better cool the center-of-mass. The axial damping rate of the center-of-mass increases linearly with the number of electrons, but the damping rate can be changed by detuning the axial frequency from the center frequency of the amplifier noise resonance (see Fig. 2.11 for the linear dependence of damping rate and location on the noise resonance peak). Fig. 6.6 shows flip rate measurements made for 2 and 3 electrons with a normal damping rate and a damping rate lowered to the damping rate for a single electron. There appears to be no change in a or b for a lower damping rate. This would be expected from the flip rate theory described in Appendix A. The flip rate is given as $W \propto exp(-S/D)$

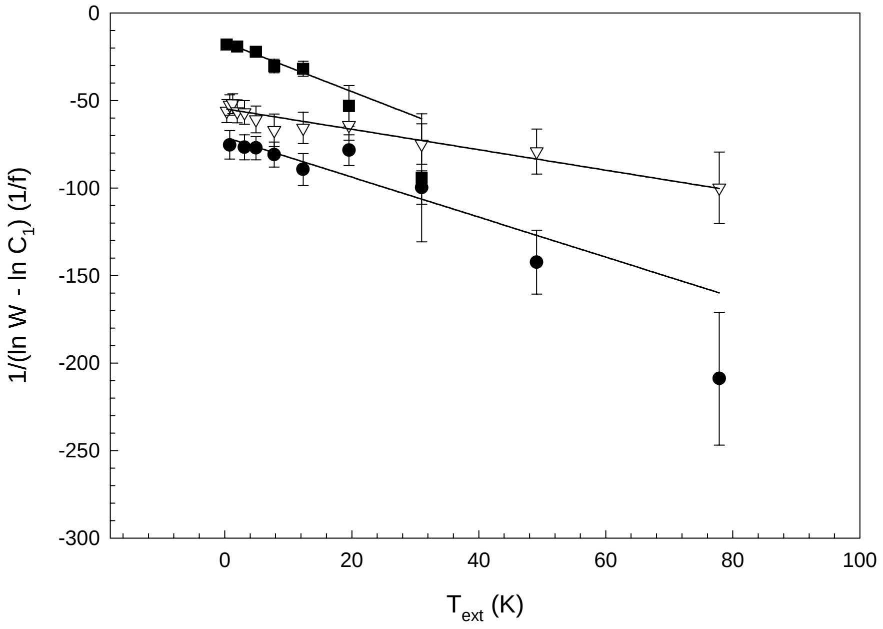

Figure 6.5: Flip rates adjusted by $(1/f) = 8.05(\epsilon_+ - \epsilon)^{0.89}/\epsilon_+^{0.39}$ versus temperature of externally added white noise for 1 (circles), 2 (triangles) and 3 (squares) electrons. For 1 electron, $\epsilon_+/2\pi = 300$ Hz and $(\epsilon_+ - \epsilon)/2\pi = 450$ Hz. For 2 electrons $\epsilon_+/2\pi = 88$ Hz and $(\epsilon_+ - \epsilon)/2\pi = 100$ Hz. For 3 electrons $\epsilon_+/2\pi = 110$ Hz and $(\epsilon_+ - \epsilon)/2\pi = 50$ Hz. The fact that the slopes of these plots are not all 1 indicates that either the theory is not completely correct or the calibration of the external noise power changed between measurements.

where S is the activation energy and depends on $1/\gamma_z$ (Appendix A gives the dependence $S \approx 2Gh/h_T$ and Eq. 3.7 gives $h_T \propto \gamma_z$), and D is the thermal noise and also depends on $1/\gamma_z$.

6.2.2 Effective Temperature and Flip Rates

Another parameter that might change with number of electrons is the effective temperature of the noise affecting the flip rates. It is often useful to identify each degree of freedom of the system with a temperature. It is assumed that when tuned near a cavity mode, the cyclotron temperature is 4.2 K. It was shown in section 5.7 that the effective flip rate for

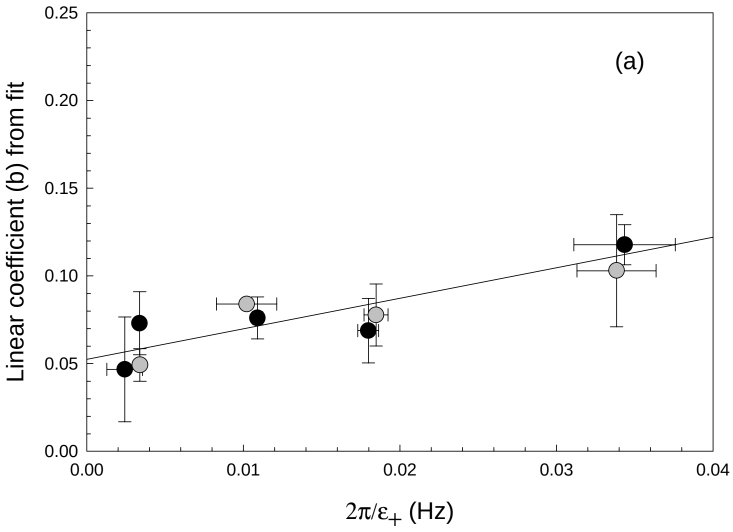

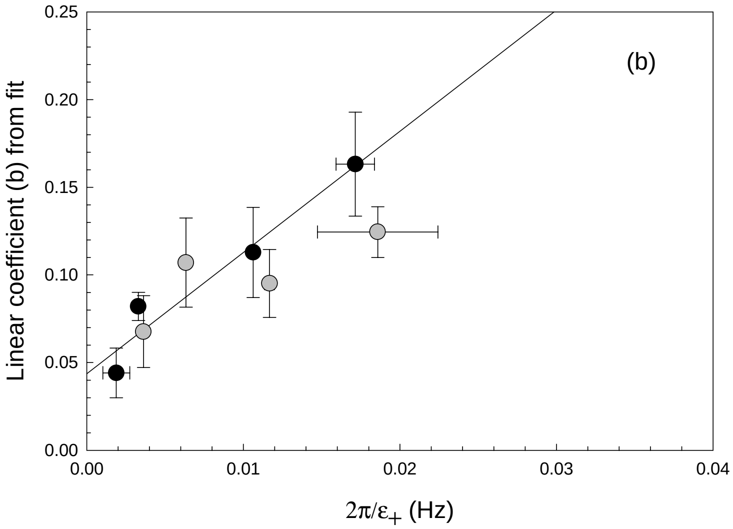

Figure 6.6: (a) Linear coefficients from the fit of $lnW = a + b(\epsilon_+ - \epsilon)$ versus $1/\epsilon_+$ for 2 electrons with full axial damping (black) and half axial damping(grey). (b) same as (a) for 3 electrons with full axial damping (black) and one third axial damping (grey).

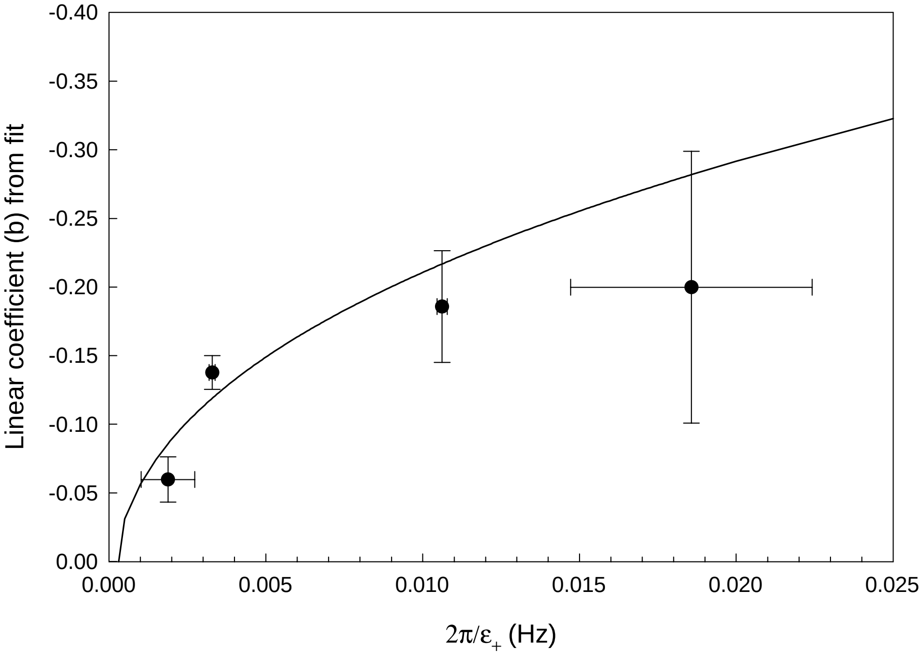

Figure 6.7: Linear coefficient of fit of $\ln W = a + b(\epsilon_+ - \epsilon)^{0.89}$ plotted versus $1/\epsilon_+$. The solid line is the fit of $b = c/\epsilon_+^{0.39}$, giving a $T + \bar{X} = 12.9 \pm 6.4$ K

a single electron depends on two noise terms

$$W = C_1 exp\left(\frac{0.86md^2\omega_z^{3/2}}{k|\lambda_6|^{1/2}}\frac{(\epsilon_+ - \epsilon)^{0.89}}{\epsilon_+^{0.39}}\left[\frac{1}{T + (1/4kR)(I^2/\Delta\nu)A^2}\right]\right) \tag{6.1}$$

The effective temperature is much larger than 4.2 K due to $1/f$ noise from the Fluke 732A power supply. For more than 1 electron, the axial temperature may cool by transferring energy to the cyclotron reservoir via the internal motions. The final temperature depends on the efficiency of the energy transfer, which must depend on the number of Coulomb interactions. Therefore, more electrons have a lower effective axial temperature than fewer electrons. Due to the nonlinear nature of the noise described in Chapt. 5, it is difficult to describe a relation between effective temperature and number of electrons. However, an analysis of the flip rate versus added noise of 2 and 3 electrons in Fig. 6.5 using Eqs. 5.20 and 5.21 gives lower effective temperatures for 2 and 3 electrons (see Table 6.1).

N	$\epsilon_+/2\pi$ (Hz)	$(\epsilon_+ - \epsilon)/2\pi$ (Hz)	T+X (K)
1	300	450	70.9 ± 3.8
2	88	100	54.7 ± 1.1
3	110	50	16.7 ± 1.0

Table 6.1: Effective temperatures extracted from measurements of 1, 2 and 3 electrons with external noise. The three measurements are not easily compared because the effective temperature probably depends inversely on detuning and drive strength. However, since the temperature for 2 and 3 electrons is lower than 1 even for smaller ϵ_+ and $\epsilon_+ - \epsilon$, we conclude the temperature really is decreasing for more electrons.

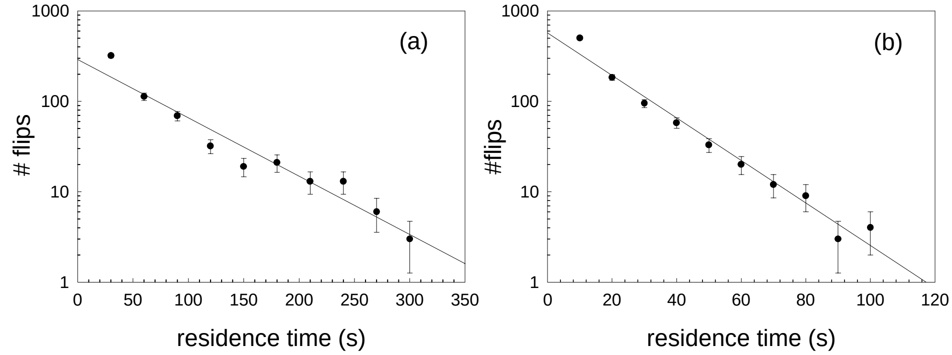

Figure 6.8: Histogram of phase residence times of 2 electrons for (a) $\epsilon_+/2\pi = 92$ Hz, $(\epsilon_+ - \epsilon)/2\pi = 30$ Hz and (b) $\epsilon_+/2\pi = 56$ Hz, $(\epsilon_+ - \epsilon)/2\pi = 20$ Hz.

Three electrons appears to mostly damp the DC noise from the Fluke 732 power supply. Assuming X is small means that the flip rate can be fit to the form $\ln W = a + b(\epsilon_+ - \epsilon)^{0.89}$ as described in section 5.2, and the linear coefficients, b, fit to the form $b = c/\epsilon_+^{0.39}$ where c is proportional to temperature. These fits give an average temperature, $T + \bar{X} = 12.9 \pm 6.4$ which is consistent with the temperature of 3 electrons measured previously.

6.3 Distribution of Phase Residence Times

Fig. 5.7 shows that for 1 electron the distribution is exponential. This is also true for 3 electrons (see Fig. 6.9), but for 2 electrons there were more flips at short times

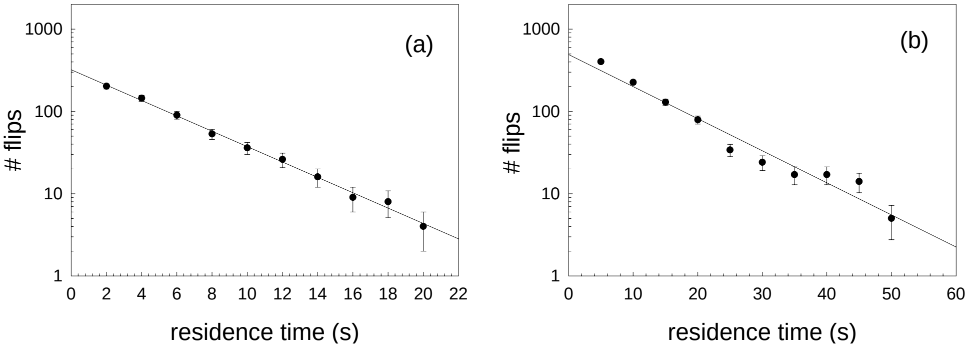

Figure 6.9: Histogram of phase residence times of 3 electrons for (a) $\epsilon_+/2\pi = 304$ Hz, $(\epsilon_+ - \epsilon)/2\pi = 20$ Hz and (b) $\epsilon_+/2\pi = 533$ Hz, $(\epsilon_+ - \epsilon)/2\pi = 50$ Hz.

than expected (see Fig. 6.8). Tan and Gabrielse [7] also observed a nonexponential distribution of phase residence times for many electrons. The dynamics that produces the extra flips are still unknown, but it may be related to the level of internal motions. The earlier observations were made with a cloud that was not completely synchronized so the internal motions were significant. Because 2 electrons do not efficiently transfer energy to the cyclotron motion, internal motions may not be completely damped. Statistically significant measurements could not be made for more than 3 electrons in this thesis, but with this hypothesis, one would expect an exponential distribution for larger numbers of electrons at the rigid limit.

6.4 Cyclotron Damping and Flip Rates

As the cyclotron frequency is detuned from a mode frequency, the cyclotron damping rate decreases which would lead to a higher axial temperature. We observe that for many electrons (15 in Fig. 6.10), the flip rate increases with detuning as the synchronization decreases. Fig. 6.10 shows that the amplitude and the logarithm of the mean phase residence time ($1/\ln W$) serve as equally good measures of the degree of synchronization.

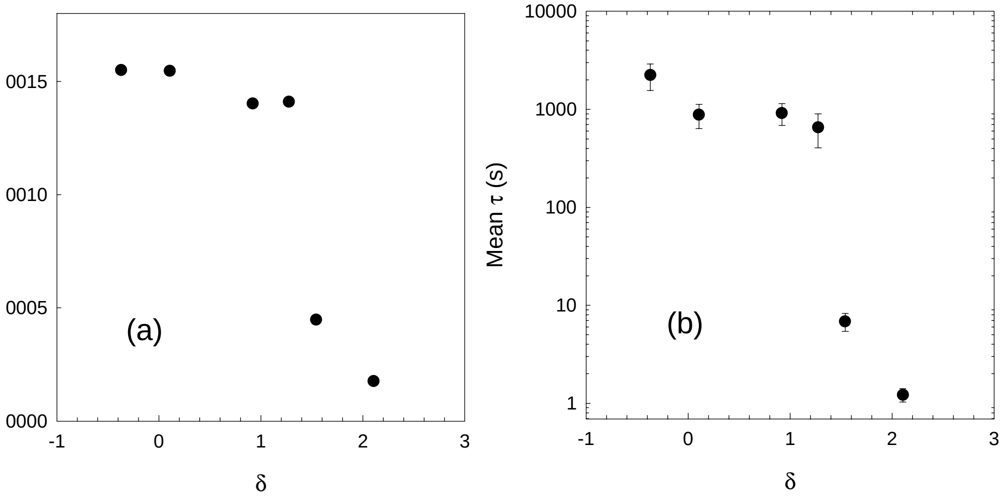

Figure 6.10: Parametric amplitudes and flip rates across a cavity mode. As the mode detuning increases, the center of the lineshape collapses so that the measured amplitude (a) decreases to zero far from the mode. (b) The mean phase residence time ($\tau = 1/W$) also decreases with mode detuning so that either the amplitude or the $\log \tau$ are good measures of the mode cooling power.

Chapter 7

Conclusion

We used a Penning trap with a good cylindrical microwave cavity to probe the synchronization of electrons in the trap. When the cyclotron frequency is tuned near an electromagnetic cavity mode, the cyclotron motion easily damps the internal motions of a cloud of electrons, the axial motions synchronize, and a large center-of-mass amplitude is observed. When the level of noise in the experiment is low enough, the parametrically excited center-of-mass amplitude is that expected for a rigid ball of charge. This synchronized behavior has been observed for 2 to 1000 electrons.

Stochastic phase switching has been observed for 1 electron. This behavior was originally expected for more than one electron and was thought to be related to the internal motions of a cloud of electrons. The observations in this work confirm that stochastic phase switching is a phenomenon of a rigid oscillator in the presence of noise, where the flip rate primarily depends on the level of noise relative to the amplitude of oscillation. This experiment has stimulated a theory that describes the flip rate in terms of parameters of the parametric excitation and agrees well with observations.

Although the theory assumes the noise present in the system is white, some of the noise in this system is comprised of narrowband noise arising from a solid state power supply. This leads to an effective axial temperature for one electron that is significantly higher than the 4.2 K trap and detection circuit.

Similar phase switching behavior has been observed for 2, 3, and 4 electrons with significantly lower flip rates for more electrons. Dependence of the flip rate on drive strength and noise were also different, especially for 3 and 4 electrons. Although the increased damping for larger numbers of electrons was considered as the cause of these differences, it was ruled out when observations of 2 and 3 electrons with lower damping rates produced no change in the flip rate. Rather, we conclude the cause of these differences from 1 electron is the effective temperature. More electrons have a lower effective temperature due to shunting the noise through the Coulomb interactions to the cyclotron motion which then damps to the 4.2 K cavity.

There is still further work to do on both synchronization and stochastic behavior of many electrons. As the cyclotron frequency is swept past a cavity mode frequency by changing the magnetic field, the axial amplitude produces a lineshape that is asymmetric and displays hysteresis, especially for large numbers of electrons. This may be related to the dynamics of the cloud as it approaches synchronization. A similar area to be explored is the lineshape of the parametric resonance when the cloud is partially synchronized which also displays transient behavior.

The primary topic of interest for stochastic behavior is understanding the noise and how it is damped by many electrons. More theoretical work needs to be done to better understand the effects of narrowband noise, but it is probably preferable to remove it from the experiment. Phase flips have also been observed for partial synchronization, but the flip rates as a function of various parameters have not been studied in depth. One clue to the difference between phase switching behavior for rigid and non rigid systems may be the distribution of phase residence times. The histograms created for one electron show the expected exponential distribution, but earlier work on partially synchronized clouds produced histograms with extra flips at short times [7]. This distribution was also observed for 2 electrons (but not for 3), indicating perhaps that the internal mode of the pair was not fully damped. Numerical simulations of 2 electrons may produce some insight that can be extended to many more particles.

Appendix A

Derivation of Phase Flip Rates of a Parametric Oscillator

A.1 Fluctuational Phase Flip Transition Rates

The expression for the rate of phase flips stated in Chapter 5 has been derived by Maloney, Silverstein, et. al. [13]. They begin with the equation of motion for a parametrically driven anharmonic oscillator in the presence of noise

$$\ddot{Z} + \gamma_Z \dot{Z} + \omega_Z^2 Z + \lambda_4 \omega_Z^2 Z^3 + \lambda_6 \omega_Z^2 Z^5 + h\omega_Z^2 \cos(\omega_d t) Z = C\xi(t) \tag{A.1}$$

and solve A.1 in terms of slowly varying variables

$$Z(t) = \sqrt{\frac{2\omega_d \gamma_z}{3|\lambda_4|\omega_z^2}}\,[q_1 \; cos\omega_z t - q_2 \sin\omega_z t] \tag{A.2}$$

$$\dot{Z}(t) = -\sqrt{\frac{\omega_d^3 \gamma_z}{6|\lambda_4|\omega_z^2}}\,[q_1 \sin\omega_z t + q_2 \cos\omega_z t] \tag{A.3}$$

Using a standard averaging procedure by which Eq. A.2 and A.3 are scaled by $\tau = 2t/\gamma_z$ and inserted into Eq. A.1, and fast oscillating terms are neglected, they obtain first order equations of motion for q_1 and q_2

$$\dot{q_1} = -q_1 + \frac{\partial g}{\partial q_2} + \xi_1(2\tau/\gamma_z) \tag{A.4}$$

$$\dot{q_2} = -q_2 - \frac{\partial g}{\partial q_1} + \xi_2(2\tau/\gamma_z) \tag{A.5}$$

where $\xi_{1,2}(2\tau/\gamma_z)$ is the noise and

$$\begin{aligned} g(q_1, q_2) = \frac{1}{2}(q_1^2 + q_2^2)\left[\frac{2\epsilon}{\gamma_z} - \frac{1}{2}(q_1^2 + q_2^2)\frac{|\lambda_4|}{\lambda_4} - \frac{\rho h_T}{3h}(q_1^2 + q_2^2)^2\right] \\ + \frac{1}{2}\frac{h}{h_t}(z_2^2 - q_1^2) \end{aligned} \tag{A.6}$$

where the parameter $\rho = 5\lambda_6 h/9\lambda_4^2$ determines the relative effect of the anharmonic terms.

This theory assumes that the noise in the system, $\xi(t)$, is white near the axial frequency with a correlation function

$$< \xi_i(2\tau/\gamma_z)\xi_i(2\tau'/\gamma_z) > \approx D\delta(\tau - \tau') \tag{A.7}$$

where D is the noise intensity. If the noise is thermal, $D = 3|\lambda_4|kT/8md^2\omega_z\gamma_z$ where m is the mass and d is the trap constant.

The flip rate is proportional to $exp(-S_n/D)$, where S_n ($n = \Psi, \Psi + \pi$) is the activation energy for escape from one of the basins of attraction and is given by the minimum of the action. They solve for the activation energy in the limit that the drive strength is strong enough that the dissipation in Eqs. A.4 and A.5 are small. Eqs. A.4 and A.5 in the absence of noise ($\xi_{1,2} = 0$) and dissipation ($q_1, q_2 = 0$) describe conservative motion with $g(q_1, q_2)$ as the Hamiltonian. The activation energy can be approximated as

$$S_{\Psi,\Psi+\pi} \approx 2G_{\Psi,\Psi+\pi}h/h_T \tag{A.8}$$

where $G_{\Psi,\Psi+\pi}$ are the maxima of the energy surface defined by the Hamiltonian $g(q_1, q_2)$

$$G_{\Psi,\Psi+\pi} = \frac{[1 - 4\rho(1 - \frac{\epsilon}{\epsilon_+})]^{3/2} + 6\rho(1 - \frac{\epsilon}{\epsilon_+}) - 1}{24\rho^2}. \tag{A.9}$$

If the trap is tuned to make $|C_4| < 10^{-5}$ then $|C_4| \ll |C_6|A^2$, and the flip rate can be approximated as

$$G_{\Psi,\Psi+\pi} = \frac{1}{3}(-\rho)^{-1/2}\left(1 - \frac{\epsilon}{\epsilon_+}\right)^{3/2}, \tag{A.10}$$

the flip rate can be approximated as

$$W \propto exp\left(-\frac{16md^2\omega_z^{3/2}(\epsilon_+ - \epsilon)^{3/2}}{3\sqrt{5}kT|\lambda_6|^{1/2}\epsilon_+}\right) \tag{A.11}$$

If the trap is severely detuned so $|C_4| \gg |C_6|A^2$, $-\rho(1 - \epsilon/\epsilon_+)$s very small then Eq. A.9 becomes

$$G_{\Psi,\Psi+\pi} = \frac{1}{4}(1 - \frac{\epsilon}{\epsilon_+})^2, \tag{A.12}$$

and the flip rate is approximately

$$W \propto exp\left(-\frac{3\omega_z(\epsilon_+ - \epsilon)^2}{8|\lambda_4|kT\epsilon_+}\right). \tag{A.13}$$

Eqs. A.11 and A.13 is only valid for values $(\epsilon_+ - \epsilon)/\epsilon_+ \ll 1$. This condition is not usually met experimentally, so a numerically generated value of $S_{\Psi,\Psi+\pi}$ must be used as shown in Fig. A.1. We fit this numerically generated data to gives

$$S_{\Psi,\Psi+\pi} \approx \frac{h}{h_T}\frac{.24(\epsilon_+ - \epsilon)^{0.89}}{(-\rho)^{1/2}\epsilon_+^{0.89}}. \tag{A.14}$$

Therefore, the flip rate for our experimental parameters is approximately

$$W \propto \exp\left[\frac{20.17\frac{\mathrm{K}}{\sqrt{\mathrm{Hz}}}(\epsilon_+ - \epsilon)^{0.89}}{\sqrt{2\pi}\epsilon_+^{0.39}T}\right]. \tag{A.15}$$

Eqs. A.11, A.13 and A.15 imply that the flip rate depends on drive strength, detuning

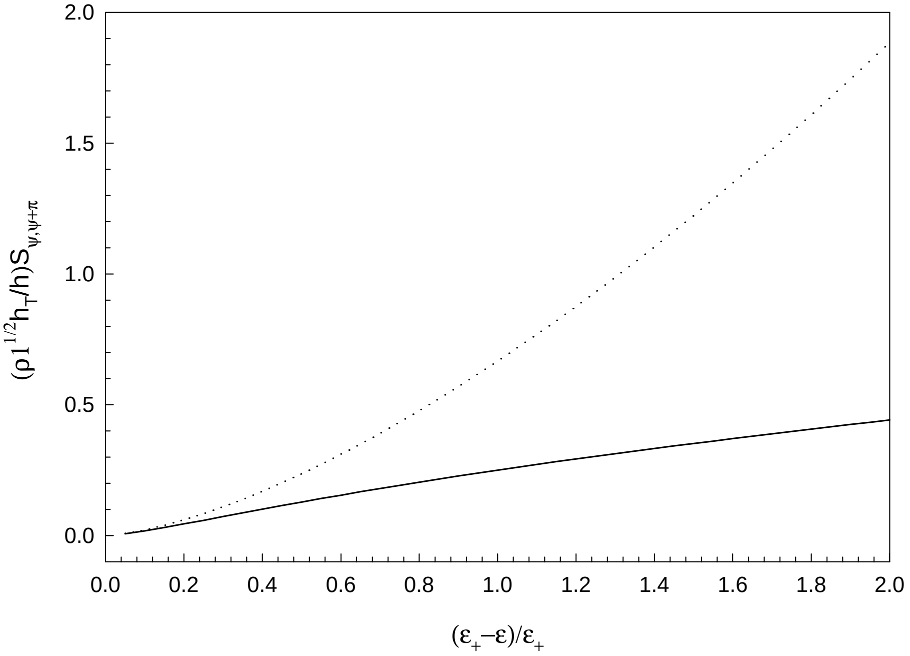

Figure A.1: Activation energy verses relative detuning. The solid line is numerical form from which Eq. A.14 is derived. The dotted line is the approximation from which Eq. A.9 is derived. It is clear the approximation is only valid for $(\epsilon_+ - \epsilon)/\epsilon_+$ near zero.

from the edge of the parametric resonance, and the effective temperature of the system.

A.2 Conditions of Validity of Phase Flip Rates

Equations A.11, A.13 and A.15 are only valid if the approach to equilibrium in phase space is underdamped. The damping condition is derived in a paper by Tseng, et. al. [12] by starting with the equations of motion

$$\frac{dA}{dt} = -\frac{\gamma_z}{2} A \left[1 - \frac{h}{h_T} \sin 2\Psi\right] \tag{A.16}$$

$$\frac{d\Psi}{dt} = -\epsilon + \frac{1}{4} h\omega_z \cos(2\Psi) + \frac{3}{8}\lambda_4 \omega_z A^2 + \frac{5}{16}\lambda_6 \omega_z A^4 \tag{A.17}$$

or in terms of the in-phase and quadrature variables $A_I = A\cos(\Psi)$ and $A_Q = A\sin(\Psi)$,

$$\frac{d}{dt}A_I = \left[\epsilon + \frac{1}{4}h\omega_z - \frac{3}{8}\lambda_4\omega_z A^2 - \frac{5}{16}\lambda_6\omega_z A^4\right] A_Q - \frac{\gamma_z}{2}A_I \tag{A.18}$$

$$\frac{d}{dt}A_q = -\left[\epsilon - \frac{1}{4}h\omega_z - \frac{3}{8}\lambda_4\omega_z A^2 - \frac{5}{16}\lambda_6\omega_z A^4\right] A_I - \frac{\gamma_z}{2}A_Q \tag{A.19}$$

where $A^2 = A_I^2 + A_Q^2$. Near the steady state, the amplitude variables can be expanded about equilibrium to obtain linear differential equations for deviations from the steady state. These deviations from the steady state are assumed to have the time dependence $e^{t/\tau_{1,2}}$ where $\tau_{1,2}$ are found to be

$$\tau_1^{-1} = \frac{\gamma_z}{2} + \sqrt{\left(\frac{\gamma_z}{2}\right)^2 \pm 4\left(\frac{\partial A_\pm^2}{\partial\epsilon}\right)^{-1} |\epsilon_\pm| A_\pm^2} \tag{A.20}$$

$$\tau_2^{-1} = \frac{\gamma_z}{2} - \sqrt{\left(\frac{\gamma_z}{2}\right)^2 \pm 4\left(\frac{\partial A_\pm^2}{\partial\epsilon}\right)^{-1} |\epsilon_\pm| A_\pm^2}, \tag{A.21}$$

where $\partial A_\pm^2/\partial\epsilon$ is taken from

$$\frac{5\lambda_6\omega_z}{16}A_\pm^4 + \frac{3\lambda_4\omega_z}{8}A_\pm^2 + \epsilon_\pm - \epsilon = 0. \tag{A.22}$$

If the approach to equilibrium is underdamped, $\tau_{1,2}$ have an imaginary part which requires

$$\left(\frac{\gamma_z}{2}\right)^2 \pm 4\left(\frac{\partial A_\pm^2}{\partial\epsilon}\right)^{-1} |\epsilon_\pm| A_\pm^2 < 0. \tag{A.23}$$

In all the experiments performed in this thesis, $\lambda_6 < 0$ and λ_4 is small, so A_+ is always the appropriate solution. For the case that λ_4 is very small, Eq. A.23 becomes

$$(\epsilon_+ - \epsilon)\epsilon_+ > \frac{N^2\gamma_z^2}{32} \tag{A.24}$$

$$\frac{(\epsilon_+ - \epsilon)\epsilon_+}{4\pi^2} > N^2 6.125 \tag{A.25}$$

where $\gamma_z/2\pi$ has been measured to be 14 Hz. This requirement is always met in these experiments.

Appendix B

Dynamics of 2 and 3 Electrons

B.1 Equilibrium Positions of 2 Electrons

Since the flip rate appears to depend intimately on the nature of the Coulomb interactions, it is interesting to examine in detail the relative positions of the electrons in the Penning trap. It is possible to do this analytically for two electrons, following a procedure described by Baumann and Nonnenmacher [41], by writing the equations of motion neglecting damping and anharmonicity in terms of the center-of-mass ($\mathbf{X}$) and relative ($\mathbf{x}$) coordinates

$$\ddot{\mathbf{x}} = -2q\omega_z^2(\mathbf{x} - 3z\hat{e}_z) + \omega_c(\dot{\mathbf{x}} \times \hat{e}_z) + \frac{2q^2}{4\pi m\epsilon_o}\frac{\mathbf{x}}{|\mathbf{x}|^3} \tag{B.1}$$

$$\ddot{\mathbf{X}} = \omega_z^2(\mathbf{X} - 3Z\hat{e}_z) + \omega_c(\dot{\mathbf{X}} \times \hat{e}_z) \tag{B.2}$$

Note that only Eq. B.1 contains the Coulomb term. We define $Q^2 = (2q^2/4\pi\epsilon_o m)$ and rewrite Eq.(B.1) in cylindrical coordinates

$$\begin{pmatrix} a_r \\ a_\phi \\ a_z \end{pmatrix} = \frac{\omega_z}{2}\begin{pmatrix} r \\ \phi \\ 2z \end{pmatrix} - \omega_c \begin{pmatrix} v_\phi \\ v_r \\ 0 \end{pmatrix} + \frac{Q^2}{(r_o^2 + z_o^2)^{3/2}}\begin{pmatrix} r \\ \phi \\ z \end{pmatrix} \tag{B.3}$$

Rescaling time as $\tau = t\kappa$ where $\kappa = \omega_c^2/4 - \omega_z^2/2$, and defining the scaled coordinates $\zeta = \left(Q^2/\kappa^2\right)^{3/2} z$ and $\rho = \left(Q^2/\kappa^2\right)^{3/2} r$, we can write the axial and radial equations of motion as

$$\ddot{\zeta} + \lambda^2\zeta = \frac{\zeta}{(\rho^2+\zeta^2)^{3/2}} \tag{B.4}$$

$$\ddot{\rho} + \rho = \frac{\rho}{(\rho^2+\zeta^2)^{3/2}} + \frac{\nu^2}{\rho^3} \tag{B.5}$$

where $\lambda^2 = \omega_z^2/\kappa^2$, $\nu^2 = \tilde{l}_z/\kappa^2$, and $\tilde{l}_z = \rho^2(\dot{\phi} - \omega_c/2)$.

The Lagrangian for this system is

$$L = \frac{1}{2}(\dot{\rho} + \dot{\zeta}) - U(\rho, \zeta) \tag{B.6}$$

$$U(\rho,\zeta) = \frac{1}{2}(\rho^2 + \lambda^2\zeta^2) + \frac{\nu^2}{2\rho^2} + \frac{1}{\sqrt{\rho^2+\zeta^2}} \tag{B.7}$$

Solving with $dU/d\rho = 0$ and $dU/dz = 0$ gives the minima at

$$\rho_o = \frac{\sqrt{\nu}}{(1-\lambda^2)^{3/2}} \tag{B.8}$$

$$\zeta_o = \begin{array}{rl} 0 & \text{when} \quad \lambda > \lambda_c, \\ \sqrt{\lambda^{-4/3} - \frac{\nu}{(1-\lambda^2)^{1/2}}} & \text{when} \quad \lambda < \lambda_c. \end{array} \tag{B.9}$$

Here, λ_c satisfies the equation $\sqrt{1-\lambda_c^2} = \nu\lambda_c^{4/3}$. When $\zeta_0 = 0$ (large angular momentum), the particles lie in the same x-y plane and move in circular paths separated by $2\rho_o$. When $\zeta > 0$ (small angular momentum), the particles move out of the plane and into a dumbbell configuration with the centers of the orbits separated by $2\rho_o$ radially and $2\zeta_0$ axially. For 2 electrons, $\lambda^2 = 5.68 \times 10^{-7}$ is much smaller than $\nu^2 = 8.03 \times 10^{-4}$, so $\lambda_c \approx 1 > \lambda$. Therefore the electrons are always in the dumbbell configuration. The radial separation is 2.12×10^{-6} cm which is about 700 times smaller than the axial separation of 1.52×10^{-3} cm. The positions of three electrons in a trap cannot be solved analytically, and requires much CPU time to solve numerically covering all time scales.

B.2 Transfer of Energy between Axial and Cyclotron Motions

O'Neil and Hjorth [42,43] have developed a theory for plasmas with a single sign of charge that describes the transfer of energy of from one degree of freedom to another that have two different effective temperatures. They assume the plasma is strongly magnetized and weakly correlated, which means the cyclotron radius is smaller than both the minimum separation of two particles and the classical distance of closest approach, $\bar{b} = 2e^2/T$ where e is the charge and T is the temperature. They observe that the total cyclotron kinetic energy is an adiabatic invariant because the collision time is much longer than the oscillation period of the cyclotron motion. However, the adiabatic invariant is not strictly conserved as each collision produces exponentially small exchange of energy between the axial and cyclotron motions which acts cumulatively to equilibrate the axial and cyclotron temperatures. In the case of this experiment, because the cyclotron damping is so strong when the plasma is completely synchronized, we assume the cyclotron temperature remains at 4.2 K and the axial temperature is lowered by energy transfer.

The energy transfer in the plasma is dominated by well separated binary collisions of close radial approach which may be modeled as a Boltzmann-like collision operator. The rate of change in the cyclotron temperature, T_c, is given by [43]

$$\frac{dT_c}{dt} = (T_z - T_c) n \bar{b}^2 \bar{v}_z I(\bar{\epsilon}) \tag{B.10}$$

where n is the density, $\bar{v}_z$ is the average axial velocity and $\bar{\epsilon} = \bar{v}_z/\omega_c \bar{b}$. Since $\bar{\epsilon}$ is small, $I(\bar{\epsilon})$ is given by

$$I(\bar{\epsilon}) \approx (0.47)\bar{\epsilon}^{1/5} \exp\left[\frac{-(2.05)}{\bar{\epsilon}^{2/5}}\right]. \tag{B.11}$$

Eq. B.10 implies the rate of energy transfer is proportional to the density, which is presumably proportional to the number of electrons. Thus more electrons transfer energy from the axial motion to the cyclotron motion more efficiently and a lower effective axial temperature is reached than with fewer electrons.

Bibliography

[1] B. V. der Pol Phil. Mag. **3**, 65 (1927).

[2] Y.Yamaguchi and H. Shimizu, Physica **11**, 212 (1984).

[3] J. Hansen and P. Lindelof, Rev. Mod. Phys. **56**, 431 (1984).

[4] M. Feigenbaum, Phys. Lett. **74**, 375 (1978).

[5] T. Carrol and L. Pecora, Phys. Rev. Lett. **70**, 576 (1993).

[6] B. McNamara and K. Wiesenfeld, Phys. Rev. A **39**, 4854 (1989).

[7] J. Tan and G. Gabrielse, Phys. Rev. A **48**, 3105 (1993).

[8] R. Wuerker, H. Shelton, and R. Langmuir, J. Appl. Phys. **30**, 342 (1959).

[9] R. Blumel, C. Kappler, W. Quint, and H. Walther, Phys. Rev. A **40**, 808 (1989).

[10] J. Hoffnagle, R. DeVoe, L. Reyna, and R. Brewer, Phys. Rev. Lett. **61**, 255 (1988).

[11] J. Tan, J. Bollinger, B. Jelenkovic, and D. Wineland, Phys. Rev. Lett. **75**, 4198 (1995).

[12] C. Tseng, D. Enzer, G. Gabrielse, and F. Walls, (submitted to Phys. Rev. A.).

[13] C. Maloney, M. Silverstein, M. Dykman, and V. Smelyanskiy, (unpublished).

[14] H. Kramers, Physica **4**, 284 (1940).

[15] M. Dykman and V. Smelyanskiy, Phys. Rev. A **41**, 3090 (1990).

[16] J. Woo and R. Landauer, IEEE J. Quantum Electronics **7**, 435 (1971).

[17] R. Kautz, Reports on Progress in Physics **59**, 935 (1996).

[18] L. Brown and G. Gabrielse, Rev. Mod. Phys. **58**, 233 (1986).

[19] F.M.Penning, Physica (Utrecht) **3**, 873 (1936).

[20] D. Wineland, P. Ekstrom, and H. Dehmelt, Phys. Rev. Lett. **31**, 1279 (1973).

[21] G. Gabrielse and F. MacKintosh, Intl. J. of Mass Spec. and Ion Phys. **57**, 1 (1984).

[22] J. Tan and G. Gabrielse, Appl. Phys. Lett. **55**, 2144 (1989).

[23] J. D. Jackson, *Classical Electrodynamics, 2nd edition* (John Wiley and Sons, Inc., New York, 1975).

[24] G. Gabrielse and H. Dehmelt, Phys. Rev. Lett. **55**, 67 (1995).

[25] G. Gabrielse, J. Tan, and L. Brown, in *Cavity Quantum Electrodynamics*, edited by T. Kinoshita (World Scientific, Singapore, 1990).

[26] R.S. VanDyke Jr. , P. Schwinberg, and H. Dehmelt, Phys. Rev. Lett. **59**, 26 (1987).

[27] R. V. Jr. in *Cavity Quantum Electrodynamics*, edited by T. Kinoshita (World Scientific, Singapore, 1990).

[28] J. Tan and G. Gabrielse, Phys. Rev. Lett. **67**, 3090 (1991).

[29] R. Davidson, *Physics of Nonneutral Plasmas* (Addison-Wesley, Redwood City, CA, 1990).

[30] T. O'Neil, in *Non-neutral Plasma Physics*, edited by C. Roberson and C. Driscoll (American Institute of Physics, College Park, M.D., 1988).

[31] D. Dubin, Phys. Rev. Lett. **66**, 2076 (1991).

[32] J. Bollinger, D. Heinzen, F. Moore, W. Itano, and D. Wineland, Phys. Rev. A **48**, 525 (1993).

[33] C. Weimer, J. Bollinger, F. Moore, and D. Wineland, Phys. Rev. A **49**, 3842 (1994).

[34] L. Brown, G. Gabrielse, K. Helmerson, and J. Tan, Phys. Rev. A **32**, 3204 (1985).

[35] D. Hall, Ph.D. thesis, Harvard University, 1997.

[36] H. Dehmelt and F. Walls, Phys. Rev. Lett. **21**, 127 (1968).

[37] C. Tseng and G. Gabrielse, Appl. Phys. B **60**, 95 (1995).

[38] L. D. Landau and E. M. Lifshitz, *Mechanics (Third Edition)* (Pergamon Press, New York, 1976).

[39] *Handbook of Mathematical Functions*, edited by M. Abramowitz and I. Stegun (Dover, New York, 1970).

[40] P. Bevington and D. Robinson, *Data Reduction and Error Analysis for the Physical Sciences* (McGraw-Hill, Inc., New York, 1992).

[41] G. Baumann and T. Nonnenmacher, Phys. Rev. A **46**, 2682 (1992).

[42] T. O'Neil and P. Hjorth, Phys. Fluids **28**, 3241 (1985).

[43] P. Hjorth and T. O'Neil, Phys. Fluids **30**, 2613 (1987).